Crustal Permeability Changes Observed From Seismic Attenuation: Impacts on Multi-Mainshock Sequences

Luca Malagnini[1], Tom Parsons[2], Irene Munafo[1], Simone Mancini[3], Margarita Segou[4], and Eric L. Geist[2]

[1]Istituto Nazionale di Geofisica e Vulcanologia
[2]United States Geological Survey
[3]University of Bristol
[4]British Geological Survey

November 22, 2022

Abstract

Measuring variations of seismic attenuation over time, while requiring extreme measurement sensitivity, provides unique insights into the dynamic state of stress in the Earth's crust at depth. We analyze seismic data from earthquakes of the 2016-2017 Central Apennines seismic sequence and obtain high-resolution time histories of seismic attenuation in a wide frequency band (0.5-30 Hz) that are characterized by strong earthquake dilatation-induced fluctuations (deep), as well as damage-induced ones (shallow). The cumulative elastic stress drop after the sequence causes negative dilatation, reduced permeability and seismic attenuation. We observe that M[?]3.5 earthquake occurrence vs. time and distance is consistent with fluid diffusion, and that these diffusion signatures are associated with changes in seismic attenuation during the first days of the Amatrice, Visso-Norcia, and Capitignano sub-sequences. We conclude that coseismic permeability changes, partially evidenced by seismic attenuation, create fluid diffusion pathways that are at least partly responsible for triggering multi-mainshock seismic sequences.

manuscript submitted to *Journal of Geophysical Research*

Crustal Permeability Changes Inferred From Seismic Attenuation: Impacts on Multi-Mainshock Sequences

Luca Malagnini[1*], Tom Parsons[2], Irene Munafò[1], Simone Mancini[3], Margarita Segou[4], and Eric L. Geist[2]

[1]Istituto Nazionale di Geofisica e Vulcanologia, Sezione di Roma 1, Rome, Italy.

[2]United States Geological Survey, Moffett Field, CA, USA.

[3]Scuola Superiore Meridionale, Università degli Studi di Napoli Federico II, Naples, Italy.

[4]British Geological Survey, Edinburgh, UK

[*]Corresponding author: Luca Malagnini (luca.malagnini@ingv.it)

Key Points:

1) Seismic attenuation is fundamentally linked to crustal permeability
2) During a seismic sequence, bulk permeability of crustal rocks and pore-fluid pressure are modulated by cumulative seismic stress drop
3) The seismic sequence of the Central Apennines (2016-17) is a long episode of fluid diffusion

Abstract

Measuring variations of seismic attenuation over time, while requiring extreme measurement sensitivity, provides unique insights into the dynamic state of stress in the Earth's crust at depth. We analyze seismic data from earthquakes of the 2016-2017 Central Apennines seismic sequence and obtain high-resolution time histories of seismic attenuation in a wide frequency band (0.5-30 Hz) that are characterized by strong earthquake dilatation-induced fluctuations (deep), as well as damage-induced ones (shallow). The cumulative elastic stress drop after the sequence causes negative dilatation, reduced permeability and seismic attenuation. We observe that $\mathbf{M} \geq 3.5$ earthquake occurrence vs. time and distance is consistent with fluid diffusion, and that these diffusion signatures are associated with changes in seismic attenuation during the first days of the Amatrice, Visso-Norcia, and Capitignano sub-sequences. We conclude that coseismic permeability changes, partially evidenced by seismic attenuation, create fluid diffusion pathways that are at least partly responsible for triggering multi-mainshock seismic sequences.

Plain Language Summary

We investigate the Central Apennines (Italy) seismic sequence that started with the 24 August 2016 M5.97 Amatrice shock, and led to a cascade of 11 more M≥5 shocks, including the 30 October 2016 M6.33 Norcia mainshock. We measure changes in seismic attenuation vs. time, observe patterns of earthquake occurrence vs time and distance that are consistent with fluid diffusion, and calculate crustal the dilatation induced by the sequence. We support a model of permeability-driven seismic attenuation: under extensional tectonics, the elastic stress drop after the seismic sequence results in negative dilatation, reduced permeability, and reduced attenuation. During the first days following the main events of the sequence, fluid diffusion is associated with changes in seismic attenuation. What emerges is that: (i) coseismic negative dilatation following large normal fault earthquakes closes fluid-filled cracks, driving fluids out, (ii) coseismic damage to fault zones and in the shallow crust provides pathways for fluid transfer, (iii) seismic attenuation is temporarily decreased during this time, (iv) short-lived (<10 days) diffusion into adjacent fault zones and the shallow crust triggers subsequent earthquakes, (v) seismic attenuation gradually recovers after this redistribution of fluids, (vi) the process repeats until regional failure stress is exhausted.

1 Introduction

Until recently, seismic attenuation was considered constant in time; at least it was studied as such (e.g., Malagnini and Dreger, 2016). Previous work on temporally changing attenuation was performed in volcanic settings (Titzschkau et al., 2010), or after strong-motion events (e.g., Chen et al., 2015; Kelly et al., 2013). Then a study by Malagnini and colleagues (2019) demonstrated that total seismic attenuation fluctuates periodically, responding to slow-varying seasonal stresses and solid Earth tides. They also showed sharp increases of the attenuation parameter $Q_S^{-1}(f,t)$ due to shallow rock damage after strong-motion episodes, and either increases or decreases of $Q_S^{-1}(f,t)$ due to static stress transfer from earthquakes occurring on nearby faults.

Malagnini and Parsons (2020) interpreted the fluctuations of $Q_S^{-1}(f,t)$ in terms of changes in permeability driven by variable compressional stresses. Of particular interest was the variation of crustal attenuation related to strong-motion earthquakes. Malagnini and Parsons envisioned two competing effects in the aftermath of a mainshock: (1) shallow damage that mostly affected relatively low-frequency surface waves (0.5-1.5 Hz, where 0.5 Hz was the minimum frequency observed), and (2) stress-induced dilatation from the static stress drop of the mainshocks of the sequence (either from each individual earthquake, or cumulatively).

Seismic attenuation has two fundamental components: (1) redistribution of seismic radiation in time and space by scattering behind the wavefront of interest (either direct P or S, e.g., Hoshiba 1995; Akinci et al., 2020); and (2) anelasticity, which transforms the elastic energy carried by stress waves into heat. This study deals with the anelastic dissipation of seismic energy. Dissipated seismic energy (converted into heat) has two contributions: (1) energy dissipated in the immediate vicinity of the fault, especially at high frequency, and (2) elastic energy dissipated along the path traveled between the surface of the volume that encapsulates the source (see previous point) and the receiver. By definition, dissipation of the first kind cannot be observed, and is inevitably included in a more general budget named "*breakdown work*" (Tinti et al., 2005) that contains frictional heat generated by fault slip, or slip-rate, weakening phase, and energy spent on changing surfaces, including new fault surface, the surface obtained by the formation

of new fragments and the comminution of existing ones, all the way to the formation of fault gouge.

Another distinction can be made between two different contributions to attenuation of elastic energy of traveling stress waves that are of roughly equivalent importance (Hanks, 1982; Kilb et al., 2012), occurring either along the crustal path, or in the immediate vicinity of the free surface (assuming a surface recording device). Our study deals only with dissipation occurring along crustal propagation. Lastly, for the sake of completeness, we remind the reader that in very shallow, fluid-rich environments, bubble production induced by traveling stress-waves may also cause significant attenuation (Tisato et al., 2015).

Crustal fluids are thought to play a primary role in anelastic attenuation along crustal paths. The physical phenomenon is that of viscous dissipation of seismic energy into heat within interstitial fluids. In fact, it is believed (e.g., O'Connell and Budiansky, 1977) that the elastic energy carried by stress waves is dissipated through two mechanisms: viscous damping acting on the pore fluids that are forced to move within isolated cracks, and stress-induced fluid flow between interconnected cracks. The dimensions of rock-permeating cracks, the characteristics of their statistical distribution, and the degree of their interconnection (i.e., the permeability of crustal rocks), completely define the frequency dependence of the anelastic attenuation parameter Q_i^{-1}, where "*i*" can be either P or S (without loss of generality we can limit our case to direct S-waves).

Depending on the frequency of oscillation, the interconnection of cracks within the network and the level of saturation, pore fluids oscillate within and between cracks in saturated or partially saturated rocks at low frequencies. A drained regime is attained when the period of oscillation is large enough (in units of fluid relaxation time) to allow inter-crack flow. Alternatively, they can oscillate within the same crack at intermediate frequencies in either saturated or partially saturated rocks. An isolated regime is attained when there is not enough time (in units of fluid relaxation time) to oscillate between cracks, although there is enough time for intra-crack oscillations. A *glued* regime occurs when the period of oscillation is shorter than the relaxation

time of the viscous fluid within the crack, and the fluid causes negligible dissipation (O'Connell and Budiansky, 1977). Transitions between different regimes can be observed by sweeping through a wide frequency band, where peaks in the attenuation parameter $\left(Q^{-1}(f)\right)$ are expected to correspond to each regime transition (O'Connell and Budiansky, 1977). Dry conditions may also occur in specific natural environments (e.g., the Moon, see Mitchell, 1995), with no viscous dissipation.

If crack density and connectivity directly determine the permeability of crustal rocks, the average crack orientation determines its anisotropic behavior, and its sensitivity to static stress changes, like the stress transfer from a seismic dislocation occurring on a nearby fault. An interesting example of this effect is exhibited after induced unclamping of the San Andreas Fault (SAF) by the **M**6.5 San Simeon earthquake (Johanson and Bürgmann, 2010; Malagnini et al., 2019). In addition to static stress variations, weak motions excited by large distant earthquakes (at regional to teleseismic distances) can influence the permeability of crustal rocks if they radiate enough energy at relatively low-frequency (~0.05 Hz, see Roeloffs, 1998). The proposed mechanism is that of breaking and subsequently flushing away colloidal deposits that clog rock pores and cracks, resulting in large increases in rock permeability, stream discharge, (Roeloffs, 1998; Manga et al., 2016; Manga and Brodsky, 2006; Brodsky et al., 2003), and increased seismic attenuation (Malagnini et al., 2019). The same mechanism may be responsible for triggering distant earthquakes by teleseismic waves through fluid diffusion caused by increased permeability (Parsons et al., 2017). Finally, the results of a numerical experiment performed by Barbosa et al. (2019) show that seismically induced viscous shearing within cracks of the order of those initiating unclogging (0.1 to 1 Pa) are plausible for strain magnitudes and frequencies typically observed in field and laboratory measurements.

The colloidal particles mobilized in a specific crustal volume by the fluid flow-induced shear stresses during some weak shaking may re-aggregate in adjacent rock volumes, especially if the latter are bounded by an impermeable surface (like the case of the SAF at Parkfield, as documented by Malagnini and Parsons, 2020), decreasing rock permeability and the attenuation

parameter. The described effect has been observed in lab experiments by Liu and Manga (2009), who stated that lab experiments confirm that dynamic stresses and time-varying flow can change permeability, and both permeability increases and decreases may be possible.

Another physical mechanism responsible for the increased rock permeability (and seismic attenuation) indirectly observed after shaking is that of strong motion-induced rock damage (Kelly et al., 2013; Rubinstein and Beroza, 2005; Malagnini and Parsons, 2020). As shown along the SAF at Parkfield by Kelly et al. (2013) and Malagnini et al. (2019), rock damage heals over several years, most probably by the precipitation of minerals and colloidal particles into the crack network, and the consequent reduction of permeability.

In this paper we measure anelastic attenuation based on peak amplitude ratios calculated at two different hypocentral distances. Peak amplitudes are from weak- and strong-motion, narrowband-filtered time histories. Interpolations at specific hypocentral distances are calculated through simple regressions, made possible by a mathematical tool called Random Vibration Theory (Cartwright and Longuet-Higgins, 1956, see later). The latter, together with the Parseval equality, allows the use of the Convolution Theorem on peak amplitudes.

We suggest that the long-term variation of the attenuation parameter after one or more main shocks is caused by permanent crustal dilatation (increased or decreased compressional stress caused by the cumulative effect of the main earthquakes' static stress drops). In regions subjected to extensional tectonics, like the one struck by the 2016-2017 seismic sequence of Amatrice-Visso-Norcia (Central Apennines, Italy), the cumulative stress drop causes a permanent reduction of the attenuation parameter, and thus of the permeability within the crustal volume affected by the seismicity, confirming the conceptual model by Muir-Wood and King (1993).

Our working hypothesis is that crustal anelastic attenuation is closely related to the characteristics of the crack population that permeates crustal rocks. Whereas the crack-fluid interaction under the excitation of traveling stress waves represents a difficult problem to be

solved quantitatively, either numerically or analytically, it may be easier to propose meaningful physical interpretations about the nature of the variation of the empirical observation of attenuation changes over time. We note variations of $Q_S^{-1}(f,t)$ after the normal faulting earthquakes of the Central Apennines that show sharp drops after each main shock. Moreover, the cumulative effect of an entire seismic sequence is such that there is a notable and stable decrease of $Q_S^{-1}(f,t)$.

2 Data

The 2016-2017 Amatrice-Visso-Norcia (AVN) seismic sequence of the Central Apennines (Italy)

On 24 August 2016, at 01:36 UTC, an **M**5.97 earthquake struck the town of Amatrice. The main shock started a long seismic sequence characterized by two more main events (**M**5.87 Visso, on 26 October 2016, at 19:18 UTC, and the **M**6.33 Norcia, on 30 October 2016, at 06:40 UTC; Figure 1A). The seismic sequence affected a large region (see the seismicity distribution shown in Figure 1B), and lasted until the end of January 2017. On January 18, 2017, a sequence of smaller shocks (**M**5.43 was the largest shock) marched through the deep part of the Campotosto fault, with epicenter near Capitignano (e.g., Cheloni et al., 2019; Falcucci et., 2018; Gori et al., 2019), with four events with **M**>5 (Figure 1A). After the Capitignano subsequence, the seismic activity of the region faded away and returned to the background level by late 2017. A rough display of the spatio-temporal evolution of the seismic sequence is provided in Figure S1.

The AVN seismic sequence contained the largest earthquake ever recorded in the Central Apennines. The sequence was recorded by a dense modern network of seismometers and accelerometers, and the collected data set provides a unique opportunity to study earthquake-related phenomena in the region. Together with the one collected during the 2009 L'Aquila seismic sequence, the AVN data set allows us to study earthquake sources and wave propagation phenomena with unprecedented accuracy for this region.

The final data set used for attenuation calculations consisted of 3,236 earthquakes recorded by 67 weak-motion 3-component stations belonging to Rete Sismica Nazionale (RSN), run by Istituto

Nazionale di Geofisica e Vulcanologia (INGV, Figure 1B, see Catalog provided as a Supporting Information). Events were gathered in the period between 07/01/2013 and 31/08/2020 with 2.0<**M**<6.33. The data set also included 83 events recorded by the Rete Accelerometrica Nazionale (RAN) for a total of 9,905 strong-motion waveforms. Station list is provided as Supporting Information. This study is based on a total of 200,132 individual-component waveforms. The histograms in Figure 2 describe the distributions of the magnitudes (M_L) of the events in our data set, hypocentral depths, and hypocentral distances of the recorded seismograms.

We only used seismograms with one individual event, no glitches, no holes, and no spurious noise. Seismograms with multiple (overlapping) events were either cut in the time window containing the specific event only, or removed from the data set. A total of 200,132 seismograms were chosen from 3,236 earthquakes with $2 \leq M \leq 6.0$ occurring between January 7 2013 and August 20 2020 by visually inspecting a multitude of individual time histories by either Irene Munafò or Luca Malagnini. A signal-to-noise (S/N) ratio analysis was performed on the spectral content of each individual seismogram, as described by Malagnini et al. (2000). Also, during the sequence the magnitudes of the events in the data set are higher (and so is the S/N ratio). Finally, we used Random Vibration Theory in order to maximize the S/N ratio (we use peak values, not spectral amplitudes, see Malagnini and Dreger, 2016 for details). No noise issues can affect the variability of attenuation at low frequencies.

3 Methods

The technique used here evolved from the work by Raoof et al. (1999) and Malagnini et al. (2000), and is described by Malagnini et al. (2019) and Malagnini and Parsons (2020). The approach is based on a tool called Random Vibration Theory (RVT), developed by Cartwright and Longuet-Higgins (1956) for the analysis of tides, and subsequently widely used in ground motion analyses (e.g. Boore and Joyner, 1984). RVT allows the use of peak values of narrowband-filtered time histories in place of their Fourier amplitudes. Moreover, it allows using the Convolution Theorem for peak value analysis (for a detailed explanation, see Appendix A in Malagnini and Dreger, 2016). Exchanging Fourier amplitudes for peak values brings a huge improvement of the signal-

to-noise ratios of the data used in the regressions, which is key in studying the fluctuations of the attenuation parameter.

The disadvantage of using RVT is that we lose the information on the peak arrival time, because in theory the peak can occur anywhere in the time history. We worked around this drawback in two ways: (1) we prescribed that the analysis be performed in the time window marked by the S-wave arrival and a minimum group velocity (1.5 km/s; (2) we visually inspected all the seismograms of the data set. This required us to visually inspect about 300,000 seismograms to generate a data set of 200,000+ good waveforms without multiple events in a time history, glitches, spurious peaks, data gaps, etc.. We gathered progressive groups of 40 consecutive earthquakes from our catalog of 3,236 earthquakes by moving forward one earthquake at a time as P=M-C+1, yielding overlapping subsets of C ordered consecutive events (C=40 in our case). Malagnini et al. (2019), tried subsets of 80-60-50-40-30 events, and explored the tradeoff between relatively more stable results obtained using a larger number of waveforms, and the loss of time resolution that comes with a larger number of earthquakes. They showed that no significant quality increment could be obtained (in terms of stability) with more than 40 events, but below that number the attenuation results were unstable. The issue of stability of the results vs. their time resolution is not important during a seismic sequence, when events are frequent, large, and each of them is recorded by many stations. The issue becomes more important during "regular" times, when earthquakes are infrequent, small, and do not have many recordings.

For each subset of 40 earthquakes we repeat the following steps: i) filter the N seismograms of the subset around a set of K central frequencies, $\{f_{c_\kappa}\}_{\kappa=1,\dots,K}$; ii) extract the peak amplitudes (A_n) at all individual frequencies and arrange them in a matrix form (one independent matrix for each central frequency, one line for each filtered seismogram, with no cross-frequency smoothing); iii) run the K regressions on all central frequencies using (1).

$$A_n(r_{ij}, t_j, f_{c_k}) = SRC_j(r_0, f_{c_k}) + D(r_{ij}, r_0, t_m, f_{c_k}) + SITE_i(f_{c_k}) + \epsilon_n, \quad (1)$$

In (1), $SRC_j(r_0, f_{c_k})$ refers to the contribution of the jth source, normalized to a reference distance r_0, $SITE_i(f_{c_k})$ is the contribution of the ith site, and $D(r_{ij}, r_0, t_m, f_{c_k})$ is a path term that accounts for the effect of crustal propagation. Note that path and source terms in (1) are normalized by a reference distance.

The parameter t_m represents the origin time of the m-*th* event of the current subset of ordered consecutive earthquakes, and for this study we chose $m = 1$; r_{ij} is the hypocentral distance between the *i-th* recording site and the *j-th* earthquake; r_0 is an arbitrary reference distance (we use $r_0 = 10$ km).

The *n-th* row of the matrix (1) refers to the *n-th* observation, the *j-th* column refers to the *j-th* seismic source, the *i-th* column refers to the *i-th* station, and *k=1,…,44* refers to the *k-th* regression (one regression per central frequency f_{c_k}). Finally, ϵ_n is the residual between the observation and the sum of the three terms describing the ground motion (we drop it in what follows).

$$A_n(r_{ij}, t_j, f_{c_k}) = log_{10}(PEAK[a_n(r_{ij}, t_j, f_{c_k})]), \tag{2}$$

Term $a_n(r_{ij}, t_j, f_{c_k})$ in (2) is the narrowband-filtered version of the nth time history, relative to the ith station, and to the jth source. $PEAK[a_n(r_{ij}, t_j, f_{c_k})]$ in (2) indicates the peak value observed after the S-wave arrival and with a group velocity larger than 1.5 km/s; $t_j \neq t_m$ when $j \neq m$.

The inversion of (1) is performed after adding the following constraints:

$$D(r_{ij} = r_0, t_m, f_{c_k}) = 0, \tag{3}$$

$$\sum_{i=1}^{NSITE} [SITE_i(f_{c_k})]=0, \tag{4}$$

$$D_{l-1}(f_{c_k}) - 2D_l(f_{c_k}) + D_{l+1}(f_{c_k}) = 0, \quad (5)$$

$\sum$ where: $l = 0,1,\ldots,L$, and L is the number of nodes defining a continuous piecewise-linear path term in a log-log space.

Constraints (3) effectively decouples the path term (representing total attenuation) from the combination of source and site terms. The reader should keep in mind that our working hypothesis is that the crust is laterally homogeneous in the studied region. Although this hypothesis is never completely true, it has worked reasonably well in many areas of the world (see studies by Malagnini and colleagues, including those on source scaling, e.g., Mayeda and Malagnini, 2009, Malagnini and Mayeda, 2010, Malagnini et al., 2008). Constraint (4) decouples the site and source terms and gives physical meaning to the latter (i.e., the source terms that would be recorded at the reference distance r_0 by the average network site, see Malagnini et al., 2000). Constraint (4) has no effect on our results, and we include it for completeness. Constraint (5) is a smoothing operation applied to the crustal propagation term, which minimizes the roughness of the solution and has negligible effects on our results.

For completeness, we note that the number of stations may not be strictly the same for each earthquake, adding some variability from earthquake to earthquake. Yet, they always contribute to the null average site term because the latter is not forced individually on each earthquake, but through the inversion of the matrix (1). This is done by adding an extra row of zeros in all columns, except for all columns corresponding to the horizontal site terms, where we insert a large number, comparable to the number of data points. An extra zero is added to the column of the observed amplitudes.

By inverting matrix (1), we obtain one set of source spectra, one set of site terms, and one smooth path term for each central frequency. Because of constraint (3), the path term is equivalent to an amplitude ratio between the attenuation at distances r_{ij} and r_0, that can be modeled for any distance r as:

$$D\left(r_1, r_0, t_m, f_{c_k}\right) = \left[\frac{g(r_1)}{g(r_0)} exp\left(-\frac{\pi f(r_1 - r_0)}{V_S Q_S(t_m, f_{c_k})}\right)\right], \quad (6)$$

where g(r) is a static attenuation function, piecewise-linear in log-log space, r_0 is an arbitrary hypocentral distance used for normalization (3), $Q_S^{-1}(t_m, f)$ is a measure of time-dependent attenuation at t=t_m, which is the focus of our research, $r_1 = 40$ km is a second arbitrary hypocentral distance, and V_S is shear-wave velocity. Crustal propagation is spatially sampled at a fixed set of hypocentral distances, in the 10 - 150 km range.

Figure 3a shows the total attenuation term $D\left(r_1, r_0, t_m, f_{c_k}\right)$ at a subset of sampling frequencies, with the indication of the durations of each one of the *m* time windows (each one contains 40 events) used to scan the entire period (horizontal black segments in Figure 3a). Moreover, Figure 3b is a 2-D representation of the fluctuations of the seismic attenuation parameter around its average value, $\Delta Q_S^{-1}(t_m, f)$, with the indications of the events of the sequences with **M**≥4.5 (epicenters in map of Figure 3c). The time-averaged attenuation parameter $\langle Q_S^{-1}(f)\rangle$ is shown in Figure 3d (averages calculated in two consecutive time windows: pre- and post-Amatrice. Note the reduction in the average attenuation parameter in the second time window. Note also that $\langle Q_S^{-1}(f)\rangle$ is described by a power law at high frequencies, but flattens just below 1 Hz, indicating that below 1 Hz frequencies, surface waves dominate between the two distances that are arbitrarily chosen to calculate the attenuation parameter. We can safely state that above 1 Hz all the peak values of the narrowband-filtered time histories are carried by direct S-waves. To reduce the error bars of the attenuation function, we apply a bootstrap procedure, in which 10% of the events of each time window are removed from the data set. 10 different regressions are run on the data set associated to t_m, and the 10 attenuation parameters $(Q_S^{-1}(t_m, f)|_i,\ i = 1, \dots, 10)$ are averaged, obtaining smooth and reliable attenuation surfaces like those shown in Figure 4. A zoom on the most energetic part of the seismic sequence, between the Amatrice mainshock (08/24/2016) and 12/31/2016 is shown in Figure S3.

By calculating the average attenuation over time, removing the geometric attenuation calculated by Malagnini et al. (2011, their eq. (3)) for the adjacent region that was struck by the April 6 2009 L'Aquila earthquake, and subtracting it from eq. (6), we obtain anomalies of $Q_S^{-1}(t,f)$ that are plotted in Figure 4 (we drop the *m* subscript of the time variable from now on). The average is taken between 01/01/2013 (the beginning of our time window) and 23/08/2016 (the day before the Amatrice main shock) to enhance the effects of the seismic sequence. Finally, errors with respect to the average (d(log(1/Q)), calculated in the regressions for all time windows and for all frequencies, are shown in Figure S3.

Limitations of our approach

Scientific results must be thoroughly evaluated to understand hidden limitations of techniques. We point out the existence of issues of limited importance about the current application developed by Malagnini et al. (2019).

1. Trade-offs:

Tradeoffs are the inevitable drawback of any inverse problem. What we have available is equation (1), and the constraints that are forced onto the matrix. With such a limited set of tools, we are able to exploit our data set in many different ways, including the assessment of temporal variations of the site terms (Figure S4). Although some variability is inevitable, their collective behavior is totally acceptable for our purposes.

Yet, our results must be affected by unavoidable tradeoffs. As an example, if all sites simultaneously experienced the same amount of damage during some strong shaking, constraint (4) would force the changes in site attenuation that are common to all sites, through constraint (3), onto all source terms. Because shaking-related rock damage is a shallow consequence of earthquake-induced ground motion, we expect that an increase in site terms occurs at low frequency at the beginning of the sequence. Figure S4 documents such a change, which only affects a subset of recording stations and is counterbalanced by the rest of the sites.

Our working hypothesis may also look simple, but many studies demonstrated that it works in the Apennines, even in a region that is larger than the one struck by the 2016-2017 seismic sequence. The availability of seismometric data in the study area is enough to study the average behavior of the seismic attenuation, and its variability over time. Moreover, the sampled crustal volume (Figure 1) is large enough and well instrumented, so that a large number of stations sample the same crustal volume illuminated by the seismic events. This is especially true for the time window that includes the seismic sequence. In comparison, the time window between 01/01/2013 and 23/08/2016 shows a remarkably constant crustal attenuation pattern (except for the seasonal fluctuations, see Figures 3b and 4), in spite of the fact that in order to obtain enough events to have a decent time resolution we needed to select anything above M1.9 (i.e., scattered background seismicity).

Source and site terms are remarkably stable over the period between 01/01/2013 and 23/08/2016 (Figure S4), especially when compared to their behaviors during the sequence. It also appears that the more seismically active region of the Central/Northern Apennines between L'Aquila to Norcia, is (in relative terms) seismologically homogeneous, at least in terms of the velocity structure. For example, Herrmann et al. (2011) were successful in using the Central Italy Apennines (CIA) velocity model to reproduce broadband seismograms down to M2.8 - http://www.eas.slu.edu/eqc/eqc_mt/MECH.IT/). The broadband inversion of the moment tensors uses frequencies up to 0.15 Hz, that is, minimum wavelengths of 15-20 km.

We use a set of stations within 50 km of any of the mainshocks. Moreover, we always look at the same hypocentral distance of 40 km; earthquakes at larger distances can still contribute (mainly through the smoothing constraint (5)) to the value of D(r,f), yet they do so negligibly with respect to earthquakes at closer distance. We however looked at the same 1/Q plots at shorter and longer hypocentral distances (30 km and 80 km), obtaining virtually the same results (Figure S5 shows the variability of 1/Q at 80 km). Finally, regressions demonstrated to be extremely stable to random mislocations that are larger than the location precision (especially to outliers, see

Figure S6). The various arguments listed in the current subsection concur to establish confidence in our results.

2. Near-fault and off-fault effects:

The effect of seismic attenuation on observed amplitudes of ground motion refers to the integral of all the individual contributions experienced along the entire crustal path, from the immediate vicinity of the fault to the recording site. Because the effect is proportional to the duration that seismic waves are affected by some specific attenuation, we can write that:

$$\frac{T_{TOTAL}}{Q_{TOTAL}} = \frac{T_{NEAR-FAULT}}{Q_{NEAR-FAULT}} + \frac{T_{PATH}}{Q_{PATH}}. \quad (7)$$

As a consequence of (7), the fluctuations of Q in the fault zone could be larger than what we obtain. Note that the near-site contribution $\left(\frac{T_{SITE}}{Q_{SITE}}\right)$ is decoupled from that of the crustal propagation by constraint (3), and we do not need to take it into account. Also, the calculated value of $Q_S^{-1}(f,t)$ is an effective value that incorporates the effects of both processes of anelastic and scattering attenuation, and we do not attempt to discriminate between them. Lastly, we interpret the sharp increase in the seismic attenuation that occurs at low frequency after the onset of the Amatrice mainshock as the effect of rock damage at shallow depths, at or below 1.0 Hz in Figure 2 (lower frame) where surface waves dominate. Due to the nature of surface waves, we expect the effects of shaking-induced rock damage to extend down to less than a few hundred meters .

3. Causality:

We use overlapping subsets of 40 consecutive earthquakes, calculate the attenuation relative to each sub-set, and associate it to a specific time belonging to the time window spanned by the subset (in the current application, the time of occurrence of the first earthquake). Then the time window is shifted to the next earthquake available along the time axis, and a new subset of 40 earthquakes is obtained by including the 41st earthquake, and leaving out the first event. The second attenuation data point is calculated and associated to the occurrence time of the second

earthquake of the entire data set. There will be times in which the time window spanned by 40 consecutive earthquakes is very long, about half a year before 24 August 2016, but as soon as the first main shock hits Amatrice, the interevent times get very small, down to a fraction of an hour (Figure 3a).

When the moving window hits the first mainshock, for 39 more time steps we include its effects (damage and dilatation reduction) on the resulting attenuation data points. We have a causality issue for whatever the choice of the occurrence time to associate with a specific data point (we chose the first origin time of the original ordered subset of 40 events, regardless of the actions of the bootstrap analysis. Malagnini et al., 2019 chose the median origin time, and another possible choice could be the average origin time, etc). We break the data set into two parts, before Amatrice, and from the Amatrice mainshock onward to avoid acausal effects. After the first mainshock, the sampling of the attenuation parameter is fine enough that we do not need to apply this procedure any more times (acausality is always present, but during the sequence, the time windows are very short, and we can neglect it for our purposes).

To aid in interpretation of attenuation observations, we add independent lines of investigation. We calculate coseismic dilatation to gain insight into where post-earthquake extension and compression occur and associated inferred crack opening or closing. We additionally conduct simple calculations of expected changes in relative fluid flow magnitudes and directions based on dilatation. We also examine the catalog for seismic patterns in time and space that are consistent with fluid diffusion signals.

We calculate the coseismic dilatation caused by earthquakes during the 2016-2017 Amatrice-Visso-Norcia seismic sequence and the Capitignano subsequence by using a boundary element method. We use rupture plane definitions from local moment tensor solutions (see supplement for solutions and dislocations). Elastic dislocations are made from earthquake rupture areas and slip that are scaled according to the empirical regressions of Wells and Coppersmith (1994), and centered at reported hypocenters/centroids. We assume that all the events occurred on the

southwest-dipping nodal planes, which are the prevailing known rupture styles. Dilatation calculations are made using the subroutines of Okada (1992). Since we are calculating dilatation strain, no friction coefficient is necessary. Results are shown in Figure 5a, with much of the region showing relative negative dilatation (compression) following the seismic sequences. Additionally, we make calculations of static stress changes on the eventual Visso and Norcia mainshock ruptures utilizing available focal mechanisms of all events beginning with the Amatrice mainshock to immediately before the Visso, and then Norcia events (after Mancini et al., 2019). This is also done using the subroutines of Okada (1992), but rather than a half-space calculation, shear, normal, and Coulomb stress change calculations are resolved on the mainshock failure planes. This is done to assess the relative influence of fluid diffusion vs. direct coseismic triggering within the mainshock sequences.

Calculated changes to fluid flow directions indicate generalized migration of pore fluids away from the most negative dilatancy regions in the crust. Relative magnitudes and directions of radial flow (u_r) are calculated using Darcy's Law assuming porous flow within a confined aquifer as

$$u_r = \frac{k}{\mu}\frac{dp}{dr} \tag{8}$$

where k is the permeability of the porous rock, p is pore pressure change, r is radial distance, and μ is dynamic fluid viscosity. Here we are calculating expected relative change in subsurface flow rather than absolute values and assume that k and μ remain constant. Integrating this differential equation (e.g., Turcotte and Schubert, 1982), shows that this relation takes the form of

$$\Delta p = C\ ln\frac{r}{r_0} \tag{9}$$

where C represents assumed constants, r_0 is the position of the pressure change, and r is the location of an expected flow value at a given distance. We assume changes in dilatancy and/or normal stress are proportional to changes in pore pressure and calculate expected relative flow direction and magnitude from each cell in the model to all the others (Figure 5b).

We searched high-resolution catalogs (Tan et al., 2021) for earthquake sequences in time and space that demonstrate consistency with a diffusion signal. We found that below **M**3.5, there are too many events likely triggered through multiple processes (e.g., static stress changes, dynamic stress changes, diffusion) to reasonably identify a diffusion process. At thresholds above **M**3.5 it is possible to systematically search time windows of earthquakes sorted by time and distance from mainshocks to visually identify patterns that could represent diffusion. We then conduct least-squares regressions to see if sequences are well fit to a functional form of $d \propto t^{0.5}$, which is characteristic of fluid diffusion. These analyses do not conclusively prove the existence of a diffusion process but are used in concert with other observations such as sudden changes in attenuation, coseismic dilatation, and expected changes in fluid concentrations to demonstrate a consistent process.

4 Results

Diffusion signatures on the $Q_S^{-1}(f,t)$ time histories

Episodes of fluid diffusion are widespread in the Apennines (e.g., Malagnini et al., 2012; Miller et al., 2004). An interesting question is whether they are coupled, in a coincident fashion, with temporal variations of the attenuation parameter. Moreover, it is well known that pulses of pore-fluid pressure may trigger seismic failure by reducing a fault's shear strength. The mechanism is that the effective fault-normal stress is reduced by the counteracting effect of the fluid pressure (Terzaghi, 1923), thus reducing the fault strength (see, for example, Wang and Manga, 2010), and

an interesting scientific question is whether episodes of fluid diffusion (which can possibly cause fault weakening) have detectable signatures on the attenuation parameter. Here we show cumulative evidence to support this from observed temporal changes in seismic attenuation and space-time relations amongst **M**≥3.5 earthquakes coupled with modeled crustal dilatation, fault-plane stress changes and fluid flow changes.

Following the approach developed by Malagnini et al. (2019), and Malagnini and Parsons (2020), we calculated anomalies of $Q_S^{-1}(f,t)$ from the average functional form $\langle Q_S^{-1}(f)\rangle$ calculated between 01/01/2013 and 23/08/2016/ (from the beginning of the available time window to one day before the Amatrice main shock). Results are shown in Figure 4, separated in two different time windows to minimize important effects on acausality. The $Q_S^{-1}(f,t)$ time histories after the Amatrice and Norcia mainshocks event show some consistent features: after a short-lived, sharp negative drop there is a longer positive pulse followed by a gentle negative swing. The duration of these features appears to depend on magnitude, lasting longer after the larger Norcia event. We interpret the negative anomaly as the effects of the negative dilatation documented in Figure 3 (deep decreased permeability), and the positive one as the effects of damage-like increases of the crack density (and permeability) at shallow depth.

We note that high frequency waveforms are characterized by small anomalies, indicating that what we detect in our analysis tells us something about the characteristic lengths of the shallow spatial distribution of permeability. It is well-known that below 1.0 Hz surface waves dominate the ground motion at short distance (e.g., Malagnini et al., 2000), and so the dimensions of permeability elements (clusters of interconnected cracks) affecting attenuation must be comparable with the 0.5 Hz wavelength (1-4 km). At higher frequencies we sample deeper paths because only crustal S-waves enter the calculation, and the characteristic lengths of the permeability heterogeneity distribution are smaller and comparable with the sampling wavelengths. For instance, at around 2 Hz such characteristic length may be between 0.5 and 1.5 km.

An analysis over the first 12 hours after the Amatrice main event shows three diffusion branches that follow a functional form of $d \propto t^{0.5}$ in a distance-time plot (Figure 6). Diffusion phenomena (heat or fluid diffusion equations) must have this form (see Nur and Booker, 1971; Malagnini et al., 2012). The diffusion curves are fit to a $d \propto t^{0.5}$ curve using a least squares method that finds the best fitting diffusivity constant value (r^2 values are given on the figures). The diffusion patterns are not simple (upper-left frame of Figure 6) and have also been noted by others (e.g., Tung and Masterlark, 2018; Convertito et al., 2020). Groundwater changes were also noted during and after the Amatrice mainshock (e.g., De Luca et al., 2018). As stated by Malagnini et al. (2012) for the M6.1 L'Aquila earthquake of April 6, 2009, and for the sequence of three large aftershocks that occurred on the Campotosto-Monti della Laga and Vettore-Monte Bove faults, it is likely that the tendency of the Apennines to produce diffusive episodes of crustal pore fluids inhibits large main shocks in favor of sequences of smaller events. In other words, the fault ruptures earlier in its seismic cycle. The time history of the attenuation parameter in one narrow frequency band (2 Hz) is shown in the bottom frame of Figure 6, whereas the high-frequency time history shows fluctuations of moderate amplitude, the 2-Hz waveform shows a marked decrease (to less attenuation) that lasted a bit less than 6 hours, followed by a rebound towards normal values. It is interesting that the minimum of $Q_S^{-1}(f = 2\ Hz, t)$ happens ~ 2.5 hours after the main shock, and is followed by a large positive swing less than 3 hours after the main event.

The same analysis is performed on a 10-day period starting at the onset of the Visso main event of October 26, 2016 (Figure 7). The Norcia earthquake (M_L 6.5, **M** 6.33) is also included. The 2 Hz attenuation curve is characterized by a similar behavior as after the Amatrice shock. First, at the onset of each main event, the attenuation parameter plunges steeply, then it bounces back. The time scale is about 20 times wider than that following Amatrice (Figure 6), but the negative-positive swing after each main shock takes about 24 hours to complete, which is roughly twice the time it took for the same swing after the Amatrice main event. Figure 8 shows yet another interesting situation, where a separate small seismic sequence hits the Campotosto fault (Cheloni et al., 2019; Falcucci et al., 2018; Gori et al., 2019) with a series of four **M**5+ events that occurred

in less than 5 hours. The sequence migrates quickly southward along the fault with a clear diffusive signature. Potential diffusion pathways are highlighted by microseismicity from the high resolution relocated catalog of Tan et al. (2021), where fault structures are apparent in cross section view (Figure 9).

In the three cases documented in Figures 6,7,8, the diffusion coefficient is very large, up to $D \approx 2000$ m^2/sec for the faster diffusion branch activated by the Amatrice main shock (1-D diffusion). The smallest diffusion coefficient is found for the Capitignano subsequence ($D \approx 53$ m^2/sec). With the exception of the latter, whose subsequence occurred on the same Campotosto-Monti della Laga fault that saw a similar diffusion episode in 2009 with $D = 60$ m^2/sec (Malagnini et al. 2012), we find very high diffusion coefficients. We use the following equation, from Townend and Zoback (2000), to compute the rock permeability:

$$\kappa = D\eta\left(\phi\beta_f + \beta_r\right). \tag{1}$$

For a rock compressibility $\beta_r = 2 \cdot 10^{-11}$ Pa^{-1}, a fluid compressibility $\beta_f = 5 \cdot 10^{-10}$ Pa^{-1}, using a porosity $\phi = 0.05$, a viscosity $\eta = 1.9 \cdot 10^{-4}$ Pa-s, and a diffusion coefficient D in the range between 50 m^2/sec and 2000 m^2/sec (from the results shown in Figures 6,7,8), we estimate the crustal permeability along the activated fault systems to be in the range between $\kappa = 3 \cdot 10^{-13}$ m^2 and $\kappa = 1 \cdot 10^{-11}$ m^2. These estimates of rock permeability are much higher than the ones obtained for undamaged upper crust (typically between 10^{-17} m^2, and 10^{-16} m^2, Townend and Zoback, 2000), because they are relative to fresh main shock rupture zones. They are not extreme, though; for example, right after the Dobi extensional earthquake sequence in Central Afar, Noir et al. (1997) estimated a permeability $\kappa \approx 10^{-8}$ m^2.

The estimates of permeability provided above are relative to critically stressed faults that just ruptured, not to the off-fault rock matrix, where we expect that the negative dilatation due to normal-faulting earthquakes would reduce crack density and thus permeability. In other words, the values of permeability found here are relative to the crustal plumbing system in the epicentral region (fault planes outlined by the seismicity in Figure 9), in the sense described by Townend

and Zoback (2000), which is contained in a volume in which the bulk permeability has decreased due to the effect of the elastic stress drop from normal faulting earthquakes (Muir-Wood and King, 1993).

Seismic attenuation occurs during propagation through bulk crustal rocks, and it is unaffected by the variations of permeability of the regional plumbing network. On the contrary, because episodes of macroscopic diffusion like those documented in Figures 6,7,8, occur along critically stressed fault planes, their parameters cannot be used to compute rocks' bulk permeabilities.

Effects of cumulative dilatation on $Q_S^{-1}(f,t)$

In the hypothesis that time-dependent seismic attenuation depends on rock permeability, we expect associations between earthquakes and changes in $Q_S^{-1}(f,t)$ to be caused by crack closure/opening induced by static stress changes from moderate-to-large events that occurred at short distances (e.g., Muir-Wood and King, 1993). We note widespread relative coseismic compression in the aftermath of mainshocks during the seismic sequence and narrower zones of dilation along fault zones (Figure 5a). During the period between the Amatrice mainshock up to the Visso event, most of the crust is under compression just south of the Visso mainshock location. Inferred fluid flow patterns suggest northward migration away from the compressed zones (and perhaps along opened fault planes) towards the Visso area as well (Figure 5b). The Visso plane is calculated to mostly have a static stress increase from the cumulative effects of prior events (Figure 10), so it is difficult to assess the relative impacts of fluid diffusion vs. static stress change triggering. Fluid flow calculations on the Visso plane based on normal stress changes where fluids are expected to migrate away from zones of clamping and into unclamped zones (assuming a sealed fault zone) do imply flow to the north towards the eventual slip zone (Figure 10).

Similarly, after the Visso mainshocks the crust around them is calculated to have a primarily compressive effect with a small gap near the Norcia mainshock (Figure 5a). Calculated fluid flow

from just prior to the Norcia mainshock implies flow south towards the Norcia hypocenter as well (Figure 5b). The static stress change pattern on the Norcia rupture is complex (Figure 10) with about equal areas of Coulomb stress increase and decrease. Areas of peak slip are shown after Chiaraluce et al. (2017), which match reasonably well with the Coulomb stress increases and perhaps slightly better with changes in normal stress. Expected fluid flow changes on the fault plane from normal stress changes imply flow towards zones of greatest slip (Figure 10). The dominant postseismic signal is negative dilatation that is expected to be associated with crack closure, which causes fluids to migrate away from these regions (Figure 5b). This model is supported by water level and fluid diffusion observations that were made in the immediate periods following some of the larger earthquakes within the Amatrice-Visso-Norcia and Capitignano sequences (e.g., De Luca et al., 2018; Petitta et al., 2018). Moreover, Chiarabba et al. (2020) also supported the idea that increased fluid pressure weakened the slip patches of the fault plane of the Norcia main shock.

Discussion

Multiple physical processes are likely responsible for temporal changes in seismic attenuation, so we must thus consider multiple coseismic effects from earthquakes as we attempt to understand the observed signals that accompany seismicity. If we were to compile a list of all the things that could cause a change in Q, we would need to include many different characteristics of the specific crustal volume under investigation: thermal state, fracture density, changes in consolidation, fluid saturation, etc. Here we argue that the two most likely post-earthquake causes of fluctuations in the attenuation parameter are represented by the effects that rock dilatation (from the cumulative stress drop from the earthquakes of the sequence) and damage (from strong shaking) induce on the mobility of pore fluids within bulk rocks. Negative dilatation and damage occur simultaneously in two different ranges of depth: while dislocation-induced dilatation acts on the crustal volume around nucleation (depth~6-8 km), stress wave-induced damage is a shallow phenomenon (depth<1 km, see Kelly et al., 2013).

After a strong earthquake, we observe two competing effects of opposite signs that alternatively dominate the attenuation parameter in different time windows: damage (increase of permeability and attenuation), and increased/decreased compression (decrease/increase of permeability and attenuation). Our results indicate that the attenuation parameter $Q_S^{-1}(f,t)$ is very sensitive to fluid mobility (intra- and inter-crack) and to fluid saturation, and, together with the theoretical work by O'Connell and Budiansky (1977), strongly support the idea that seismic attenuation is intimately linked to crustal bulk (not fault) permeability. From our results, it follows that crustal permeability is modulated by variations in the compressional stress (e.g., the post-earthquake compression that occurs in normal tectonics, see Muir-Wood and King, 1993), and that fluid viscosity is the reason why a substantial portion of seismic energy goes into heat in the crust. More compression must correspond to less seismic attenuation, and vice-versa. Our analysis is extremely simple and can be summarized by just eq. (1), making artifacts very easy to spot.

Moreover, if permeability and attenuation are linked, then the sudden coseismic increases of $Q_S^{-1}(f,t)$ observed at low frequency in Figures 3 and 4 is likely the result of an increase in crack density and interconnection (permeability) associated with damage produced by the strong-motion surface waves radiated by the three main shocks of the sequence. Whereas we are unable to bring direct quantitative proof of the effects of damage, we rely on the results of other studies (e.g., Chen et al., 2015; Kelly et al., 2013; Rubinstein and Beroza, 2005). Our calculations show a sizeable and stable overall decrease in the attenuation parameter $Q_S^{-1}(f,t)$ before the seismic sequence and after the sequence ends, which corresponds to the negative cumulative dilatation caused by the elastic stress drop from the Central Apennines sequence of normal faulting earthquakes (Amatrice-Visso-Norcia, see Figure 5a). Note that the negative dilatation of Figure 5a is calculated at 5 km in depth, and that it corresponds to a reduction in the crack density of crustal rocks.

It is important to consider that we analyzed seismic attenuation at a 40 km hypocentral distance, and verified that the 1/Q variations were virtually identical at an 80 km hypocentral distance

(Figure S5), as well as at a 30 km hypocentral distance (not shown). We conclude that the observed variability over time of high-frequency observations of 1/Q must be relatively deep (hypocentral depths are 5-9 km). At frequencies f $\leq$ 1 Hz, it is likely that surface waves start dominating the seismograms (see the flattening of the average 1/Q(f) below 1.0 Hz in Figure 3d), and they sample a shallower portion of the crust. We can estimate the minimum depth by considering that we use a minimum group velocity of 1.5 km/s. At 1.0 Hz, which has a 1.5-km wavelength. A meaningful maximum value for surface-wave group velocities at 1.0 Hz could be around 3 km/s. As a rule-of-thumb, surface waves sample the crust to 1/3 of their length, and so we conclude that, at frequencies below 1 Hz, we obtain information on the attenuation between a few hundred meters and 1 km depth.

In the immediate aftermath of a mainshock, the competition between shallow rock damage and negative dilatation at depth is evident at intermediate frequencies where a short-lived increase of the parameter $Q_S^{-1}(f,t)$ is probably related to shallow rock damage, and is followed by a stable decrease of the same parameter (deeper crack closure). Zooming in on short intervals (0.5-10 days) immediately after mainshocks (i.e., Amatrice, Visso-Norcia, Capitignano), we see a consistent pattern (Figures 6,7,8). Each mainshock that initiates a sequence is associated with a sharp increase in $Q_S^{-1}(f,t)$ followed by a comparatively steep drop (Figures 6,7,8, 11, 12, and S2). We observe coincident distance (d) and time (t) behavior of **M**≥3.5 earthquakes that is consistent with fluid diffusion, where $d \propto t^{0.5}$ (Figures 6,7,8). A subsequent gradual recovery of $Q_S^{-1}(f,t)$ persists up until the next mainshock (Figure 12). We hypothesize that this recovery is associated with the redistribution of fluids into newly damaged faults and into the shallow crust where bubble production induced by traveling stress-waves may also cause significant attenuation (Tisato et al., 2015).

We argue that a dislocation-induced pressure front generated by a large earthquake and its largest aftershocks could trigger another mainshock on either a nearby fault, or on an adjacent, locked patch of the same fault. The new event could even propagate the pressure front further

away, not necessarily in the same direction, starting a cascade of events. In fact, in multi-mainshock seismic sequences like the ones that struck the Apennines, multiple cycles of sudden attenuation drops, and more gentle attenuation recoveries suggest that multiple mainshocks may be triggered by intermittent episodes of fluid migration.

For example, we note that the Visso and Norcia earthquakes both lie on the same diffusion curve (Figure 7), meaning that it is possible that increased fluid pressure played a role in triggering the largest earthquake in the Central Apennines sequence. High-resolution catalogs of relocated earthquakes (e.g., Tan et al. 2021) highlight fault surfaces that likely act as high-permeability fluid pathways (Figure 9). The described mechanism could produce the occurrence of multi-mainshock sequences, in the Central Apennines as well as in any other extensional environment. As hypothesized by Malagnini et al. (2012), the induced fluid migration could also favor the segmentation of a major earthquake in multiple ruptures of smaller magnitudes.

Finally, a similar process could drive the preparatory phase of an isolated mainshock, where an individual fracture grows preferentially at the expense of the rest of the fracture population within the same crustal volume. Tectonic stress would concentrate on the growing crack, while relaxing within the adjacent crustal volume. The resulting reduction in crack porosity and the generalized closing of fractures and cracks in the volume surrounding the growing dominant fracture would cause a reduction in seismic attenuation, an increase in pore-fluid pressure, and a migration of pore fluids. The process would culminate with the occurrence of the first main shock.

Open questions:

1. Why is crustal attenuation extremely sensitive to bulk compression/dilatation? Malagnini et al., (2019) used the results by Johnson et al. (2017) and demonstrated that, at 2-4 km in depth on the SAF at Parkfield, the attenuation parameter responds to normal stress cyclic anomalies across the fault of the order of ~ 100 Pa. The extreme sensitivity indicates that it is the ground

motion noise that dominates the random fluctuations that affect our measurements, and not fluctuations of the physical properties of crustal rocks. Once we reduce the noise to a sufficiently low level, we only see the fluctuations of rock permeability. This demonstrates that other physical properties of crustal rocks are very stable over time. This is especially important for analyzing the effects of long-period stress periodicities, like the ones associated with seasonal loading and unloading from precipitation, multi-year wet-dry cycles, the polar tide, or solid Earth tides with multiple and submultiple periods of 28 days.

2. The most important aspect of this research is the potential use of our results for monitoring purposes, where precursory phenomena of large earthquakes might be detected. In fact, the evolution of the crustal crack distribution yields information about variations in strength of some portions of the crust under mounting tectonic stress, where stress tends to concentrate before a crustal rupture. If observed fluctuations of the attenuation parameter are directly linked to variations in the crack density, the latter must be in direct connection with variations of strength.

We note that Italy already has a high-quality seismic network (the Rete Sismica Nazionale, RSN). If the station density of the RSN was improved by an order of magnitude, we would be able to monitor the variability of the attenuation parameter of small regions of specific interest. At least, it would become possible to monitor localized anomalies in the attenuation parameter. Borehole stations would allow a much lower magnitude threshold than the one used here $(M \geq 2)$ for high-quality recordings of small earthquakes, allowing a finer spatial and temporal resolution in our monitoring purposes.

A much denser seismic network made of borehole instruments could produce a huge volume of high-quality recordings, and AI algorithms would have to be developed for the quality control of the recorded waveforms. They could be run in quasi-real time, in parallel with multi-frequency sets of regressions like the one presented here. The goal would be to use such tools to locate attenuation anomalies in space and time, in a quest for precursory phenomena.

5 Conclusions

The characteristics of the attenuation parameter (Figures 3, 4, 11, and 12) confirm the conceptual model formulated by Malagnini and Parsons (2020), that the time variations in rock permeability modulate the variability of the attenuation parameter. In fact, Figures 3d and 4 show that the average level of the background attenuation parameter between January 2013 and immediately prior to the onset of the sequence, on August 24, 2016, is higher than the background value after the sequence. Figure 5a shows that the cumulative effect of the seismic sequence (the multiple main shocks) on the study area was a negative dilatation (relative increase in compression); such an effect favored crack closure, and thus a decrease in permeability, and in anelastic attenuation as well.

The Central Apennines is a region under extensional tectonics, prone to multi-mainshock seismic sequences behaving like a cascade of several mainshocks: for example the 2016-2017 seismic sequence studied here, the Umbria-Marche sequence (swarm) of 1997-1998 (Miller et al., 2004; Amato et al., 1998), and the episode that occurred during the 2009 L'Aquila-Campotosto-Monti della Laga sequence (Malagnini et al., 2012).

Here we propose a possible physical mechanism for a cascade of multiple main shocks under extensional tectonics. We envision two main phases: 1) a pre-seismic phase that lasts up to the first earthquake and 2) intermediate phases, which may be cycled through several times, one for each subsequent main shock. In the first phase, the dilatancy model (Scholtz, 2019) predicts that at some point the preferential growth of one fracture takes place at the expense of the general population of cracks that tend to close during this preliminary phase. Such behavior must have consequences on pore fluid pressure, which changes as stress affects cracks. Pore-fluid drops imply fault strengthening, and inhibit rupture. Conversely, pore-fluid pressure rises imply fault weakening, and promote rupture. In the intermediate phases that start at mainshock onsets, two main physical processes compete in defining the attenuation parameter, rock permeability and, consequently, pore-fluid pressure. These processes are damage and negative dilatation (stress

drop). While damage would correspond to a drop in pore-fluid pressure in the shallow crust, negative dilatation and healing correspond to a deeper pore-pressure rise.

Muir-Wood and King (1993) observed that, in an extensional environment, the seismic stress drop of a main event always increases stream discharge, up to an order of magnitude more in volume than a reverse-fault mainshock of the same magnitude. This is because the elastic stress drop tends to close cracks oriented orthogonally to the (horizontal) direction of the minimum principal stress, causing a sudden increase in the pore-fluid pressure. A similar crack closure (pressure rise) may be envisioned in the pre-seismic phase, in which dilatancy predicts the preferential growth of one crack that is favorably oriented to the stress field, at the expense of the general population of cracks that during this preliminary phase tends to close.

Our conceptual model may be described as follows:

1. During the pre-seismic rupture growth in an extensional environment there may be a "*slow*" localized negative dilatation, crack closure, pore-pressure rise and migration (diffusion) along fault, and a resulting decreased fault strength that leads to the first main rupture. In all that we describe, permeability must be low enough to support local pore pressure increases, probably over a time scale of several weeks or months.
2. The first main event produces coseismic damage and negative dilatation: while the first causes a fluid pressure drop (short-lived), the second causes a fluid pressure rise (persistent); $1/Q_S$ shows opposite behavior. In turn, the fluid pressure rise and migration (diffusion) is responsible for the strength reduction in nearby faults, and the occurrence of the next earthquake. The cycling over a number of cascading main events ends when the system is depleted of its elastic energy below a certain threshold, when it is not able to produce any more ruptures.

Acknowledgments, Samples, and Data

Funding:

Progetti INGV di Ricerca Libera 2019 (LM), Progetto INGV "Pianeta Dinamico" (LM), Centro di Pericolosità Sismica, Triennio 2019-2021 Convenzione B1 Dipartimento della Protezione Civile – INGV (IM).

Competing interests: Authors declare that they have no competing interests

Data and materials availability: All seismometric data are available at the European Integrated Data Archives (EIDA, https://www.orfeus-eu.org/data/eida/); all accelerometric data are available at the ITACA data center (http://itaca.mi.ingv.it/ItacaNet_31/#/home).

References

1. Akinci E. Del Pezzo, and L. Malagnini (2020). Seismic Wave Attenuation and Scattering in the Central Apennines (Italy), *Physics of the Earth and Planetary Interiors*, https://doi.org/10.1016/j.pepi.2020.106498.
2. Amato, A., et al. (1998). The 1997 Umbria-Marche, Italy, earthquake sequence: A first look at the main shocks and aftershocks, *Geophys. Res. Lett.*, **25**, 2861– 2864.
3. D.M. Boore, and W.B. Joyner (1984). A note on the use of random vibration theory to predict peak amplitudes of transient signals, *Bull. Seism. Soc. Am*. 74 (5): 2035–2039.
4. Brodsky, E.E, E. Roeloffs, D. Woodcock, I. Gall, and M. Manga (2003). A mechanism for sustained groundwater pressure changes induced by distant earthquakes. *J. Geophys. Res.* 108, 2390.
5. Barbosa, N.D., J. Hunziker, S. Lissa, E.H Saenger, and M. Lupi (2019). Fracture unclogging: A numerical study of seismically induced viscous shear stresses in fluid-saturated fractured rocks, J. Geophys. Res., 124, 11, pp 11705-11727, https://doi.org/10.1029/2019JB017984.
6. Cartwright, D.E., and M.S. Longuet-Higgins (1956). The statistical distribution of the maxima of a random function, *Proc. R. Soc. Lond. A*, 237**,** 212–232, https://doi.org/10.1098/rspa.1956.0173.
7. Cheloni, D., N. D'Agostino, L. Scognamiglio, E. Tinti, C. Bignami, A. Avallone, R. Giuliani, S. Calcaterra, P. Gambino, and M. Mattone (2019). Heterogeneous behavior of the Campotosto normal fault (Central Italy) imaged by InSAR GPS and Strong-Motion Data:

Insights from the 18 January 2017 events, Remote Sens. 2019, 11, 1482, doi: 10.3390/rs11121428.

8. Chen, K.H., T. Furumura, and J. Rubinstein (2015). Near-surface versus fault zone damage following the 1999 Chi-Chi earthquake: Observation and simulation of repeating earthquakes, J. Geophys. Res., 120, 4, 2426-2445, https://doi.org/10.1002/2014JB011719.

9. Chiarabba, C., De Gori, P., Segou, M., and Cattaneo, M., 2020, Seismic velocity precursors to the 2016 Mw 6.5 Norcia (Italy) earthquake: Geology, v. 48 (9): 924-928, https://doi.org/10.1130/G47048.1.

10. Chiarabba, C., D. Piccinini, and P. De Gori (2009), Velocity and attenuation tomography of the Umbria Marche 1997 fault system: Evidence of a fluid-governed seismic sequence https://doi.org/10.1016/j.tecto.2009.04.004

11. Chiaraluce, L., R. Di Stefano, E. Tinti, L. Scognamiglio, M. Michele, E. Casarotti, M. Cattaneo, P. De Gori, C. Chiarabba, G. Monachesi, A. Lombardi, L. Valoroso, D. Latorre, and S. Marzorati (2017), The 2016 Central Italy Seismic Sequence: A First Look at the Mainshocks, Aftershocks, and Source Models, Seismological Research Letters, 88, 757-771, doi: 10.1785/0220160221.

12. Convertito V, De Matteis R, Improta L and Pino NA (2020), Fluid-Triggered Aftershocks in an Anisotropic Hydraulic Conductivity Geological Complex: The Case of the 2016 Amatrice Sequence, Italy, Front. Earth Sci. 8:541323, doi: 10.3389/feart.2020.541323.

13. De Luca, G., G. Di Carlo, and M. Tallini (2018), A record of changes in the Gran Sasso groundwater before, during and after the 2016 Amatrice earthquake, central Italy, Scientific Reports, 8:15982, DOI:10.1038/s41598-018-34444-1.

14. Falcucci, E., S. Gori, C. Bignami, G. Pietrantonio, D. Melini, M. Moro, M. Saroli, and F. Galadini (2018). The Campotosto seismic gap in between the 2009 and 2016-2017 seismic sequences of Central Italy and role of inherited lithospheric faults in regional

seismotectonic settings, *Tectonics*, 37, 2425-2445. https://doi.org/10.1029/2017TC004844.

15. Gori, S., I. Munafò, E. Falcucci, M. Moro, M. Saroli, L. Malagnini, and F. Galadini (2019). Active faulting and seismotectonics in central Italy: lesson learned from the past 20 years of seismicity. Engineering clues, Earthquake Geotechnical Engineering for Protection and Development of Environment and Constructions-Silvestri & Moraci (Eds), ISBN 978-0-367-14328-2.

16. Hoshiba, M. (1995). Estimation of nonisotropic scattering in western Japan using coda wave envelopes' Application of a multiple nonisotropic scattering model, *J. Geophys. Res.* 100, B1, 645-657.

17. Kelly, C. M., A. Rietbrock, D. R. Faulkner, and R. M. Nadeau (2013). Temporal changes in attenuation associated with the 2004 M6.0 Parkfield earthquake*, J. Geophys. Res. Solid Earth,* 118, 630–645, doi:10.1002/jgrb.50088.

18. Kilb, D., G. Biasi, J. Anderson, J. Brune, Z. Peng, and F.L. Vernon (2012). A Comparison of Spectral Parameter Kappa from Small and Moderate Earthquakes Using Southern California ANZA Seismic Network Data, *Bull. Seism. Soc. Am.,* 102 (1): 284–300, https://doi.org/10.1785/0120100309.

19. Johanson, I. A., and R. Bürgmann (2010), Coseismic and postseismic slip from the 2003 San Simeon earthquake and their effects on backthrust slip and the 2004 Parkfield earthquake, *J. Geophys. Res,.* **115**, B07411, doi:10.1029/2009JB006599.

20. Johnson, C. W., Fu, Y., and R. Bürgmann (2017). Stress models of the annual hydrospheric, atmospheric, thermal, and tidal loading cycles on California faults: Perturbation of background stress and changes in seismicity. *J. Geophys. Res. Solid Earth,* 122, 10,605–10,625. https://doi.org/10.1002/2017JB014778

21. Liu, W., and M. Manga (2009). Changes in permeability caused by dynamic stresses in fractured sandstone*, Geophys. Res. Lett.,* 36, L20307, doi:10.1029/2009GL039852.

22. O'Connell, R. J., and B. Budiansky (1977), Viscoelastic properties of fluid-saturated cracked solids, J. Geophys. Res., 82, 5719-5735.

23. Malagnini, L., and T. Parsons (2020). Seismic attenuation monitoring of a critically stressed San Andreas fault, *Geophys. Res. Lett.,* https://doi.org/10.1029/2020GL089201.

24. Malagnini, L., Dreger, D. S., Bürgmann,R., Munafò, I., & Sebastiani, G. (2019). Modulation of seismic attenuation at Parkfield, before and after the 2004 M6 earthquake. *J. Geophys. Res.*: Solid Earth,124, 5836–5853. https://doi.org/10.1029/2019JB017372.

25. Malagnini, L., and D.S. Dreger (2016). Generalized Free-Surface Effect and Random Vibration Theory: a new tool for computing moment magnitudes of small earthquakes using borehole data, *Geophys. J. Int.,* **206**, 103-113. doi: https://doi.org/10.1093/gji/ggw113.

26. Malagnini, L., F. Lucente, P. De Gori, A. Akinci, and I. Munafo' (2012). Control of Pore-Fluid Pressure Diffusion on Fault Failure Mode: Insights from the 2009 L'Aquila Seismic Sequence, J. Geophys. Res. 117, ISSN: 0148-0227, doi: 10.1029/.2011JB008911.

27. Malagnini, L., A. Akinci, K. Mayeda, I. Munafo', R.B. Herrmann, and A. Mercuri (2011). Characterization of Earthquake-Induced Ground Motion from the L'Aquila Seismic Sequence of 2009, Italy, Geophys. J. Int., Geophys. J. Int. 184, 325–337, DOI: 10.1111/j.1365-246X.2010.04837.x.

28. Malagnini, L., Herrmann, R.B., and M. Di Bona (2000). Ground motion scaling in the Apennines (Italy). *Bull. Seism. Soc. Am.*,90, 1062-1081.

29. Mancini, S., M. Segou, M. J. Werner, and C. Cattania (2019), Improving physics-based aftershock forecasts during the 2016-2017 central Italy earthquake cascade, J. Geophys. Res. 124, doi:10.1029/2019JB017874.

30. Manga,M., I. Beresnev, E. E. Brodsky, J. E. Elkhoury, D. Elsworth, S. E. Ingebritsen, D. C. Mays, and C.-Y.Wang (2012), Changes in permeability caused by transient stresses: Field observations, experiments, and mechanisms, Rev. Geophys., 50, RG2004, doi:10.1029/2011RG000382.

31. Manga, M., and E. Brodsky, Seismic triggering of eruptions in the far field: Volcanoes and geysers. Annu. Rev. Earth Planet. Sci. 34, 263–291 (2006).
32. Miller, S., Collettini, C., Chiaraluce, L. *et al.* (2004). Aftershocks driven by a high-pressure CO_2 source at depth. *Nature* **427,** 724–727, https://doi.org/10.1038/nature02251.
33. Mitchell, B.J. (1995). Anelastic structure and evolution of the continental crust and upper mantle from seismic surface wave attenuation, Reviews of Geophysics, 33, 4, 441-462, https://doi.org/10.1029/95RG02074.
34. Muir-Wood, R., and G.C.P. King (1993). Hydrological Signatures of Earthquake Strain, J. Geophys. Res., 98, B12, 22035-22068.
35. Noir, J., E. Jacques, S. Békri, P. M. Adler, P. Tapponnier, and G. C. P. King (1997). Fluid flow triggered migration of events in the 1989 Dobi Earthquake sequence of central Afar, Geophys. Res. Lett., 24(18), 2335–2338, doi:10.1029/97GL02182.
36. Nur, A., and J. R. Booker (1971). Aftershocks Caused by Pore Fluid Flow?, Science, 175, 885-887, doi: 10.1126/science.175.4024.885.
37. Parsons, T., L. Malagnini, and A. Akinci (2017). Nucleation speed limit on remote fluid-induced earthquakes, Science Advances, Sci. Adv. 3 (8), e1700660, https://doi.org/10.1126/sciadv.1700660.
38. Petitta, M., L. Mastrorillo, E. Preziosi, F. Banzato, M.D. Barberio, A. Billi, C. Cambi, G. De Luca, G. Di Carlo, D. Di Curzio, C. Di Salvo, T. Nanni, S. Palpacelli, S. Rusi, M. Saroli, M. Tallini, A. Tazioli, D. Valigi, P. Vivalda, and C. Doglioni (2018). Water-table and discharge changes associated with the 2016–2017 seismic sequence in central Italy: hydrogeological data and a conceptual model for fractured carbonate aquifers. *Hydrogeol J* **26,** 1009–1026. https://doi.org/10.1007/s10040-017-1717-7
39. Raoof, M., R.B. Herrmann, and L. Malagnini (1999). Excitation of three-component ground motion in Southern California, Bull. Seism. Soc. Am., 89, 888-902.
40. Roeloffs (1998). Persistent water level changes in a well near Parkfield, California, due to local and distant earthquakes, J. Geophys. Res., 103 B1, 869-889.

41. Rubinstein, J. L. and G. C. Beroza (2005), Depth Constraints on Nonlinear Strong Ground Motion from the 2004 Parkfield Earthquake, GRL, vol. 32, L14313, doi: 10.1029/2005GL023189.

42. Scholz, C. (2019). *The Mechanics of Earthquakes and Faulting*. Cambridge: Cambridge University Press. doi:10.1017/9781316681473.

43. Silverii, F., N. D'Agostino, A.A. Borsa, S, Calcaterra, P. Gambino, R. Giuliani, M. Mattone (2018). Transient crustal deformation from karst aquifers hydrologyi n the Apennines (Italy), Earth Planet. Sci. Lett., 506, 23–37, https://doi.org/10.1016/j.epsl.2018.10.019.

44. Tan, Y. J., F. Waldhauser, W. L. Ellsworth, M. Zhang, W. Zhu, M. Michele, L. Chiaraluce, G. C. Beroza, and M. Segou (2021), Machine-Learning-Based High-Resolution Earthquake Catalog Reveals How Complex Fault Structures Were Activated during the 2016–2017 Central Italy Sequence, The Seismic Record, 1, 11–19, https://doi.org/10.1785/0320210001

45. Terzaghi, K. (1923). Die Berechnung der Durchassigkeitsziffer des Tones aus dem Verlauf der hydrodynamischen Spannungsercheinungen*, Sitzungsber. Akad. Wiss. Wien Math. Naturwiss. Kl.*, Abt. 2A, 132, 105-124, 1923.

46. Tinti, E., P. Spudich, and M. Cocco (2005). Earthquake fracture energy inferred from kinematic rupture models on extended faults, J. Geophys. Res., 110, B12303, doi:10.1029/2005JB003644.

47. Tisato, N., B. Quintal, S. Chapman, Y. Podladchikov, J-P. Burg (2015). Bubbles attenuate elastic waves at seismic frequencies: First experimental evidence, Geophys. Res. Lett. 42, 3880-3887, https://doi.org/10.1002/2015GL063538.

48. Titzschkau, T., M. Savage, and T. Hurst (2010). Changes in attenuation related to eruptions of Mt. Ruapehu Volcano, New Zealand, Journal of Volcanology and Geothermal Research, 190, 1–2, pp. 168-178, https://doi.org/10.1016/j.jvolgeores.2009.07.012.

49. Townend, J., and M.D. Zoback (2000). How faulting keeps the crust strong, GEOLOGY, 28 (5): 399.

50. Tung, S., and Masterlark, T. (2018). Delayed poroelastic triggering of the 2016 October Visso earthquake by the August Amatrice earthquake, Italy. Geophysical Research Letters, 45, 2221–2229. https://doi.org/10.1002/2017GL076453

51. Wang, C.-Y., and M. Manga (2010). Hydrologic responses to earthquakes and a general metric, *Geofluids* (2010) **10**, 206–216, https://doi.org/10.1111/j.1468-8123.2009.00270.x.

52. Wells, D. L., and K. J. Coppersmith (1994), New empirical relationships among magnitude, rupture length, rupture width, rupture area, and surface displacement, Bull. Seismol. Soc. Am., 84, 974– 1002.

53. Winker, K.W. and A. Nur (1982). Seismic attenuation: Effects of pore fluids and frictional-sliding, *Geophysics,* 47, 1-15, https://doi.org/10.1190/1.1441276.

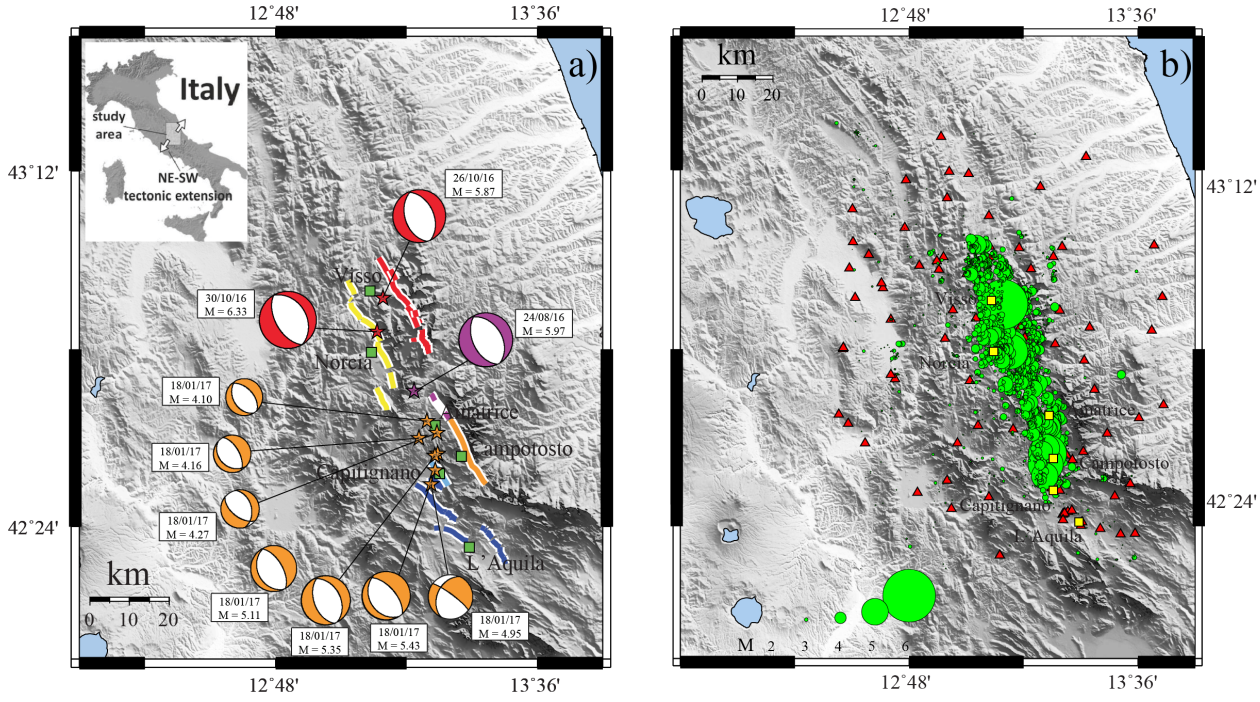

Figure 1. Representation of the data set. a) Mechanisms of selected earthquakes, including the mainshocks of the Amatrice, Visso and Norcia and the major seven events of Capitignano sequence (from http://eqinfo.eas.slu.edu/eqc/eqc_mt/MECH.IT/). Fault traces are represented by colored lines (fault strands with the same color pertain to the same seismogenic fault system, from Gori et al., 2019). Fault systems are matched with the corresponding focal solutions using the same color; stars correspond to the location of the mainshocks, whereas white squares represent the main cities of the area. **b)** Locations and magnitudes of the 3,236 earthquakes used

in this study (2.0 < **M** < 6.33) occurred in the time window between 07/01/2013 and 31/08/2020; gray squares indicate the main cities of the area.

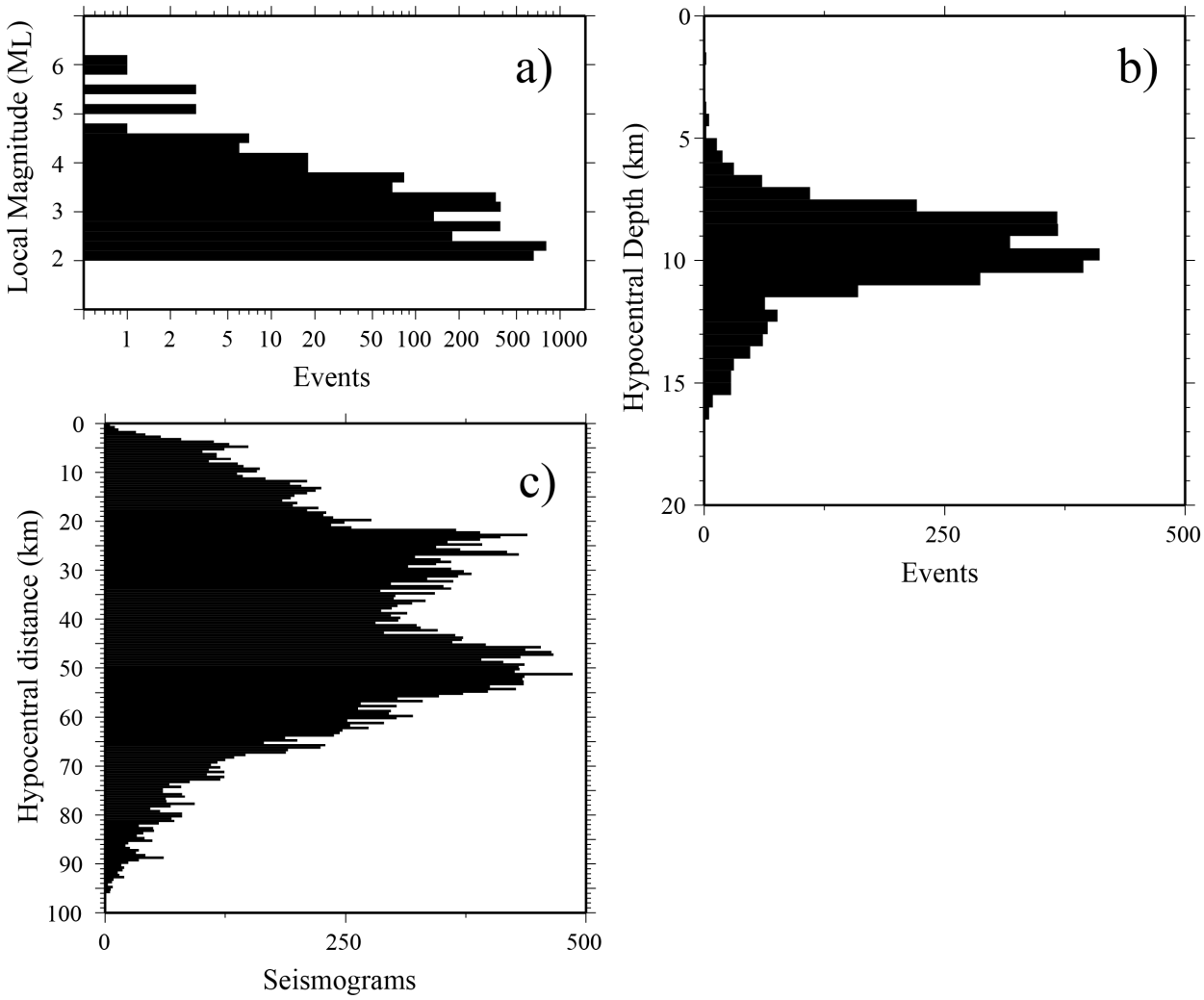

Figure 2. Histograms describing our data set: **a)** local magnitudes (M_L); **b)** hypocentral depths; **c)** source-receiver hypocentral distances.

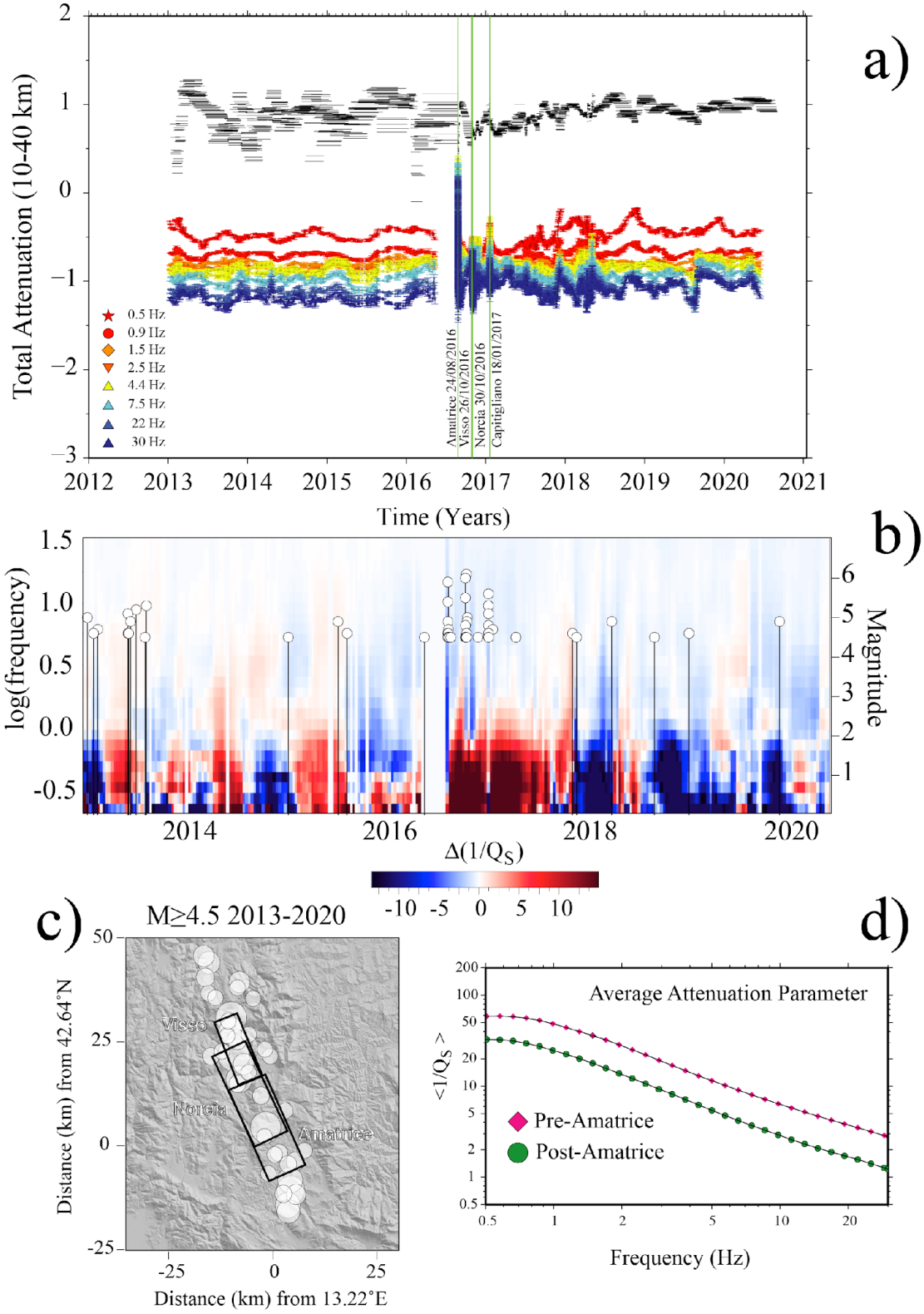

Figure 3. a) Colored symbols: total attenuation (geometric and anelastic) calculated between 10 and 40 km of hypocentral distance in the Central Apennines, before, during, and after the 2016-2017 sequence. Horizontal black segments: durations of each one of the *m* time windows (each

one contains 40 events) used to scan the entire period (horizontal black segments. Indicated are the main shocks of Amatrice, Visso and Norcia. Malagnini et al. (2019) and Malagnini and Parsons (2020) hypothesized that the fluctuations of $Q_S^{-1}(t,f)$ over time as linked to stress-induced fluctuations of crack density and connectivity. That is, to variations of rock permeability. Within such a hypothesis, earthquake-generated stress waves induce cyclic movements of rock fluids through variable compressions of the cracked rock matrix. Along permeable paths of interconnected cracks, seismic waves induce fluid flows of lengths comparable to their wavelengths: high-frequency seismic waves act only on comparatively short paths of interconnected cracks, low-frequency seismic waves can affect longer paths, and the two situation would be differently efficient in attenuating seismic waves, because although they would be dominated by different loading times, the circulating fluid would be the same, and its viscosity would be constant. **b)** Two-D representation of the attenuation parameter $Q_S^{-1}(t,f)$, which indicated the magnitudes and times of occurrence of events with **M**≥4.5. The frequency axis is in log scale. **c)** Epicentral locations of the events with **M**≥4.5 indicated in **b)**. Rectangles indicate the approximate ruptures of the three main shocks of the sequence. **d)** Time-averaged attenuation parameters $\langle Q_S^{-1}(f)\rangle$ calculated in the pre-Amatrice time window (January 07 2013 through August 23 2016, red symbols), and in the post-Amatrice one (August 24 2016 through August 20 2020, green symbols).

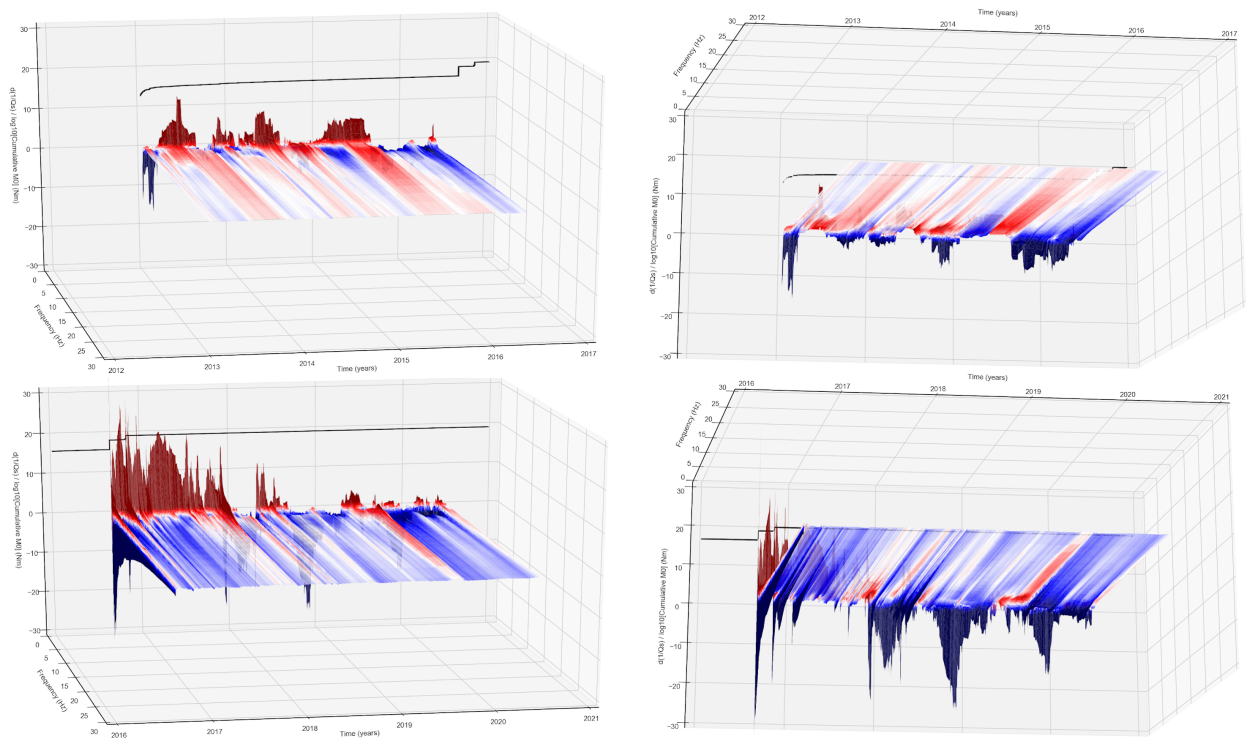

Figure 4. Seismic attenuation as a function of time and frequency, calculated at a hypocentral distance of 40 km. Central Apennines, before and after the Amatrice main shock of August 24, 2016. **Upper:** from two different points of view, anomalies of $Q_S^{-1}(f,t)$ from the average calculated between 01/01/2013 and 23/08/2016 (one day before the Amatrice main shock). **Lower:** from two different points of view, anomalies of $Q_S^{-1}(f,t)$ from the average calculated as described above, in the time window starting at the onset of the Amatrice main shock. After the

first main shock of the Amatrice sequence (M6, 24/08/2016), the seismic parameter in the epicentral region undergoes an instantaneous drop due to the coseismic stress drop-induced negative dilatation. The latter produces a sudden reduction of the crustal bulk permeability via a reduction of crack density and interconnection. The strong ground shaking is responsible for a contrasting action that tends to increase crack density in rocks that are very close to the free surface through damage (Rubinstein and Beroza, 2005; Kelly et al. 2013; Malagnini et al., 2019). Damage produces the positive peaks that affect the attenuation parameter at low-frequency (say, below 2.0 Hz), that occur immediately after the negative anomalies discussed earlier. Damage probably also produces the thin “lines” of increased attenuation parameter that can be seen after each main shock (see Figure 11). Because low-frequency shaking is associated with surface waves, in such a portion of the spectrum, damage is the dominant effect over reduction of crack density and permeability produced by the coseismic stress drop.

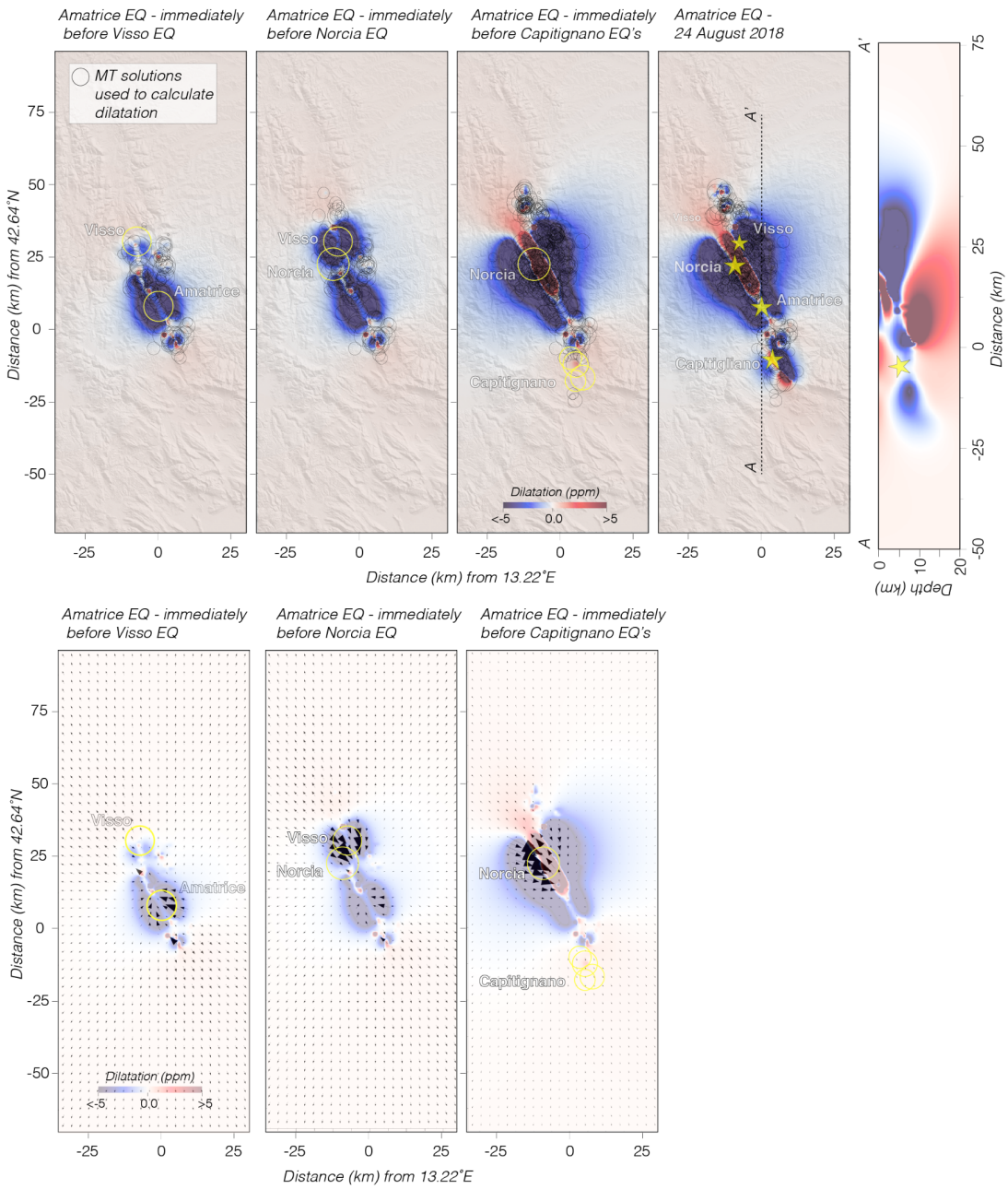

Figure 5. a) Cumulative dilatation. Cumulative dilatation is calculated assuming the SW dipping moment tensor solutions of M≥3 earthquakes were the rupture planes. Dilatation is shown on horizontal planes at 5 km depth, and a cross section is also shown. If drops in $Q_S^{-1}(f,t)$ are related to drops in crack density, negative dilatation (compression) is to be expected, in close agreement with the conceptual model by Muir-Wood and King (1993). **b)** Expected relative flow magnitudes and directions resulting from coseismic dilatation

changes caused by M≥3 earthquakes beginning with the 24 August 2016 Amatrice earthquake to times just before the Visso, Norcia, and Capitignano earthquakes.

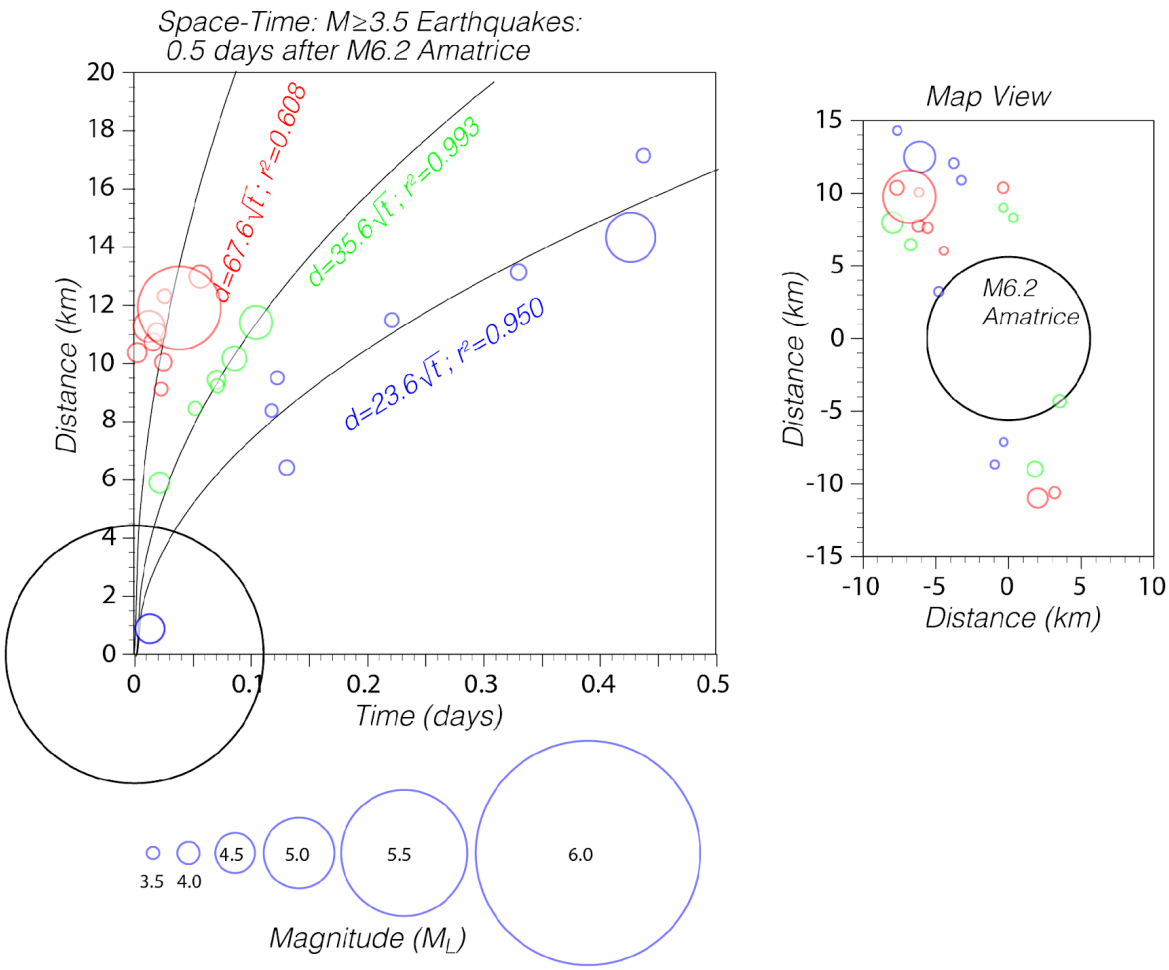
Space-Time: M≥3.5 Earthquakes:
0.5 days after M6.2 Amatrice
d=67.6√t ; r²=0.608
d=35.6√t ; r²=0.993
d=23.6√t ; r²=0.950
Distance (km)
Time (days)
Map View
M6.2
Amatrice
Distance (km)
Distance (km)
3.5
4.0
4.5
5.0
5.5
6.0
Magnitude (M_L)

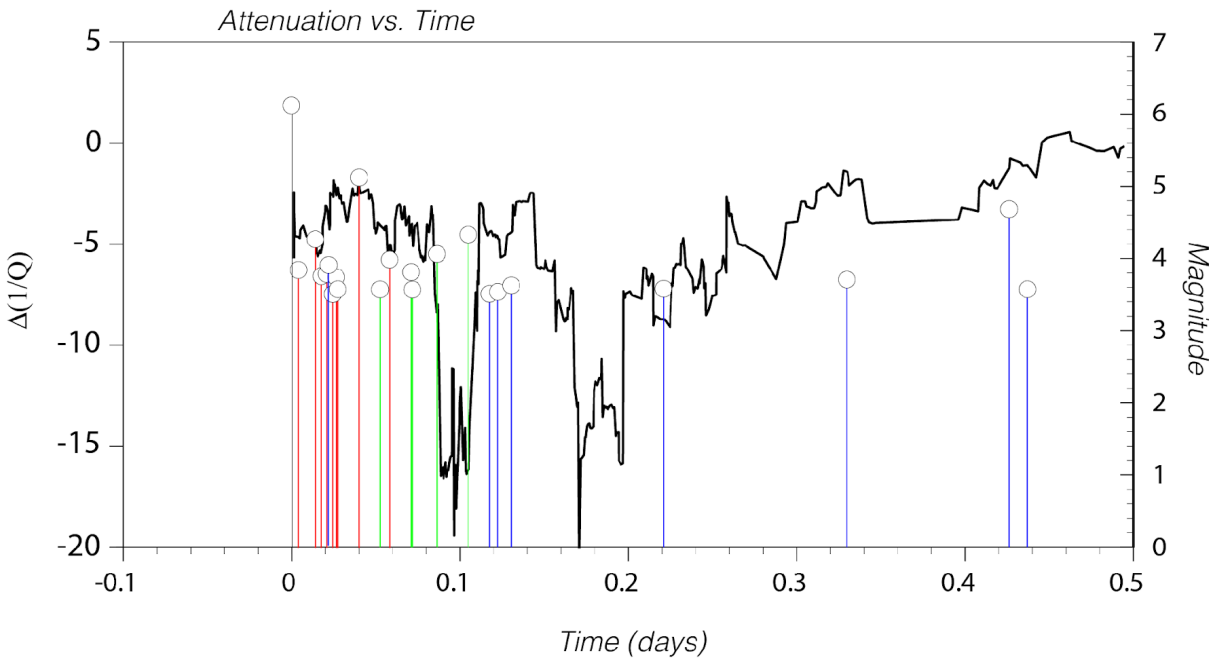
Attenuation vs. Time
Δ(1/Q)
Magnitude
Time (days)

1056

Figure 6. Diffusion and attenuation vs. time: Amatrice. Upper: three different simultaneous diffusion processes may be recognized mostly to the North of the Amatrice main shock. Map view to the right. **Lower:** 2.2 Hz seismic attenuation (black solid line) drops for about six hours after the mainshock, then goes back to higher values (still negative). The drop in attenuation may be associated to the effect of the coseismic stress drop on the crustal cracks (coseismic crack closure is expected in normal-faulting earthquakes, see Muir-Wood and King, 1993) and thus to crustal permeability. Over a broader time window, the effects are clear and may be interpreted in terms of two competing effects: damage of shallow crustal rocks (Rubinstein and Beroza, 2005), and crack closure due to the coseismic stress drop of a normal-faulting earthquake. The colors of the vertical lines associated with earthquakes correspond with the earthquakes portrayed by colored circles in the upper panel.

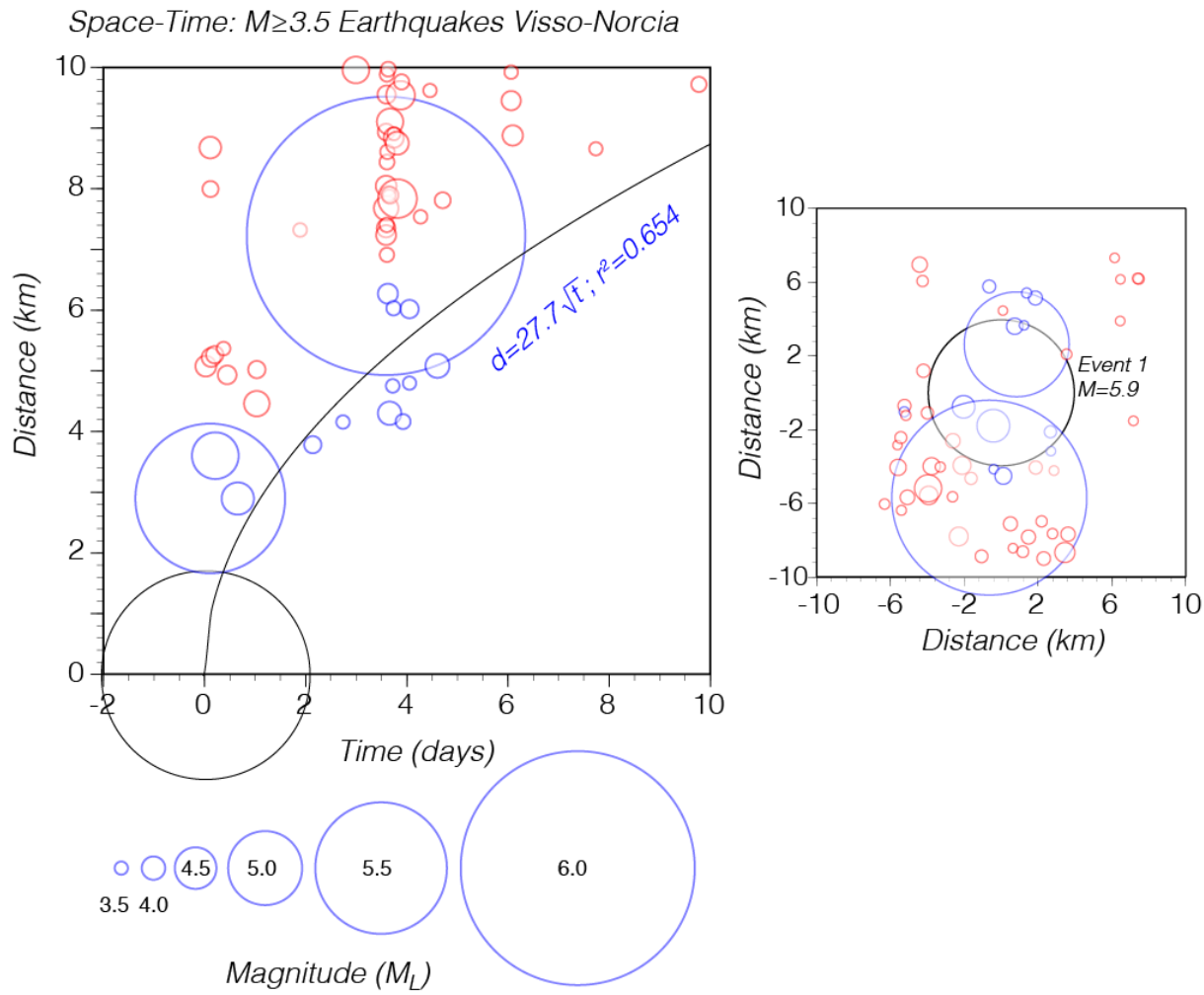
Space-Time: M≥3.5 Earthquakes Visso-Norcia
Distance (km)
Time (days)
d=27.7√t ; r²=0.654
Event 1
M=5.9
Distance (km)
Distance (km)
3.5 4.0
4.5
5.0
5.5
6.0
Magnitude (M_L)

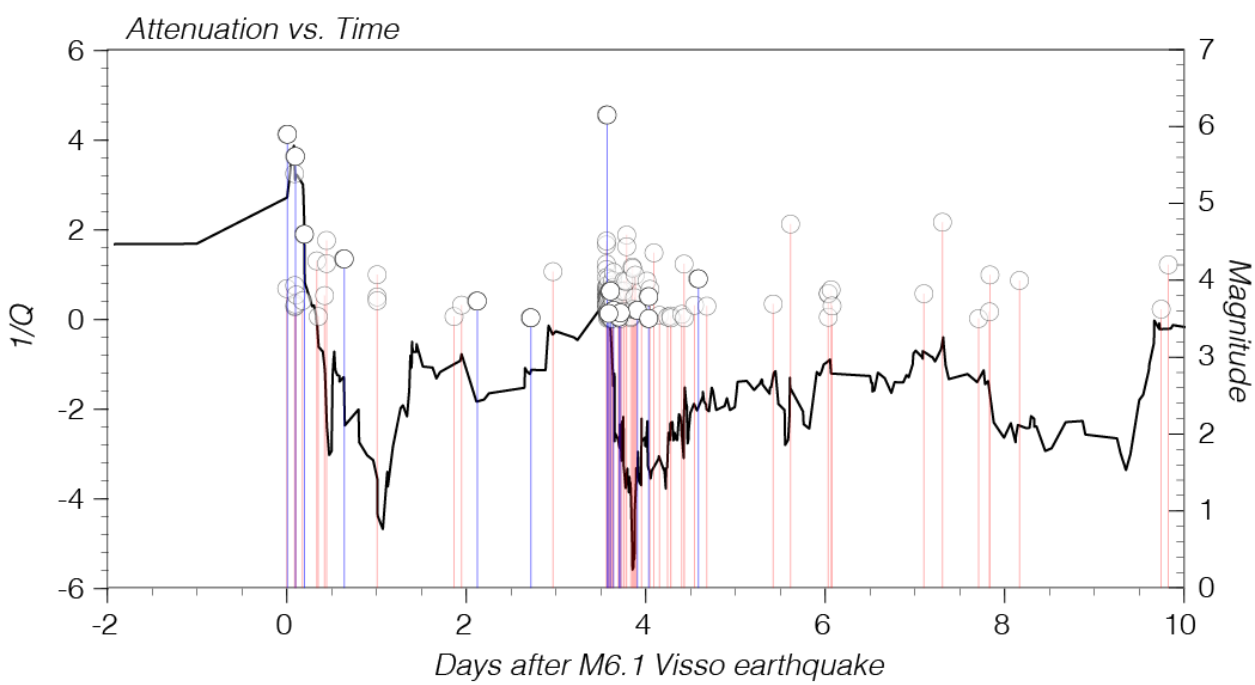
Attenuation vs. Time
1/Q
Magnitude
Days after M6.1 Visso earthquake

Figure 7. Diffusion and attenuation vs. time: Visso-Norcia. Upper: diffusion process associated to the mainshocks of Visso (October 26, 2016) and Norcia (October 30, 2016), with a map view to the right. **Lower:** 2.2 Hz fluctuation of the seismic attenuation parameter around the pre-Amatrice average. The colors of the vertical lines associated with earthquakes correspond with the earthquakes portrayed by colored circles in the upper panel.

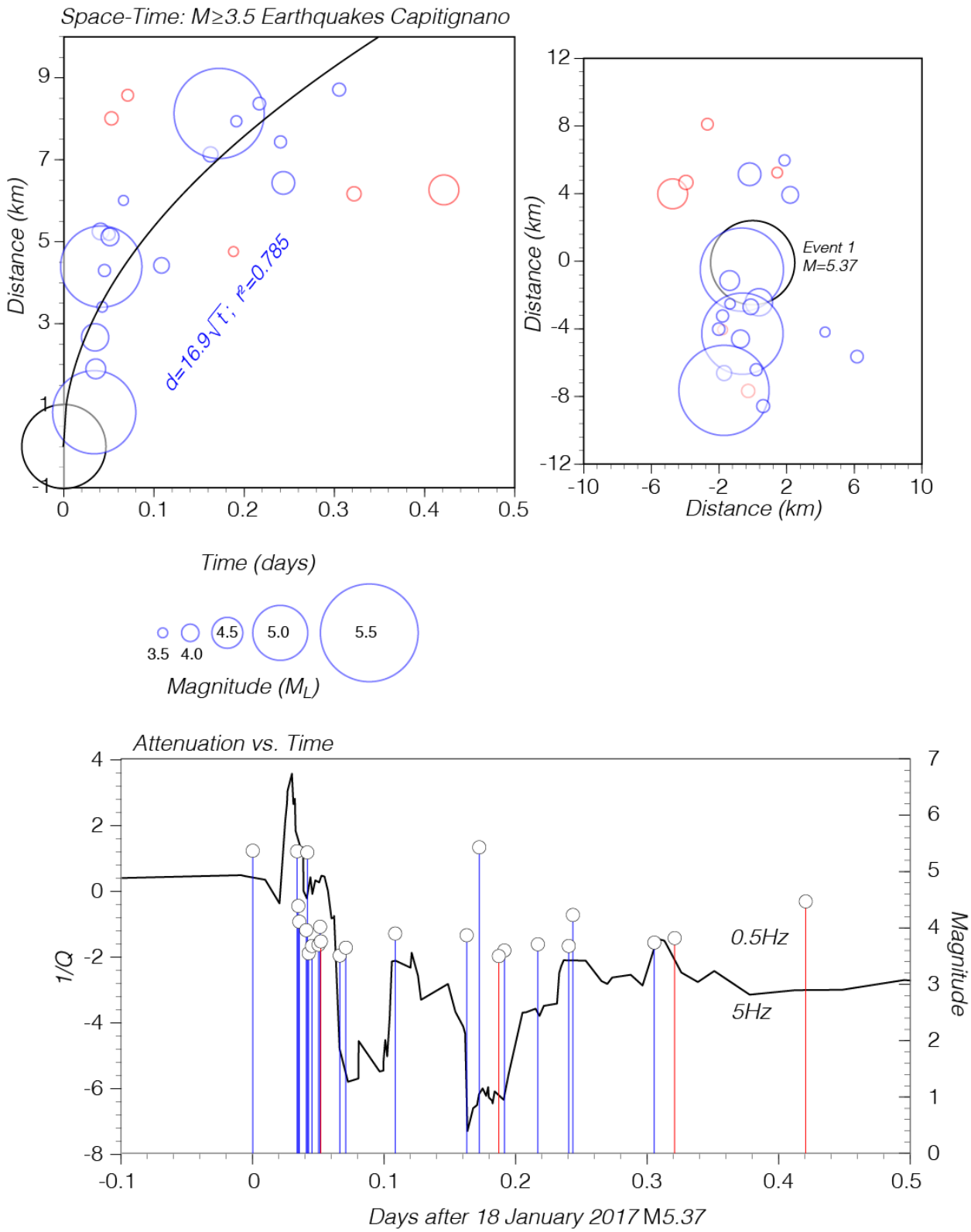

Figure 8. Diffusion and attenuation vs. time: Capitignano. Upper: diffusion process associated to the seismic sequence of Capitignano (January 18, 2017). Map view to the right. **Lower:** 2.2 Hz fluctuation of the seismic attenuation parameter around the pre-Amatrice average. The colors of

the vertical lines associated with earthquakes correspond with the earthquakes portrayed by colored circles in the upper panel.

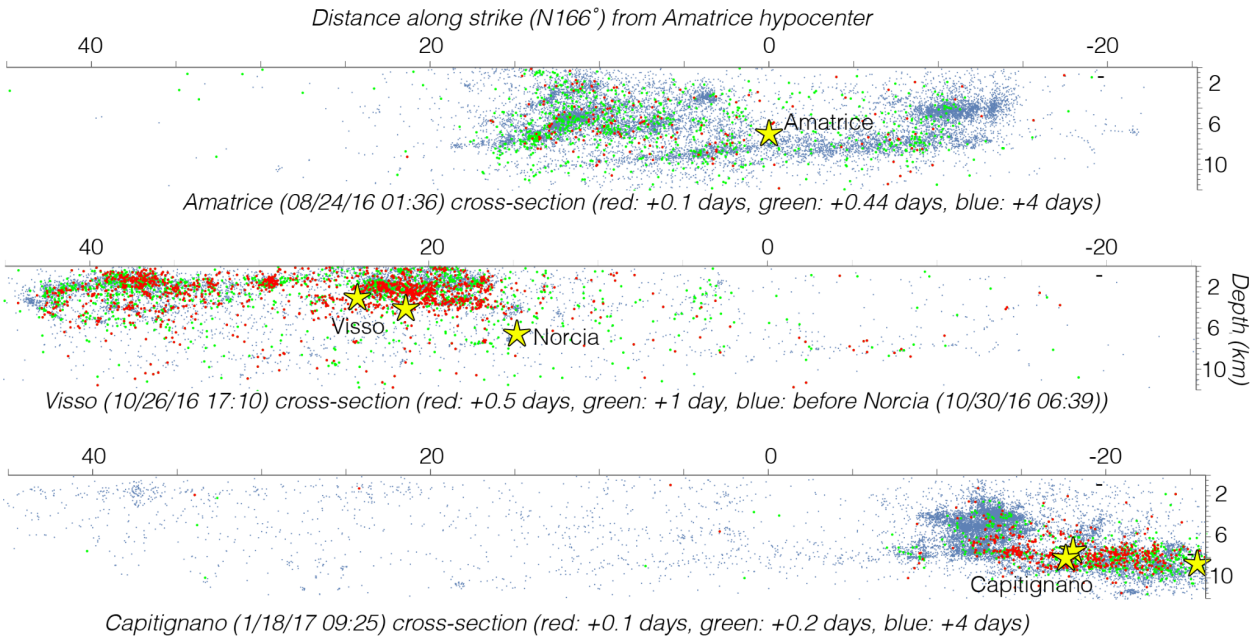

Figure 9. Cross-sectional views of relocated catalogs. Relocated earthquake catalogs of the Central Apennines seismic sequence (Tan et al., 2021). The top panel shows an eastward view that highlights a basal detachment at ~10-15 km depth as well as several structures above it. Red events correspond to the first 0.1 days after the Amatrice mainshock and to the first two diffusion curves in Figure 6, and the green dots include all three diffusion events; these earthquakes highlight potential fluid diffusion pathways along faults. The red events in the center panel correspond in time with the potential diffusion event between the Visso and Norcia shocks (Figure 7). The lower panel shows potential diffusion pathways involving the Capitignano sequence of 4 M≥5 shocks (Figure 8).

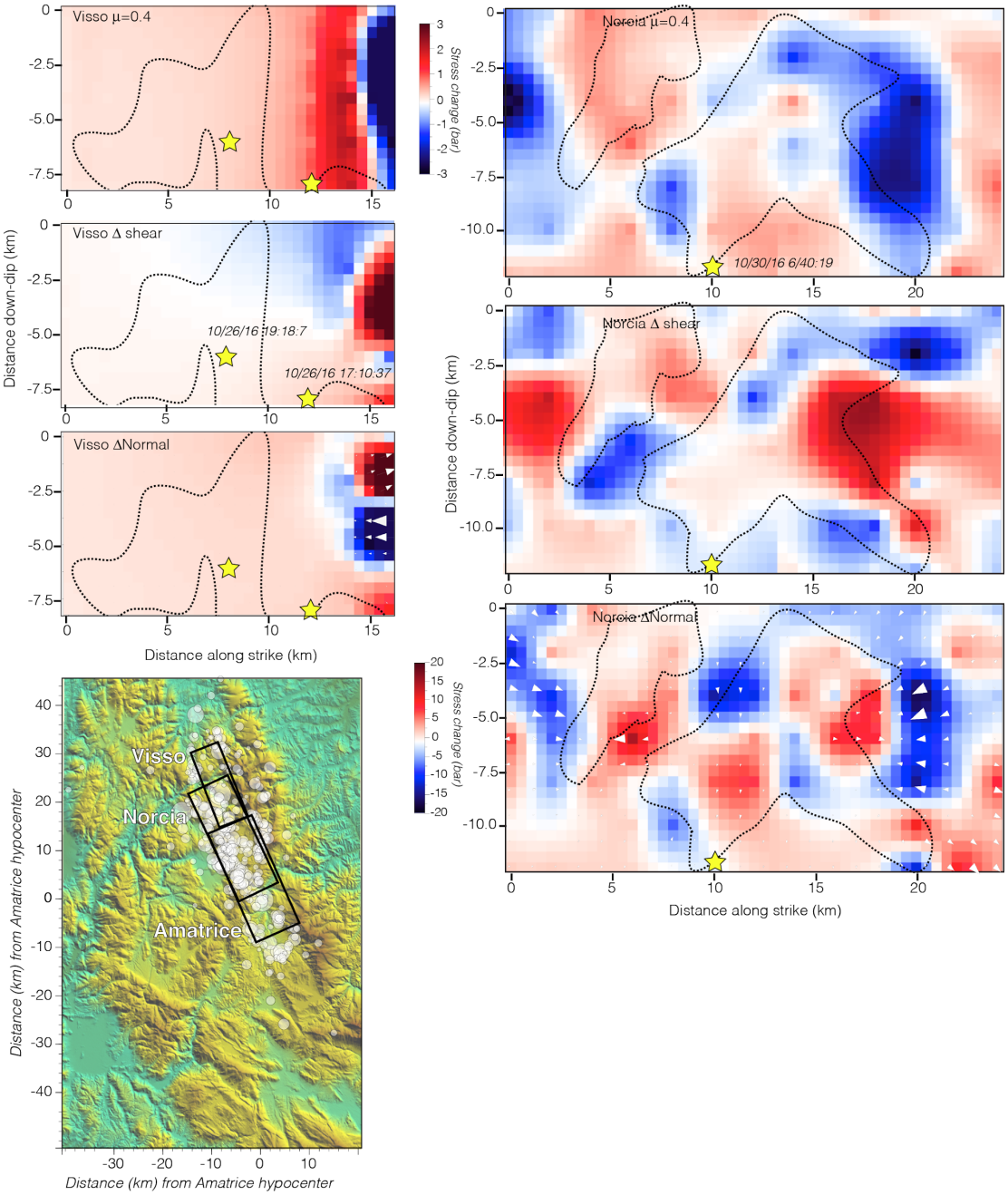

Figure 10. Calculated static stress changes from **M**≥3 earthquakes beginning with the 24 August 2016 Amatrice earthquake resolved on the ruptures of the Visso and Norcia earthquakes (left and right columns, respectively). Hypocenters are shown by yellow stars and approximate slip distributions outlined from solutions by Chiaraluce et al. (2017). Coulomb stress changes are mostly positive on the Visso plane (calculated with an intermediate friction coefficient of 0.4). Shear and normal stress changes are also shown. Expected magnitudes and directions of relative fluid flow resulting from normal stress

changes are superposed on the normal stress change map for both the Visso and Norcia ruptures. The Norcia plane shows very complex patterns of stress change and fluid flow.

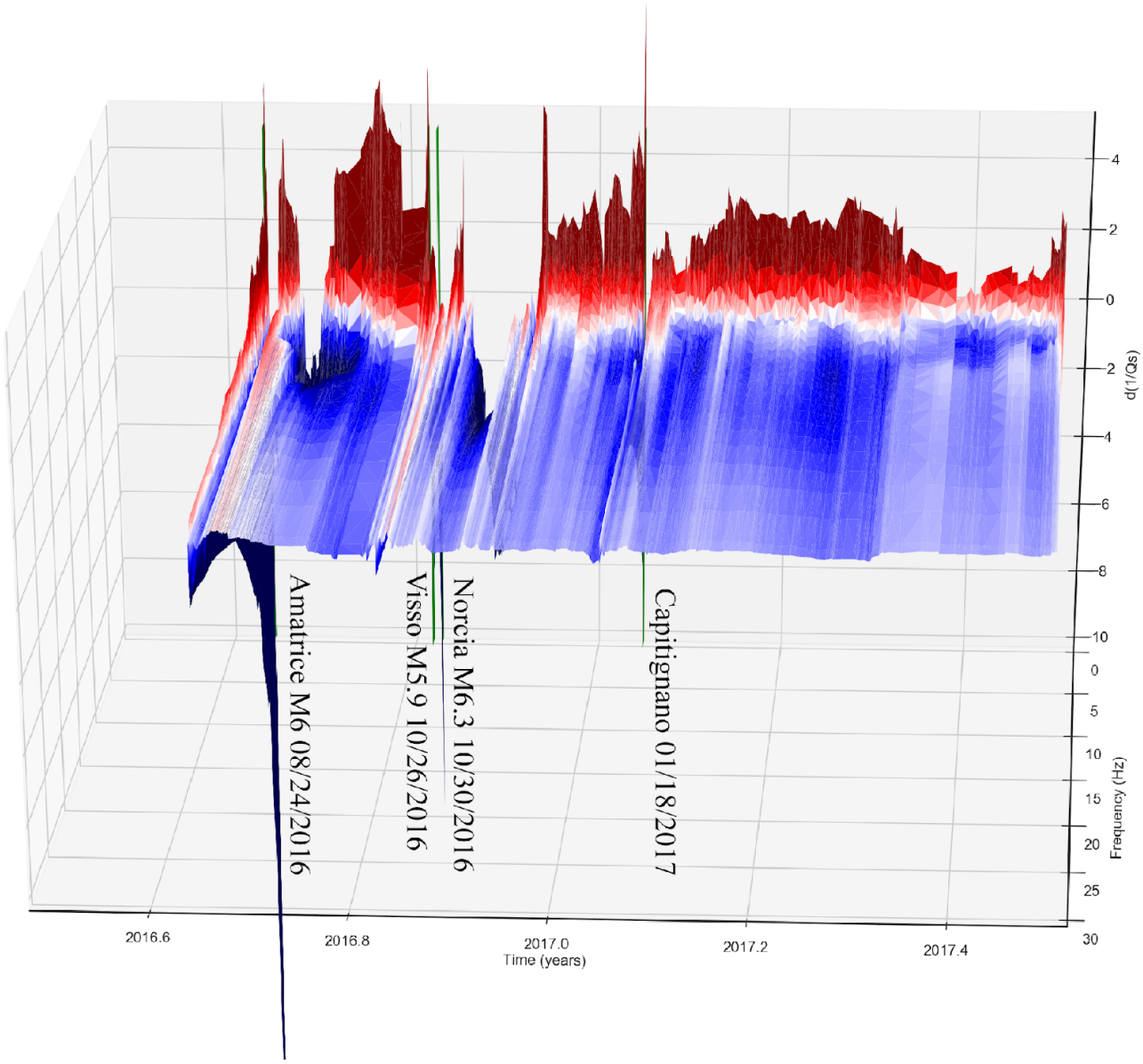

Figure 11. 3D visualization of the seismic attenuation parameter $Q_S^{-1}(f,t)$ during the most energetic part of the Amatrice-Visso-Norcia seismic sequence. Indicated are the occurrences of the three mainshocks and of the Capitignano sub-sequence of January 18 2017. It is very clear that the earthquakes produce a sharp coseismic drop in seismic attenuation at relatively high frequencies (only frequencies $f \geq 1$ Hz are plotted here) due to crack closing (Muir-Wood and King, 1993), followed by a more gentle rise, probably due to fluid displacement through diffusion, and a wide through that is probably due to the cumulative effects of coseismic crack closure produced by the aftershocks. The pattern is reproduced after each main event, and after the Capitignano sub-sequence.

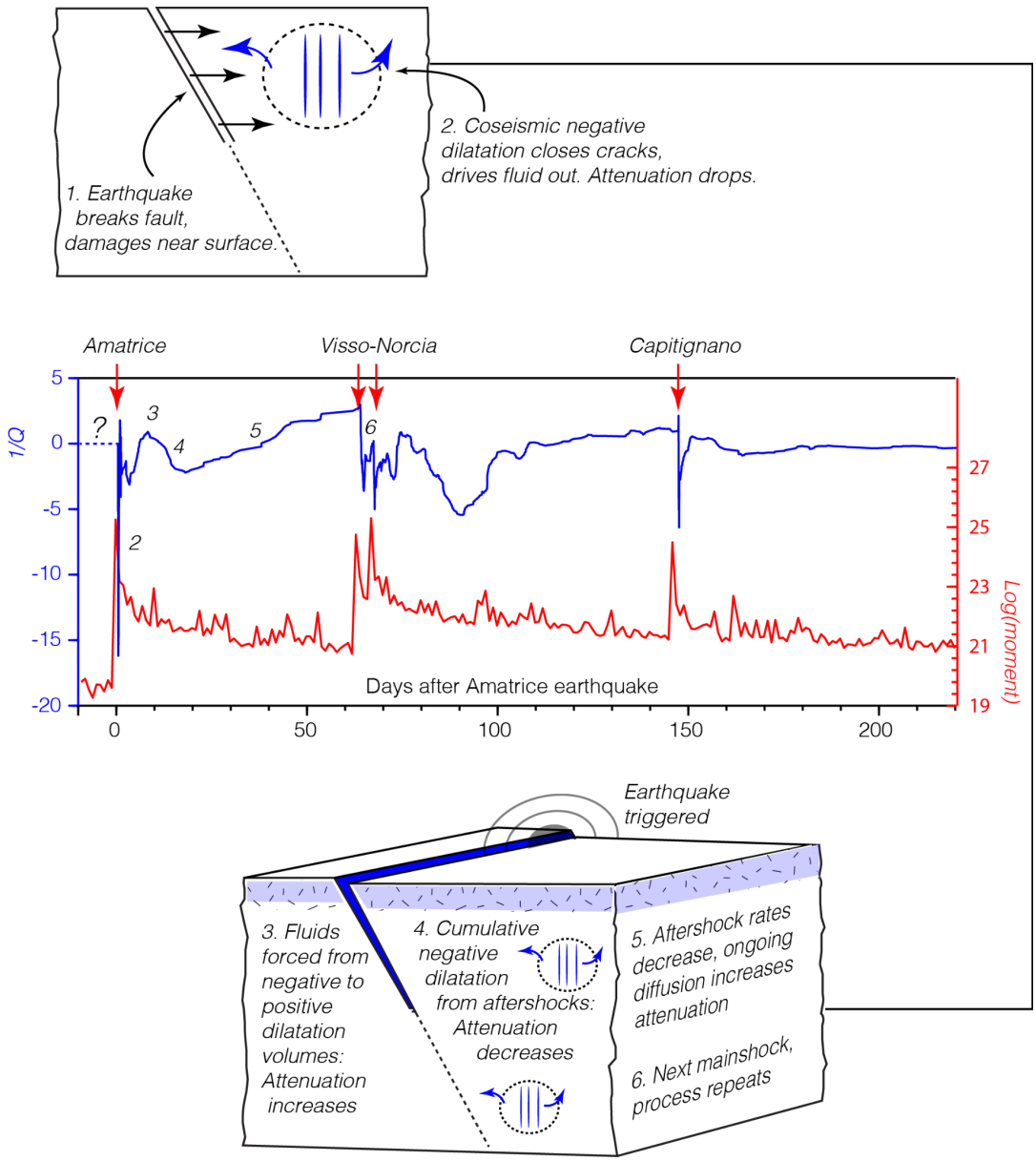

Figure 12. Conceptual model of fluid behavior. Scaling the attenuation vs. time curves from after the Amatrice, Norcia, and Capitignano earthquakes, we note a consistent shape. Each mainshock that initiates a sequence is associated with a sharp increase in $Q_S^{-1}(f,t)$, $f = 2.2\ Hz$, followed by a comparatively steep drop. This happens during periods where potential diffusion is also observed. A subsequent gradual recovery in $Q_S^{-1}(f,t)$, $f = 2.2\ Hz$, persists up until the next mainshock. We hypothesize that this recovery is associated with the redistribution of fluids into newly damaged faults and into the shallow crust. The question mark on the dashed segment of the 1/Q curve indicates that such a horizontal segment is there for a reference purpose only, for we have no information about what happens to the attenuation parameter right before the Amatrice earthquake.

[Journal of Geophysical Research, Solid Earth]

Supporting Information for

Crustal Permeability Changes Inferred From Seismic Attenuation: Impacts on Multi-Mainshock Sequences

Luca Malagnini[1*], Tom Parsons[2], Irene Munafò[1], Simone Mancini[3], Margarita Segou[4], and Eric L. Geist[2]

[1] Istituto Nazionale di Geofisica e Vulcanologia, Sezione di Roma 1, Rome, Italy.

[2] United States Geological Survey, Moffett Field, CA, USA.

[3] Scuola Superiore Meridionale, Università degli Studi di Napoli Federico II, Naples, Italy.

[4] British Geological Survey, Edinburgh, UK

[*] Corresponding author: Luca Malagnini (luca.malagnini@ingv.it)

Contents of this file

Figures S1, S2, S3, S4, S5, S6, and S7. Tables S1, S2, and S3. An introductory text is also provided.

The catalog of the earthquakes used in this study is provided as a separate file.

Introduction

We describe the time variability of the attenuation parameter, $Q_S^{-1}(f,t)$, in the Central Apennines region (Italy), between January 2013 and the end of August 2020. As it is described in details in the main text, $Q_S^{-1}(f,t)$ is obtained by correcting the total attenuation (a sample is plotted in Figure 3a of the main text) for the effect of the geometric attenuation that was quantified by Malagnini et al. (2011, their eq. (3)).

In our study we consider two physical parameters, rock permeability and anelastic attenuation of seismic waves, to be somehow equivalent; our statement is based on the following evidence/interpretation:

1. Increased attenuation has been observed at Parkfield following strong motion (see Kelly et al., 2013; Malagnini et al., 2019; Malagnini and Parsons, 2020).
2. Increased $Q_S^{-1}(f,t)$ has been observed after weak shaking from large distant earthquakes (see Malagnini et al., 2019, and Malagnini and Parsons, 2020). Moreover, permeability variations induced by weak shaking in natural environments are described by Brodsky et al. (2003), Manga et al. (2012), Manga and Brodsky (2006), and Parsons et al. (2017). The same phenomenon is also observed in laboratory experiments (Liu and Manga, 2009). We interpret weak-motion shaking-induced increases in $Q_S^{-1}(f,t)$ in terms of increased permeability, due to the removal of colloidal deposits by cyclic flow-induced shear stresses acting on the internal surfaces of cracks.
3. Decreased $Q_S^{-1}(f,t)$ has sometimes been observed after weak shaking, generally from teleseismic earthquakes (Malagnini et al., 2019). We interpret the decreased attenuation in terms of a reduction of permeability due to re-deposition of mobilized colloidal particles in adjacent rock volumes bounded by impermeable surfaces (i.e., a fault zone, see *in situ* results from Malagnini and Parsons (2020) and laboratory results by Liu and Manga (2009));
4. Cyclic variations of $Q_S^{-1}(f,t)$ have been observed at seasonal as well as at multiple tidal periods, plausibly due to pressure-induced variations in crack density (Malagnini et al., 2019). In order to link the observed time variations of $Q_S^{-1}(f,t)$ to rock permeability, we can use a result obtained by Silverii et al. (2018), who noticed that the vertical and the horizontal deformations in the

Apennines are out of phase: whereas the first represents the (instantaneous) elastic response to the load/unload seasonal cycle (maximum load is obtained in summer, minimum load in winter), the second is the result of the increased pore pressure at depth, which is delayed by the time needed for fluids to percolate through the crust in the aquifers (maximum pore-fluid pressure at depth is reached in summer), and to be discharged (minimum pore-fluid pressure at depth is reached in winter).

If hydrostatic pressure at depth in the Apennines peaks in summer, it corresponds to the opening of vertical crustal cracks. In turn, the latter corresponds to increased permeability and fluid mobility. On the contrary, permeability decreases correspond to decreases of hydrostatic pore-fluid pressure, and to closing of vertical crustal cracks that occur in winter (Silverii et al., 2018). The correspondence of higher attenuation in summer and lower attenuation in winter can be seen in Figures 4 and S2. Similar seasonal fluctuations were observed along the San Andreas fault at Parkfield by Malagnini et al. (2019).

5. Progressive increase of $Q_S^{-1}(f,t)$ has been observed before the **M**6 2004 Parkfield main shock on the Pacific side of the SAF (in extension); opposite, progressive decrease of $Q_S^{-1}(f,t)$ has been observed, before the Parkfield main shock, on the North American side of the SAF (in compression, Malagnini et al.,2019).
6. Malagnini et al. (2019) demonstrated that variations of $Q_S^{-1}(f,t)$ on the SAF are inversely correlated to variations of normal stress on the fault. In fact, an instantaneous increase of $Q_S^{-1}(f,t)$ was observed on the Pacific side of the SAF at the time of the **M**6.5 San Simeon event, due to increased Coulomb stress on the SAF at Parkfield. An opposite, instantaneous decrease of $Q_S^{-1}(f,t)$ was observed on the North American side of the SAF. Johanson and Bürgmann (2010) quantified the unclamping induced by the San Simeon earthquake on the SAF, which caused the anomalies in the attenuation parameter.

Physical mechanism of crustal anelastic attenuation:

O'Connell and Budiansky (1977) developed a theoretical model that linked together some physical parameters:

1) (bulk) crack density;
2) fluid saturation;
3) fluid viscosity (that is, relaxation times in viscous behavior);
4) fluid compressibility;
5) (bulk) rock porosity;
6) pore (rock) compressibility.

The theoretical model describes two mechanisms of elastic energy dissipation:

1) viscous relaxation of fluids within the same crack;
2) viscous relaxation through fluid flow between cracks.

Three regimes are allowed:

1) saturated isolated;
2) saturated drained;
3) glued.

Bulk rock permeability plays a fundamental role in the model. Specifically, the higher the permeability, the higher the fluid mobility, and thus the fraction of the elastic energy that can be dissipated via the two mechanisms listed above. Depending on the frequency of oscillation, either one of the three regimes listed above is allowed. At transitional frequencies that separate two adjacent regimes, peaks in $Q^{-1}(f)$ are expected.

Further contents include:

1. A rough display of the spatio-temporal evolution of the seismic sequence (Figure S1), in which we provide information useful for judging the performance of the approach used for the computation of seismic attenuation. In fact, Figure S1 describes the spatial distributions of earthquakes in three different time windows of special importance for this paper: pre-Amatrice, post-Amatrice through pre-Visso, and post-Visso;
2. A zoom on the most energetic part of the seismic sequence, between the Amatrice mainshock (24/08/2016) and 31/12/2016 (Figure S2);
3. An error plot (Figure S3);
4. A trade-off analysis (Figure S4);
5. A plot of the attenuation parameter computed using the total attenuation at a hypocentral distance of 80 km (Figure S5), which allows a direct comparison with the results of Figure 4 of the main text, where the hypocentral distance used was 40 km;
6. A robustness analysis (Figure S6);
7. Evidence of an interesting negative correlation between seismic attenuation and the instantaneous release of seismic moment (Figure S7).

Here are the detailed contents:

1. Spatio-temporal distribution of the seismicity

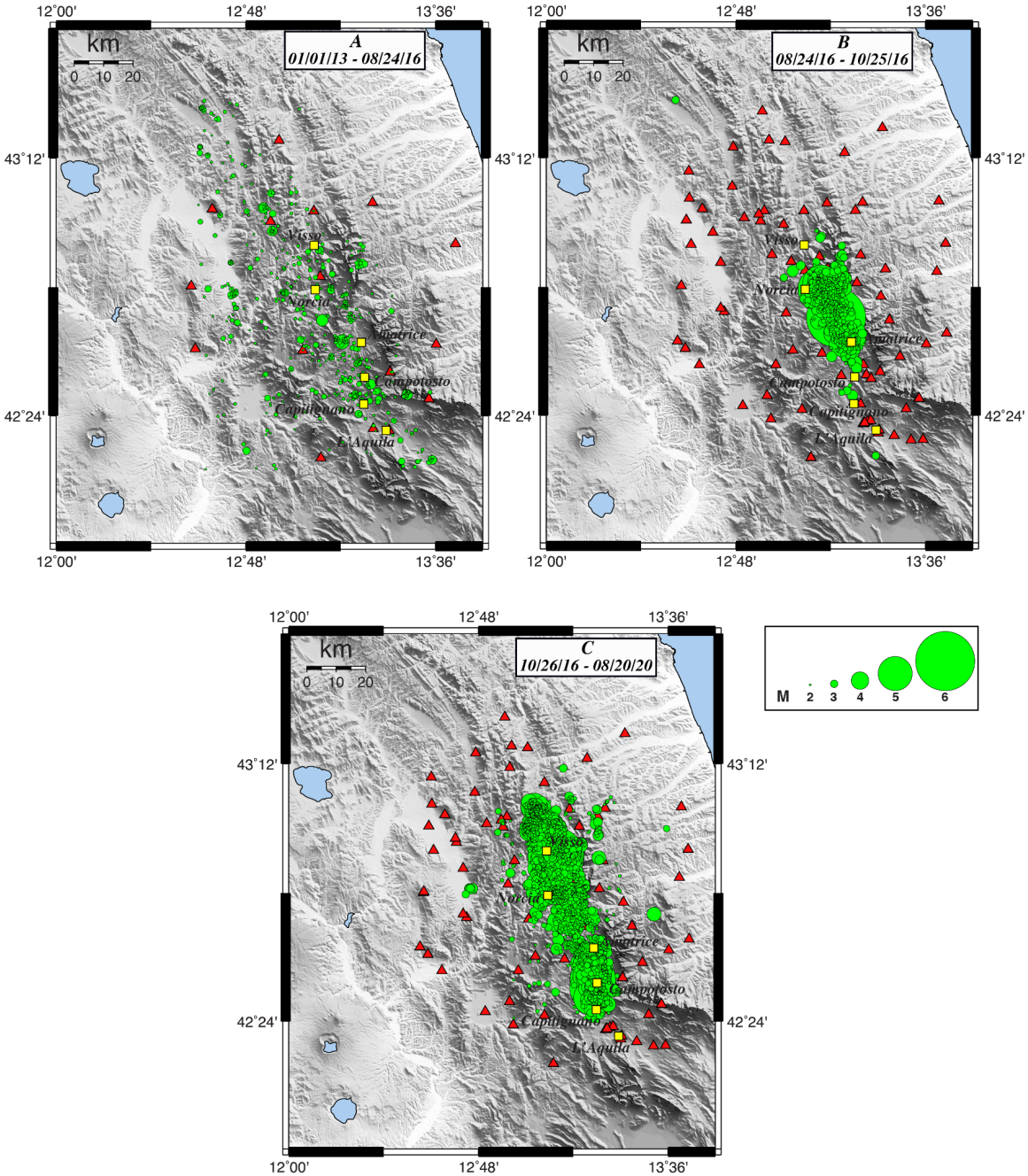

Figure S1. The locations of the events used for the computation of $Q_S^{-1}(t,f)$ in the Central Apennines during the 2016-2017 seismic sequence of Amatrice-Visso-Norcia, in three different time windows: **a)** 01/01/2013 - 23/08/2016; **b)** 24/08/2016 - 25/10/2016; **c)** 26/10/2016 - 20/08/2020.

2. Zooming in the most energetic part of the sequence

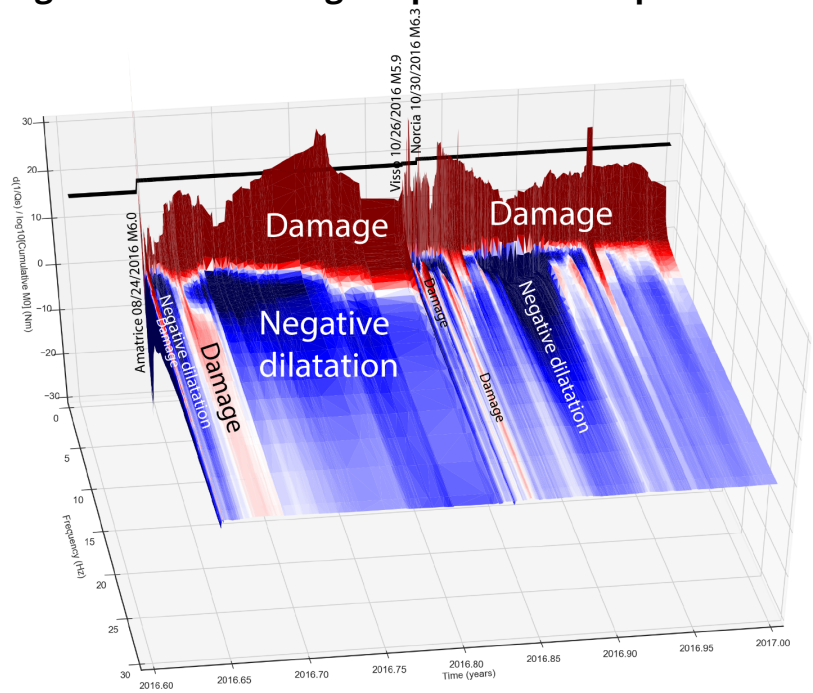

Figure S2. Zoom in the $Q_S^{-1}(t,f)$ 3-D surface, between 24/08/2016 and 31/12/2016.

3. Error plot

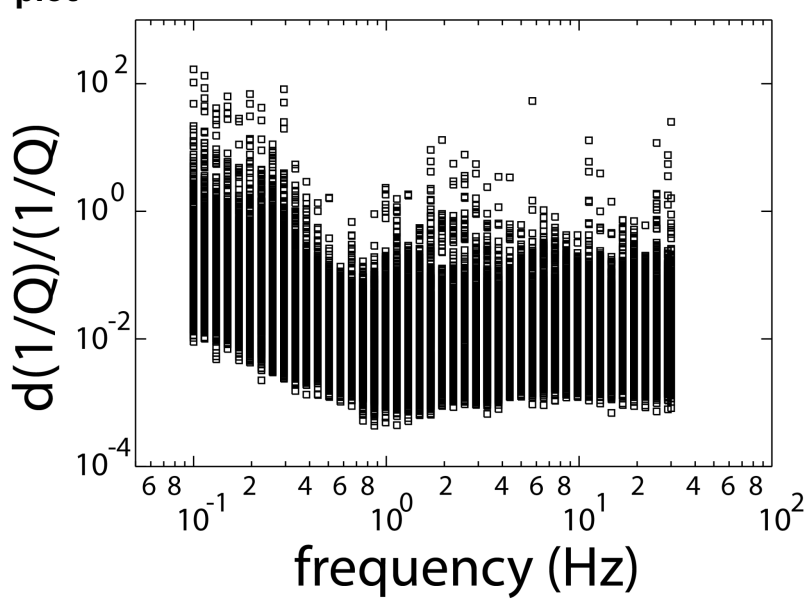

Figure S3. Errors with respect to the average (d(log(1/Q)) calculated in the regressions all time windows and for all frequencies.

4. Trade-offs analysis

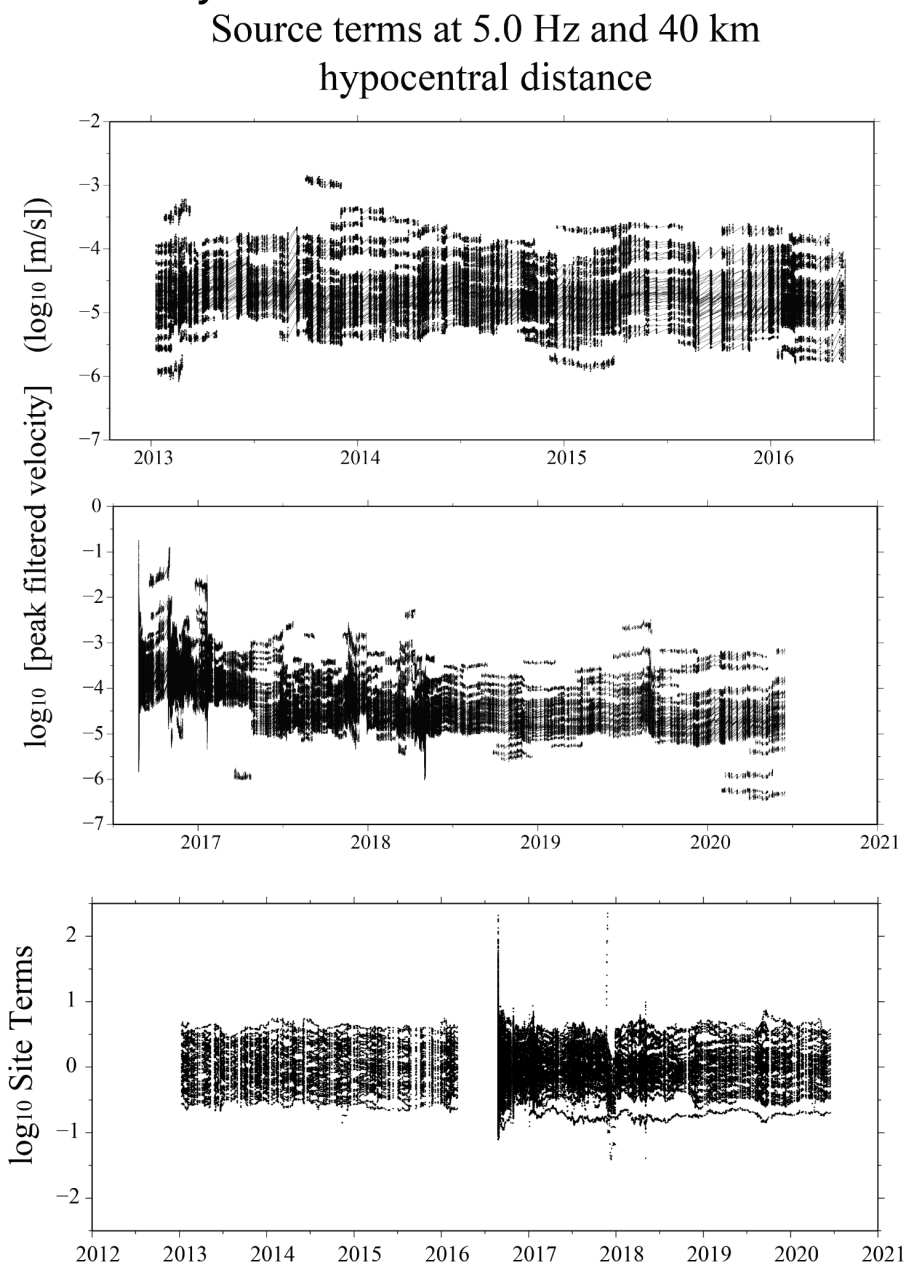

Figure S4. Individual source and site terms plotted as a function of time, during the entire time window analyzed in this paper, at the central frequency of 5 Hz. Upper and middle plots: individual source terms (individual sets of points linked together by a line), for the pre- and post-Amatrice time windows, respectively. Note the sharp decrease in the source amplitudes starting in late spring 2017, due to the fact the most energetic part of the seismic sequence was over, and smaller magnitudes were needed in order to have a decent time resolution. Bottom plot: similarly to the upper and the middle plots, but the site terms are shown in a single frame for the entire time window under investigation.

5. Seismic attenuation at 80 km hypocentral distance

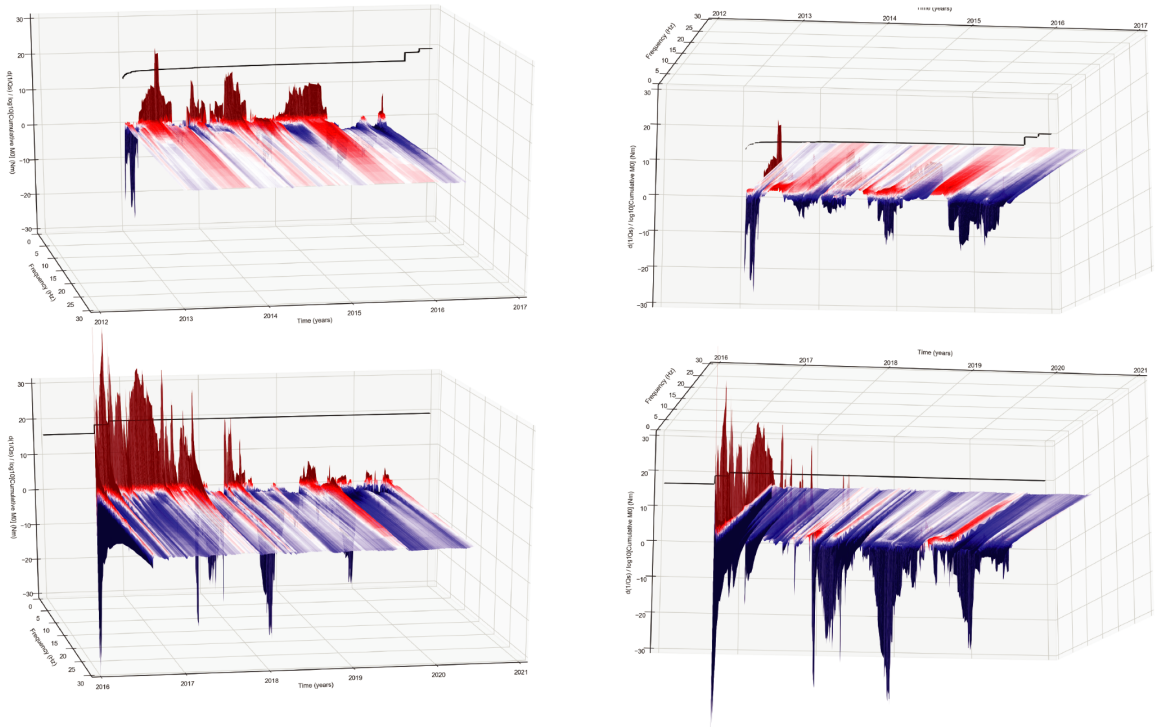

Figure S5. Attenuation parameter calculated using the total attenuation term at a hypocentral distance of 80 km. No differences can be appreciated with the 40 km computation shown in Figure 4 of the main text.

6. Robustness analysis

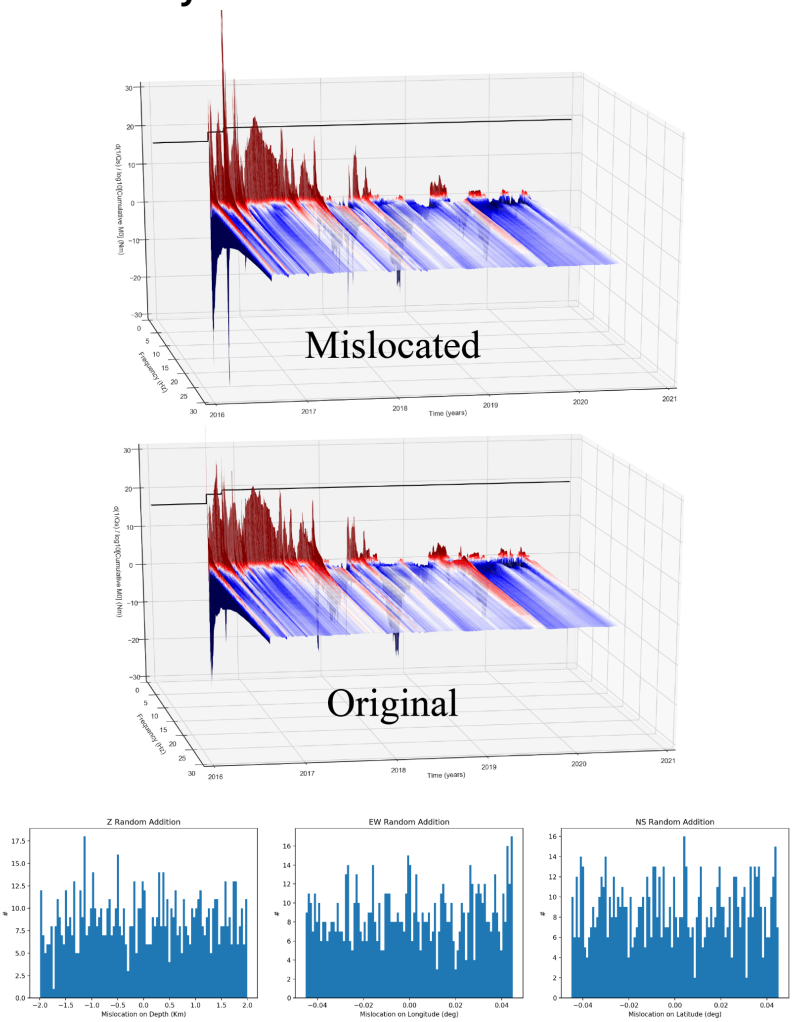

Figure S6. Robustness analysis applied to the results obtained for the time window 01/01/2013 - 30/06/2017, about the temporal variations of the anelastic attenuation parameter $[Q_s(t,f)]^{-1}$ (Figure 4 of the main text). We do it by perturbing the hypocentral localizations with random offsets distributed with constant probability within ±5 km in latitude and longitude and ±2 km in depth, as indicated in this Figure. Regression results, shown here, demonstrate the extreme robustness of the Malagnini and Parsons's method (2020), when applied to the 2016-2017 Central Apennines' seismic sequence. We note that the salient features of the parameter $[Q_S(t, f)]^{-1}$ are present in both plots, although the procedure of artificial degradation of the hypocentral locations reduced some of the character of the 3D surface topography. **Top:** results of the same set of regressions calculated on the mislocated data set; **Middle** results obtained on the original one data set. No appreciable differences can be seen between the two plots; **Bottom:** Distributions of the random offsets that were applied to mislocate the events.

7. Inverse correlation

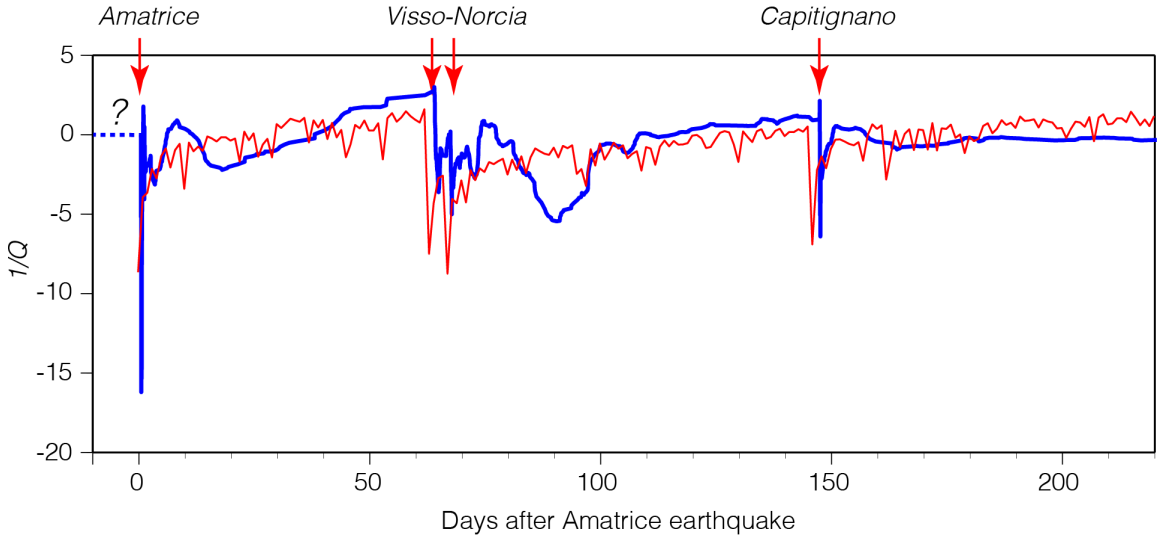

Figure S7. $Q_S^{-1}(t, f = 2\,Hz)$ (blue) is negatively correlated with the instantaneous moment release during the seismic sequence (in red, the function shown in Figure 11 of the main text, multiplied by -1). From this comparison it is very clear that the broad throughs in the blue line do not have counterparts in the instantaneous moment release. The question mark on the dashed segment of the 1/Q curve indicates the lack of information about what happens to the attenuation parameter right before the Amatrice earthquake.

8. Tables

Table S1. Stations used in this study:

Station name	Latitude	Longitude	Altitude (m)
ACC	42.696	13.242	922
ACT	42.7713	13.4125	45
AMT	42.6325	13.2866	933
ANT	42.4182	13.0786	564
AQA	42.3755	13.3393	693
AQF	42.3807	13.3547	805
AQG	42.3737	13.337	743
AQK	42.345	13.4009	726
AQP	42.3837	13.3686	1192
AQU	42.354	13.405	710
AQV	42.3771	13.3439	692
ASP	42.848	13.6479	89
ASS	43.075	12.6041	390
ASSB	43.0426	12.6587	734
BRS	42.3243	13.5902	977
BVG	42.9323	12.611	216

BZZ	42.337	13.4685	640
CAMP	42.5358	13.409	1283
CESI	43.0049	12.9046	840
CESX	42.6085	12.5868	458
CIT	42.5942	13.1632	873
CLF	43.0367	12.9204	701
CLO	42.8294	13.206	1456
CMI	42.8504	13.0928	767
CNE	42.8944	13.1528	798
CNO	43.1421	13.0792	615
CPT	42.8274	12.9251	609
CSA	43.008	12.5906	196
CSC	42.719	13.0122	683
CTD	42.3884	12.9477	484
FBR	43.3436	12.9119	31.5
FCC	42.7545	13.1932	1553
FDMO	43.0365	13.0873	550
FIAM	42.268	13.1172	1070
FMG	42.268	13.1172	1073
FMT	43.188	12.9332	497
FOC	43.0263	12.8965	821
FOCC	42.9574	12.7079	283
FOPC	42.9697	12.7031	300
FOS	43.0146	12.8351	965
GIGS	42.4532	13.5728	960
GLT	43.2331	12.789	607
GNU	42.8038	12.5702	1085
GSA	42.4207	13.5194	1063
GUMA	43.0627	13.3352	574
LNSS	42.6029	13.0403	1155
LSS	42.5582	12.9689	1067
MCT	43.2925	13.4189	349
MCV	42.9934	13.0013	709
MMO	42.8993	13.3268	1030
MNF	43.0596	13.1844	644
MOMA	42.801	12.5682	1040
MOMA	42.8039	12.5701	1040
MSC	42.5268	13.3508	1335
MSCT	42.5267	13.3509	1382
MTL	43.2494	13.0083	376
MTR	42.524	13.2448	974
NCR	43.1115	12.7845	492
NOR	42.7924	13.0924	661
NRC	42.7925	13.0964	616
NRCA	42.8335	13.1143	927
OFFI	42.935	13.6857	320
PBN	43.0637	13.0821	503
PCB	42.558	13.338	1315
PGG	42.3229	13.5394	769
PRE	42.8793	13.0334	622

PTI	43.0665	13.657	294
PZI1	42.4356	13.3262	908
RQT	42.813	13.311	1188
RTI	42.4302	12.829	393
SLO	42.9002	12.9528	876
SNI	42.632	12.554	380
SNO	43.0371	13.3041	528
SNTG	43.255	12.9406	650
SPD	42.5151	13.371	1338
SPM	42.7232	12.7512	778
SPO1	42.7344	12.7363	428
T0104	42.3599	13.3382	754
T1241	42.8563	13.4312	664
T1242	42.8293	13.2044	1451
T1243	42.6966	13.4484	1120
T1245	42.8565	13.188	1541
T1246	42.5833	13.493	1134
T1247	42.4416	13.2983	836
T1256	43.0063	13.226	1536
TER	42.6565	13.6895	317
TERO	42.6228	13.6039	673
TLN	43.2159	13.2584	412
TRE	42.8765	12.7358	261
TRL	42.4613	12.9323	1226
TRN1	42.5582	12.6461	175
UST	42.9419	13.125	733
VAL	43.1593	12.6017	348

Table S2. Moment tensor solution parameters for the earthquakes used in this study to compute cumulative stress changes.

Origin Time	Latitude	Longitude	Depth	**M**	Azimuth	Dip	Rake	Fit
2016.647724	42.71	13.22	5	5.97	155	50	-85	0.718
2016.647761	42.61	13.28	5	4.46	115	57	-123	0.6013
2016.647832	42.79	13.15	5	5.29	136	46	-100	0.6889
2016.647882	42.8	13.14	5	3.93	331	57	-103	0.5912
2016.647898	42.61	13.27	7	3.7	332	61	-84	0.4871
2016.647959	42.62	13.24	6	4.12	330	60	-90	0.6554
2016.648009	42.77	13.12	3	4.32	340	50	-90	0.5354
2016.648889	42.82	13.15	7	4.5	335	65	-75	0.5542
2016.649139	42.8	13.25	3	3.77	220	65	-40	0.6158
2016.649564	42.66	13.22	7	4.19	339	55	-93	0.542
2016.649859	42.78	13.15	5	3.31	317	63	-121	0.6416
2016.650018	42.8	13.17	6	3.04	348	50	-94	0.5681
2016.650201	42.65	13.21	9	3.98	327	56	-100	0.5551
2016.650648	42.75	13.21	5	4.36	339	72	-99	0.5832
2016.650752	42.69	13.23	7	3.27	337	50	-113	0.3077
2016.650827	42.62	13.33	2	3.75	138	61	-98	0.4632
2016.651297	42.61	13.3	3	3.08	320	55	-90	0.5281
2016.651681	42.61	13.25	7	3.17	324	65	-95	0.5033

2016.651708	42.6	13.29	5	4.39	125	55	-120	0.5833
2016.652514	42.59	13.29	5	3.45	122	54	-127	0.5789
2016.653013	42.67	13.29	3	3.61	155	55	-90	0.5475
2016.653476	42.7	13.23	7	3.17	180	55	-55	0.6126
2016.653501	42.62	13.29	5	3.13	138	48	-109	0.5618
2016.653515	42.6	13.29	5	4.72	127	50	-113	0.606
2016.653592	42.62	13.3	5	3.23	339	55	-93	0.5886
2016.653607	42.75	13.21	7	3.21	120	70	90	0.6211
2016.653637	42.77	13.15	5	3.36	347	71	-107	0.5564
2016.653672	42.57	13.29	7	2.87	335	55	-80	0.4884
2016.654271	42.61	13.3	5	2.83	128	51	-124	0.4744
2016.654744	42.6	13.29	5	2.97	330	60	-75	0.613
2016.654837	42.69	13.15	7	3.49	323	61	-96	0.7015
2016.655376	42.79	13.15	5	3.07	355	65	-70	0.6052
2016.65565	42.84	13.26	2	3.13	170	55	-60	0.5379
2016.655902	42.84	13.24	2	3.75	175	50	-65	0.5935
2016.656062	42.84	13.25	2	3.91	175	55	-60	0.5068
2016.656081	42.84	13.25	3	2.9	165	65	-55	0.4873
2016.656437	42.84	13.24	2	3.46	175	65	-60	0.5272
2016.65646	42.55	13.31	3	3.28	330	50	-70	0.5776
2016.656618	42.77	13.23	4	2.72	165	85	50	0.583
2016.656841	42.79	13.18	5	3.06	121	52	-102	0.5318
2016.656952	42.84	13.25	2	3.53	175	65	-60	0.5203
2016.658189	42.59	13.26	7	3.4	130	53	-106	0.6249
2016.659071	42.6	13.31	5	3.14	144	47	-105	0.6194
2016.659224	42.72	13.21	7	3.31	329	54	-110	0.6808
2016.65938	42.8	13.23	5	3.17	124	66	-97	0.533
2016.659529	42.63	13.29	5	3.24	140	55	-85	0.6666
2016.659657	42.78	13.11	10	2.93	283	57	-130	0.5339
2016.659964	42.59	13.29	5	3.57	159	71	-95	0.6266
2016.660249	42.77	13.12	9	3.48	155	50	-95	0.662
2016.660283	42.82	13.24	5	4.15	206	60	-87	0.5723
2016.660371	42.82	13.14	5	3.78	340	55	-85	0.6029
2016.66079	42.74	13.2	5	3.08	324	47	-105	0.5382
2016.6614	42.76	13.2	7	3.42	345	50	-70	0.5562
2016.661924	42.75	13.19	6	3.57	131	46	-100	0.4675
2016.662738	42.73	13.14	4	2.81	312	75	138	0.445
2016.663107	42.83	13.15	6	2.85	119	77	128	0.6487
2016.663237	42.86	13.22	4	3.15	5	80	20	0.5859
2016.664003	42.8	13.14	6	3.33	340	55	-65	0.5463
2016.665539	42.73	13.19	8	2.87	353	73	-100	0.5854
2016.66646	42.82	13.26	3	2.96	338	61	-132	0.6414
2016.66686	42.81	13.16	7	3.08	50	89	-105	0.6584
2016.667779	42.76	13.18	6	3.18	132	56	-100	0.5255
2016.667968	42.84	13.14	5	3.95	340	60	-85	0.626
2016.668019	42.87	13.24	4	3.42	277	81	160	0.6667
2016.66819	42.76	13.24	8	3.31	165	75	-55	0.6962
2016.66874	42.83	13.26	5	3.52	321	79	-134	0.5765
2016.668959	42.83	13.13	5	3.38	345	60	-80	0.7125
2016.669139	42.78	13.16	5	3.42	344	65	-92	0.6202
2016.669198	42.75	13.24	5	3.44	310	45	-90	0.6394
2016.669619	42.85	13.18	11	2.9	297	61	-118	0.461
2016.669841	42.62	13.31	5	3.62	145	60	-80	0.5498
2016.670176	42.86	13.23	5	3.11	135	50	-90	0.4693
2016.6705	42.81	13.24	3	3.03	315	70	-142	0.5683
2016.670656	42.81	13.17	7	3.12	220	80	15	0.4686
2016.670719	42.56	13.3	6	3.34	301	69	-112	0.7037
2016.673883	42.75	13.14	2	2.79	15	50	-65	0.4863
2016.67407	44.5	9.6	3	3.08	257	76	-111	0.7026
2016.675042	42.77	13.13	2	4.16	338	61	-98	0.5323
2016.675241	42.81	13.2	3	2.87	158	74	-102	0.4533

2016.675919	42.93	13.26	4	2.91	170	80	-65	0.4087
2016.676038	42.87	13.21	4	4.29	284	85	170	0.579
2016.676621	42.87	13.22	4	3.09	10	70	25	0.5971
2016.676746	42.86	13.22	2	2.98	115	67	-136	0.5672
2016.677055	43.98	7.52	9	3.31	292	81	160	0.4772
2016.678225	42.85	13.23	2	2.79	312	63	-121	0.5355
2016.680826	42.85	13.21	4	3.34	287	81	160	0.5707
2016.682015	42.63	13.31	7	2.83	339	65	-95	0.4605
2016.682604	42.85	13.24	2	3.13	320	60	-109	0.6254
2016.682787	42.65	13.34	6	3.54	140	55	-80	0.5464
2016.682927	42.83	13	7	2.84	180	65	30	0.58
2016.683095	42.66	13.34	5	3.17	126	46	-100	0.4427
2016.684192	42.76	13.19	6	3.07	335	55	-85	0.5026
2016.685437	42.86	13.22	2	3.15	321	73	-115	0.6806
2016.6858	42.73	13.19	9	3.11	307	54	-127	0.6077
2016.686378	42.8	13.2	6	3.18	215	60	-60	0.6248
2016.687461	42.67	13.3	9	2.97	355	70	-90	0.6657
2016.687867	42.8	13.24	1	3.3	133	45	-95	0.5438
2016.689257	42.95	13.16	1	2.97	144	47	-105	0.4972
2016.694273	42.84	13.26	3	2.89	195	55	-55	0.6989
2016.695628	42.96	13.16	1	2.96	160	60	-75	0.5931
2016.695924	42.79	13.23	3	3.2	150	55	-80	0.5185
2016.698845	42.68	13.28	4	3.24	150	50	-85	0.6184
2016.699702	42.8	13.22	2	2.99	314	47	-105	0.3992
2016.703446	42.58	13.2	15	3.34	150	70	-40	0.5135
2016.706752	42.86	13.26	2	2.93	280	74	-127	0.6262
2016.709228	42.78	13.13	2	2.91	330	60	-85	0.4169
2016.709322	42.78	13.13	2	3.72	358	61	-96	0.5827
2016.709327	42.78	13.13	2	3.5	2	56	-100	0.5328
2016.709328	42.78	13.14	1	3.26	345	55	-90	0.4797
2016.70957	42.75	13.14	1	2.79	350	50	-95	0.4895
2016.709639	42.76	13.09	7	3.07	43	76	-104	0.7126
2016.713979	42.84	13.23	5	3.21	300	59	-106	0.5393
2016.716066	42.68	13.29	4	3.12	325	80	-50	0.4641
2016.716287	42.82	13.25	2	2.99	312	71	-137	0.6695
2016.71776	39.04	16.45	17	3.29	68	69	-103	0.6455
2016.720495	42.68	13.29	4	2.88	315	75	-60	0.6619
2016.721263	42.67	13.28	4	3.67	325	65	-55	0.6215
2016.721465	42.68	13.29	4	3.2	145	90	70	0.6742
2016.72171	42.81	13.15	6	2.92	300	75	-70	0.6803
2016.721711	42.81	13.15	6	2.92	310	90	-70	0.6237
2016.724855	42.8	13.15	5	3.38	175	90	80	0.6115
2016.727676	42.78	13.13	2	2.79	320	75	-85	0.4721
2016.72906	42.76	13.19	5	3.48	335	60	-80	0.5977
2016.75084	42.9	13.25	5	3.4	175	60	-75	0.5962
2016.75087	42.9	13.24	5	3.54	175	60	-70	0.5577
2016.756806	42.79	13.23	2	3.24	140	55	-80	0.4678
2016.761008	42.86	13.12	5	3.45	107	54	-127	0.5852
2016.763717	42.64	13.22	7	3.14	328	61	-98	0.4933
2016.766867	42.88	13.14	5	2.83	149	66	-97	0.409
2016.768644	42.9	13.25	5	3.23	160	65	-75	0.5193
2016.771431	42.78	13.2	6	2.9	90	65	-55	0.5541
2016.771894	42.75	13.18	3	3.58	148	45	-95	0.5903
2016.771936	42.75	13.19	4	3.12	328	45	-95	0.6166
2016.772562	42.74	13.19	3	3.91	331	46	-100	0.6154
2016.773542	42.74	13.2	3	3.06	165	70	-85	0.484
2016.77376	42.74	13.2	3	3.5	160	60	-85	0.5292
2016.779548	42.86	13.25	1	2.8	295	53	-106	0.5681
2016.781125	42.87	13.07	5	3.14	325	55	-70	0.5479
2016.787358	42.63	13.33	5	3.29	332	51	-98	0.5214
2016.78979	42.89	13.26	3	3.12	145	60	-55	0.4827

2016.793239	42.75	13.18	3	3.04	180	60	-70	0.5584
2016.793436	42.75	13.18	3	3.95	341	46	-100	0.5631
2016.793997	42.85	13.15	5	3.23	355	70	-85	0.61
2016.803297	40.76	15.65	16	3.49	150	89	100	0.6155
2016.812421	43.19	11.05	9	3.53	37	78	112	0.5596
2016.816335	43.38	12.55	1	2.92	145	60	-80	0.5498
2016.818862	43.6	10.99	8	3.94	82	85	-155	0.5534
2016.821628	42.88	13.13	5	5.3	334	60	-93	0.6813
2016.821796	42.88	13.09	6	3.3	339	66	-97	0.6248
2016.821836	42.91	13.12	5	3.33	324	47	-105	0.5687
2016.821846	42.89	13.13	5	3.04	350	60	-75	0.5799
2016.821869	42.91	13.13	5	5.87	162	45	-85	0.7812
2016.821918	42.89	13.07	6	3.87	175	75	55	0.5594
2016.82211	42.87	13.08	5	3.73	329	66	-97	0.6341
2016.822126	42.82	13.26	4	3	134	79	134	0.4694
2016.822143	42.86	13.13	5	4.48	330	60	-90	0.5119
2016.822163	42.86	13.21	4	3.31	163	78	-112	0.4358
2016.822198	42.93	13.16	2	3.14	137	84	125	0.4712
2016.822208	42.87	13.12	5	3.19	6	60	-87	0.4997
2016.82239	42.84	13.17	3	3.44	150	60	-70	0.5058
2016.82243	42.84	13.17	2	3.03	355	60	-45	0.4473
2016.822445	42.99	13.12	2	3.26	146	55	-87	0.4843
2016.822517	42.89	13.06	7	3.17	310	55	-120	0.517
2016.822783	42.84	13.15	5	3.96	339	60	-93	0.5858
2016.822842	42.99	13.13	3	4.1	350	70	-80	0.5355
2016.823224	42.87	13.13	3	3.22	341	73	-115	0.4982
2016.823356	42.87	13.1	5	4.32	348	61	-96	0.5886
2016.823388	42.96	13.15	1	3.01	160	80	-45	0.5675
2016.823807	43.02	13.13	1	3.28	135	59	-106	0.5085
2016.823826	43.02	13.14	1	3.05	128	66	-123	0.4738
2016.824015	42.79	13.16	5	3.22	353	61	-96	0.5913
2016.824254	42.95	13.07	7	3.13	324	66	-116	0.4622
2016.824382	42.84	13.1	5	4.26	355	70	-92	0.6201
2016.824385	42.85	13.11	5	3.85	355	65	-90	0.6201
2016.824392	43.01	13.12	2	3.3	350	50	-65	0.6004
2016.825091	42.87	13.15	3	3.07	287	62	-139	0.5968
2016.825288	42.82	13.12	5	3.24	336	57	-103	0.5715
2016.825355	42.99	13.14	2	3.23	140	55	-90	0.6211
2016.82539	43.03	13.12	2	3.29	121	64	-146	0.5914
2016.825429	42.99	13.15	2	3.22	130	53	-106	0.4422
2016.825479	43	13.14	2	3.15	145	50	-85	0.5965
2016.825575	42.86	13.04	8	3.18	310	67	-136	0.5435
2016.825772	42.89	13.18	2	3.06	330	50	-80	0.4886
2016.826068	42.96	13.14	3	3.04	106	66	-129	0.4382
2016.826184	42.92	13.11	5	3.29	335	55	-60	0.6564
2016.826724	42.87	13.21	1	3.35	150	55	-85	0.4291
2016.826952	42.79	13.12	8	3.63	340	75	-40	0.6081
2016.827407	42.87	13.16	5	3.68	0	75	-80	0.595
2016.827642	42.8	13.14	5	3.18	338	61	-98	0.614
2016.827789	42.88	13.09	6	3.37	328	67	-99	0.5814
2016.828872	42.99	13.05	6	3.36	316	66	-108	0.661
2016.829038	42.85	13.15	3	3.31	25	85	70	0.5717
2016.829517	43.02	13.1	3	3	123	68	-125	0.5364
2016.829607	42.88	13.2	1	3.08	325	55	-90	0.4949
2016.829737	42.81	13.1	7	4.08	330	50	-90	0.5847
2016.829832	42.96	13.08	5	3.12	314	66	-116	0.6106
2016.830389	42.83	13.1	5	3.21	353	61	-96	0.4778
2016.83049	43.06	13.07	5	3.26	160	65	-65	0.6386
2016.831361	42.84	13.11	2	6.33	150	55	-90	0.6296
2016.831577	42.86	13.05	8	3.74	345	90	-55	0.6256
2016.83158	42.83	13.08	8	4.25	5	75	-80	0.7201

2016.83159	42.88	13.19	2	3.64	308	51	-124	0.5424
2016.831622	42.71	13.22	7	3.43	155	55	-55	0.5189
2016.83163	42.93	13.21	4	3.37	270	57	123	0.4621
2016.831632	42.86	13.11	3	3.37	345	80	35	0.4459
2016.831723	42.84	13.12	5	3.48	350	65	-80	0.5534
2016.831786	42.94	13.2	2	3.61	350	50	-65	0.5444
2016.83179	42.84	13.07	7	3.59	335	75	-90	0.5951
2016.831834	44.18	12.24	10	3.66	68	80	118	0.453
2016.831836	42.78	13.08	7	3.75	353	74	-102	0.5128
2016.831855	42.82	13.09	6	3.52	328	67	-99	0.6114
2016.831865	42.92	13.19	2	3.58	298	51	-124	0.5387
2016.831892	42.8	13.19	7	3.53	165	65	-80	0.6751
2016.831892	42.8	13.19	7	3.53	165	65	-80	0.6751
2016.831893	43.06	13.07	5	3.98	160	60	-70	0.6696
2016.831904	42.85	13.12	9	3.22	305	68	-118	0.4691
2016.831929	42.89	13.14	5	3.47	325	55	-75	0.5919
2016.831964	42.84	13.06	9	4.04	340	90	-85	0.7422
2016.83198	42.84	13.08	6	4.5	330	75	-91	0.6644
2016.832017	42.93	13.2	2	3.66	345	55	-60	0.492
2016.832017	42.93	13.2	2	3.66	345	55	-60	0.492
2016.832029	42.85	13.14	3	3.31	350	75	-91	0.4988
2016.832034	42.92	13.15	2	3.32	306	52	-117	0.4691
2016.832041	42.92	13.19	4	3.07	83	74	143	0.4959
2016.832043	42.91	13.2	2	3.19	165	50	-65	0.5013
2016.832061	42.73	13.19	2	3.1	149	66	-116	0.4912
2016.832077	42.9	13.2	2	3.26	338	50	-94	0.5933
2016.832086	42.73	13.15	6	3.27	333	45	-95	0.5766
2016.832108	42.77	13.06	7	3.34	314	54	-110	0.5941
2016.832116	42.81	13.2	7	3.15	170	70	-92	0.6239
2016.832122	43.02	13.12	1	3.45	335	45	-90	0.5624
2016.832125	43.01	13.12	4	3.26	299	81	-102	0.4004
2016.832147	42.8	13.16	6	4.09	155	75	-50	0.5772
2016.832161	42.9	13.22	4	3.31	188	69	-148	0.4084
2016.832171	42.91	13.2	1	3.06	292	61	-118	0.4406
2016.832201	42.94	13.21	1	3.54	158	56	-97	0.4961
2016.832209	42.79	13.07	7	3.23	329	71	-95	0.5622
2016.832222	42.91	13.2	2	3.46	151	46	-100	0.5777
2016.832223	42.78	13.09	7	3.75	165	75	87	0.6374
2016.832237	42.68	13.21	5	3.08	341	69	-112	0.5081
2016.832242	42.76	13.06	6	3.39	360	88	-100	0.6818
2016.832281	42.9	13.16	2	3.6	335	60	-65	0.5193
2016.832287	42.93	13.21	3	3	185	85	-35	0.4512
2016.832291	42.69	13.19	7	3.11	347	71	-107	0.5729
2016.83233	42.94	13.2	2	3.23	165	65	-80	0.5095
2016.832336	42.93	13.2	2	3.14	132	50	-113	0.4894
2016.832343	42.84	13.04	7	3.02	343	67	-101	0.5123
2016.832345	42.8	13.14	6	3.27	168	56	-97	0.555
2016.832356	42.77	13.2	3	2.94	335	50	-65	0.4682
2016.832369	42.86	13.1	8	2.95	220	55	-50	0.5343
2016.832437	43.06	13.07	5	3.59	160	55	-70	0.5857
2016.832449	42.82	13.16	6	3.05	321	86	115	0.5507
2016.832452	42.78	13.17	5	2.97	83	74	-102	0.4753
2016.832458	42.83	13.05	6	3.18	330	70	-90	0.5492
2016.832519	42.92	13.21	3	2.9	296	58	-138	0.4421
2016.832551	43.07	13.07	5	3.15	160	60	-75	0.5382
2016.832562	42.81	13.1	7	2.99	107	66	141	0.5706
2016.832594	42.87	13.07	7	3.1	306	63	-127	0.504
2016.832597	42.89	13.16	2	3.44	128	48	-109	0.5483
2016.832627	42.95	13.18	4	3.02	170	75	35	0.375
2016.83263	42.91	13.14	6	3.57	175	50	-60	0.5957
2016.832639	42.88	13.21	2	3.15	310	71	-120	0.5146

2016.832663	42.92	13.21	1	2.79	145	53	-106	0.4172
2016.83269	42.79	13.15	1	3.85	355	45	-90	0.5557
2016.832725	42.81	13.1	5	3.4	325	70	-88	0.6205
2016.832761	42.8	13.15	1	3.05	166	46	-100	0.4884
2016.832937	42.81	13.09	8	2.99	155	70	60	0.4125
2016.832967	42.93	13.2	4	3.29	274	67	153	0.4925
2016.832977	42.94	13.14	6	3.27	326	57	-103	0.5394
2016.833132	42.8	13.16	1	2.81	177	45	-85	0.4867
2016.833143	42.91	13.16	1	3.29	150	50	-80	0.5197
2016.83319	42.9	13.2	4	3.06	290	73	148	0.5478
2016.833195	42.81	13.19	7	3.41	175	70	-70	0.6749
2016.833233	42.92	13.21	4	3.19	20	65	35	0.4375
2016.833237	42.91	13.05	7	3.31	300	55	-120	0.6027
2016.83327	42.72	13.18	1	2.89	345	85	-175	0.4997
2016.833319	42.78	13.12	7	3.44	339	79	-101	0.5952
2016.833326	42.83	13.09	4	3.54	147	69	148	0.4215
2016.833355	42.78	13.1	7	3.2	340	85	-45	0.6665
2016.833365	42.75	13.19	4	2.98	116	82	-145	0.5586
2016.833367	42.73	13.19	2	2.85	175	50	-70	0.6116
2016.833391	42.75	13.13	7	3.34	328	74	-102	0.6465
2016.833391	42.75	13.13	7	3.34	328	74	-102	0.6465
2016.83342	42.8	13.1	7	3.19	8	67	-99	0.6348
2016.83343	42.99	13.11	2	2.82	145	65	-70	0.5012
2016.83345	42.79	13.04	6	3.37	335	90	-75	0.7299
2016.833514	42.74	13.18	6	2.98	305	60	-60	0.5715
2016.833539	42.9	13.15	2	3.4	160	60	-65	0.636
2016.833566	42.78	13.12	11	3.11	91	78	144	0.593
2016.833626	42.78	13.11	7	2.94	325	85	-65	0.6135
2016.833655	43.07	13.07	5	3.55	165	60	-70	0.6117
2016.833673	42.62	13.3	5	3.46	160	65	-85	0.6844
2016.833686	42.84	13.05	5	3.17	252	80	165	0.7493
2016.833727	42.77	13.09	7	4.03	354	84	-104	0.6939
2016.833737	42.95	13.19	2	3.61	101	58	-138	0.5189
2016.833747	42.72	13.19	4	2.95	343	50	-94	0.6141
2016.833769	42.94	13.14	7	3.06	323	66	-123	0.6308
2016.833828	42.89	13.19	2	3.23	330	50	-80	0.5216
2016.833831	42.84	13.06	7	3.38	340	60	-90	0.5514
2016.833882	42.79	13.07	6	3.21	327	70	-105	0.6326
2016.833937	42.77	13.21	3	3.12	312	51	-98	0.6279
2016.834049	42.77	13.21	5	3.74	309	47	-105	0.5416
2016.834141	42.84	13.13	5	3.98	355	70	-85	0.5996
2016.834315	43.02	13.08	5	3.44	165	55	-65	0.5965
2016.834321	42.81	13.14	5	3.42	328	61	-96	0.6035
2016.834354	42.81	13.19	7	3.23	165	75	-65	0.6
2016.834423	42.82	13.15	7	3.48	146	66	-129	0.671
2016.834428	42.91	13.11	8	2.9	289	86	-135	0.5436
2016.834507	42.9	13.21	2	2.87	200	50	-60	0.5328
2016.834591	42.77	13.08	7	3.07	279	87	-130	0.6223
2016.83463	42.69	13.27	7	3.06	340	80	-80	0.5778
2016.834728	42.92	13.22	2	3.13	345	50	-75	0.4941
2016.834987	43.06	13.13	2	2.92	131	63	-127	0.4721
2016.835056	42.75	13.14	8	3.12	323	86	-145	0.583
2016.835146	42.9	13.14	5	3.3	150	55	-75	0.5171
2016.835297	42.77	13.05	6	3.18	160	75	75	0.5859
2016.835346	42.95	13.2	2	3.22	330	50	-80	0.4644
2016.835379	42.74	13.15	1	2.98	215	65	-65	0.4859
2016.835656	42.94	13.21	2	3.07	125	68	-118	0.4742
2016.835741	42.89	13.18	4	3.01	265	73	148	0.4309
2016.835885	42.81	13.05	7	3.21	286	73	-115	0.5839
2016.836058	42.95	13.2	1	3.13	340	50	-75	0.5627
2016.836135	42.85	13.08	8	3.04	331	73	-115	0.6069

2016.836143	42.93	13.06	6	3.01	326	73	-115	0.6018
2016.836361	42.66	13.22	7	3.23	314	54	-110	0.6675
2016.836377	42.77	13.03	7	2.84	325	90	-115	0.4753
2016.836443	42.91	13.31	17	3.49	105	68	-118	0.6629
2016.836627	42.78	13.14	6	2.97	146	46	-100	0.5206
2016.836817	43.01	13.14	1	3.32	147	51	-98	0.6543
2016.836831	43.01	13.14	1	3.15	146	46	-100	0.6193
2016.83697	43	13.16	7	4.6	110	81	-150	0.6314
2016.837294	43.61	11.01	9	3.27	180	70	30	0.5108
2016.83738	42.73	13.21	5	3.14	155	60	-65	0.5566
2016.837397	42.69	13.15	9	3.05	110	70	142	0.618
2016.837568	42.9	13.16	3	2.95	293	57	-130	0.5212
2016.837799	42.91	13.17	1	3.39	318	45	-95	0.4852
2016.837889	42.8	13.11	11	3.18	286	77	-128	0.663
2016.837945	42.93	13.21	2	3.28	335	45	-90	0.5394
2016.838011	42.8	13.1	7	3.19	330	55	-65	0.6232
2016.838113	42.81	13.13	8	3.35	130	75	-65	0.6527
2016.838206	42.73	13.22	6	3.32	317	73	-108	0.6069
2016.838235	42.8	13.03	7	3.67	335	80	-80	0.7055
2016.839426	42.91	13.13	5	2.94	322	69	-131	0.6037
2016.839467	43.04	13.06	6	2.92	316	66	-108	0.6374
2016.839496	42.78	13.08	6	3.15	324	85	-120	0.6786
2016.839498	43.03	13.06	6	3.33	325	65	-90	0.7034
2016.839559	42.8	13.17	6	3.23	111	63	-127	0.7057
2016.839666	42.71	13.19	5	3.13	235	60	-40	0.6448
2016.839875	43	13.15	1	2.99	332	45	-85	0.5433
2016.840076	42.78	13.21	3	3.09	330	60	-60	0.5455
2016.840441	42.88	13.15	7	3.18	328	56	-113	0.6114
2016.840539	42.8	13.15	7	2.8	59	83	-109	0.6582
2016.840606	43.03	13.04	6	3.26	340	65	-80	0.5488
2016.840727	42.89	13.15	5	3.02	332	48	-71	0.4967
2016.841012	42.93	13.21	2	3.11	15	75	20	0.4467
2016.841013	42.94	13.15	5	3.27	328	61	-98	0.537
2016.841033	42.88	13.07	1	3.61	322	51	-98	0.502
2016.841143	42.9	13.2	2	2.75	277	86	150	0.4898
2016.841298	42.88	13.19	2	3.29	134	47	-105	0.4777
2016.841323	43.04	13.06	5	3.06	340	55	-70	0.5937
2016.841323	43.04	13.06	5	3.06	340	55	-70	0.5937
2016.841596	43.03	13.05	5	4.69	324	71	-95	0.578
2016.84166	42.86	13.07	9	2.84	185	60	-80	0.4993
2016.841679	42.66	13.31	2	3.05	154	65	-95	0.4982
2016.841732	43.02	13.06	5	2.96	325	70	-90	0.6884
2016.841831	42.97	13.15	5	3.2	155	55	-55	0.5188
2016.842401	42.83	13.12	6	3.35	330	55	-90	0.5437
2016.842695	42.78	13.21	4	3.09	8	67	-101	0.577
2016.842895	42.91	13.22	2	3.36	323	57	-130	0.4827
2016.842939	42.92	13.2	2	3.21	180	55	-60	0.5544
2016.84303	42.69	13.18	9	3.73	327	56	-100	0.5733
2016.843203	42.99	13.08	5	3.37	333	69	-103	0.5987
2016.843516	43.03	13.06	6	3.11	317	56	-100	0.5098
2016.843725	43.02	13.05	5	3.06	338	77	-106	0.5221
2016.843869	42.79	13.11	7	3.1	4	84	-114	0.8014
2016.84394	42.76	13.05	7	3.12	310	53	-106	0.5922
2016.844195	42.87	13.1	7	2.93	313	61	-132	0.7073
2016.844296	42.87	13.07	7	3.22	329	66	-97	0.6675
2016.844507	42.68	13.21	9	3.19	307	54	-127	0.7766
2016.844774	42.9	13.16	2	2.94	140	60	-90	0.6684
2016.84497	42.78	13.14	6	3.01	323	56	-97	0.5699
2016.845398	43.01	13.07	5	3	152	45	-85	0.5193
2016.845493	42.87	13.13	3	3.12	102	54	-127	0.536
2016.845916	42.98	13.13	3	2.83	10	65	-30	0.4233

2016.846967	42.79	13.13	6	3.33	332	56	-83	0.6112
2016.847074	42.83	13.23	11	3.06	315	75	-50	0.5299
2016.84724	42.88	13.13	3	2.84	355	65	-80	0.5281
2016.847766	43.06	13.06	5	2.93	321	52	-102	0.7223
2016.847939	42.7	13.15	8	3.11	325	80	-80	0.7741
2016.847954	42.68	13.18	7	2.97	308	51	-124	0.689
2016.848106	42.91	13.19	2	3.11	309	64	-114	0.5527
2016.848257	42.94	13.21	1	3.17	170	60	-75	0.44
2016.848258	42.95	13.23	1	3.59	155	55	-95	0.4776
2016.848276	42.95	13.22	1	3.11	155	55	-75	0.6146
2016.848607	42.79	13.18	7	2.94	102	62	-139	0.5588
2016.848674	42.98	13.13	2	3.32	327	50	-113	0.6437
2016.84903	42.75	13.19	2	3.31	159	55	-93	0.6034
2016.84918	42.95	13.2	1	3.23	155	60	-70	0.7049
2016.849203	42.94	13.22	2	2.87	175	70	-70	0.5945
2016.849441	42.73	13.19	5	3.4	180	50	-60	0.5739
2016.849552	43.04	13.09	2	2.95	5	90	0	0.7965
2016.84956	42.95	13.21	2	3.07	300	55	-120	0.7124
2016.850105	43.06	13.06	5	3.62	311	64	-106	0.4804
2016.850266	42.78	13.2	4	3.13	315	65	-60	0.6059
2016.851805	42.81	13.19	6	3.41	140	65	-75	0.5255
2016.853267	42.88	13.19	2	3.08	330	50	-85	0.601
2016.853891	42.87	13.08	9	3.19	197	77	106	0.6821
2016.854392	43.02	13.14	2	3.24	332	50	-86	0.5021
2016.854576	42.9	13.18	1	2.73	308	50	-94	0.579
2016.854615	42.89	13.15	9	3.73	326	64	-106	0.6594
2016.855799	42.9	13.18	2	3.01	329	66	-116	0.6655
2016.856133	42.83	13.04	7	3.22	328	73	-100	0.7416
2016.85747	42.81	12.77	7	3.33	290	70	-55	0.7238
2016.858051	42.55	13.25	3	3.04	165	55	-90	0.714
2016.858294	43	13.15	2	3.38	340	45	-90	0.4566
2016.85836	43	13.16	2	2.98	149	54	-110	0.6199
2016.858632	42.66	13.19	9	3.6	180	50	-60	0.6491
2016.858663	42.73	13.18	9	3.28	185	55	-80	0.6358
2016.862232	42.89	13.13	3	3.44	359	65	-92	0.5239
2016.862922	42.78	13.05	7	3.34	315	90	-80	0.7889
2016.867153	42.9	13.18	2	2.94	318	56	-97	0.5902
2016.867551	43	13.13	2	3.73	160	50	-85	0.4966
2016.867599	42.99	13.14	2	3.55	165	50	-80	0.4872
2016.867797	42.72	13.21	5	4.1	331	46	-100	0.6241
2016.868231	42.94	13.2	1	2.91	175	60	-85	0.701
2016.868318	43.03	13.07	5	2.98	345	65	-80	0.5135
2016.868686	42.8	13.14	6	3.53	175	50	-90	0.6342
2016.868722	42.92	13.21	3	3.16	105	76	-159	0.6908
2016.868776	42.82	13.1	8	3.05	10	65	-80	0.6441
2016.868844	42.82	13.1	10	3.02	143	71	159	0.604
2016.869224	42.55	13.23	3	3.17	140	60	-109	0.5959
2016.871474	42.95	13.09	6	3.21	315	55	-120	0.5389
2016.871763	42.86	13.16	8	3.88	324	64	-114	0.676
2016.872216	43.01	13.06	5	3.14	350	60	-70	0.5334
2016.873226	42.98	13.06	6	3.15	335	80	-87	0.7348
2016.873842	42.94	13.15	9	3.67	341	52	-102	0.6638
2016.876261	43.03	13.07	3	3	160	55	-70	0.6453
2016.876425	43.03	13.08	5	3.21	141	55	-87	0.6396
2016.876931	42.75	13.21	5	3.17	355	50	-90	0.6194
2016.878152	43.04	13.11	2	2.87	279	64	146	0.672
2016.878401	42.8	13.13	7	3.8	125	80	-75	0.7088
2016.878415	43.03	13.1	2	2.83	185	85	-35	0.5972
2016.882432	42.77	13.2	10	3.32	314	76	-133	0.5769
2016.885384	43.01	13.07	6	3.22	325	55	-90	0.6311
2016.887501	42.86	13.19	4	3.08	246	72	154	0.7105

2016.888171	42.64	13.22	8	3.24	0	73	-148	0.702
2016.88933	42.95	13.16	9	3.16	348	61	-96	0.5956
2016.891062	44.43	9.79	4	3.18	143	56	-97	0.601
2016.891145	43.01	13.08	5	3.07	330	55	-75	0.549
2016.891876	43.02	13.08	4	2.94	315	50	-85	0.5475
2016.89444	43.01	13.13	2	2.85	141	46	-100	0.5656
2016.89618	42.84	13.12	5	3.46	334	55	-93	0.6747
2016.896354	42.93	13.15	2	3.16	350	60	-45	0.7215
2016.896899	43.05	13.1	3	2.88	195	90	-15	0.6827
2016.897076	43.05	13.1	3	3.15	10	85	10	0.752
2016.898587	42.72	13.28	10	3.17	322	76	-111	0.7473
2016.902985	43.02	13.08	5	3.13	330	55	-70	0.6286
2016.903194	42.99	13.15	2	2.79	160	55	-75	0.7626
2016.904893	42.86	12.94	3	3.11	80	90	-155	0.7102
2016.907554	42.8	13.21	5	3.37	140	55	-65	0.5368
2016.908889	43.01	13.07	5	3.12	335	65	-75	0.6939
2016.908957	43.01	13.07	3	3.1	335	55	-50	0.7408
2016.909285	43.02	13.08	5	3.59	325	50	-70	0.6016
2016.909332	43.02	13.08	5	3.66	143	45	-95	0.6112
2016.909364	43.02	13.07	4	3.02	334	47	-105	0.7727
2016.909457	43.02	13.07	4	2.96	130	55	-95	0.6875
2016.909573	43.02	13.07	5	3.86	131	46	-100	0.6318
2016.910429	42.65	13.22	8	3.16	129	76	154	0.6157
2016.910587	42.81	12.76	5	3.18	280	65	-60	0.606
2016.910734	43.02	13.07	5	3.61	136	46	-100	0.6312
2016.911699	43.02	13.07	5	3.42	323	61	-98	0.69
2016.912395	43.02	13.07	5	3.48	335	50	-70	0.6188
2016.912783	42.81	12.78	5	3.35	265	50	-80	0.6269
2016.912977	42.76	13.24	7	3.48	335	55	-85	0.5928
2016.913648	43.02	13.12	2	3.06	155	50	-80	0.5986
2016.914416	42.53	13.29	7	4.34	334	71	-95	0.6433
2016.9169	42.75	13.25	9	3.03	344	86	-115	0.5902
2016.919344	43	13.08	5	3.96	328	56	-97	0.507
2016.919963	43.04	13.07	6	3.16	347	56	-83	0.7057
2016.920324	43.04	13.07	6	3.06	325	50	-90	0.6438
2016.92251	43.01	13.14	2	2.99	147	51	-98	0.6833
2016.923738	42.99	13.08	5	3.18	330	60	-85	0.62
2016.926108	43.01	13.06	5	3.14	307	62	-101	0.7412
2016.928549	43.04	13.1	3	3.29	10	90	-10	0.8111
2016.930139	42.56	13.29	6	3.15	335	55	-85	0.7635
2016.931948	40.54	15.82	10	3.72	288	56	-113	0.4703
2016.932488	42.88	13.16	5	2.87	314	71	-126	0.5898
2016.932907	42.83	13.01	1	2.94	97	54	-127	0.5938
2016.933439	43.01	13.07	5	2.92	322	51	-98	0.6267
2016.93388	43.05	13.09	3	2.93	175	65	-45	0.644
2016.935104	42.87	13.22	7	2.95	90	60	-90	0.6444
2016.936065	42.56	13.28	6	3.13	319	66	-97	0.8009
2016.938131	42.84	13.03	7	3.25	325	70	-90	0.7541
2016.940715	43.02	13.07	5	3.41	345	65	-45	0.6286
2016.940729	44.33	10.5	6	3.83	170	50	-65	0.6349
2016.941442	43.02	13.07	5	3.27	123	48	-109	0.6235
2016.94358	43.02	13.07	4	3.02	324	54	-110	0.638
2016.946825	42.9	13.11	3	4.05	25	65	-70	0.4957
2016.947883	38.06	14.73	7	3.34	50	90	55	0.4595
2016.950041	42.74	13.04	8	3.4	330	70	-85	0.672
2016.953301	42.99	13.07	5	3.4	339	71	-95	0.5464
2016.953996	42.65	13.3	3	3.69	154	60	-93	0.6099
2016.955103	43.02	13.07	5	3.24	330	55	-85	0.561
2016.955109	43.02	13.06	5	3.48	335	55	-75	0.5846
2016.95539	43.02	13.06	5	3.27	340	60	-75	0.5714
2016.956343	42.56	13.27	6	3.18	325	50	-85	0.5866

2016.958023	42.93	13.16	2	3.06	104	60	-145	0.6514
2016.96447	42.92	13.16	2	3.32	355	70	-55	0.5797
2016.966562	42.93	13.2	2	3.2	350	55	-60	0.6765
2016.966938	42.92	13.17	2	3	355	70	-35	0.6174
2016.968429	42.78	13.15	6	3.19	145	53	-106	0.5564
2016.988609	42.92	13.2	2	3.42	323	48	-109	0.5447
2017.005891	42.8	12.75	4	3.91	72	85	-155	0.5715
2017.007233	42.57	13.24	3	2.97	180	70	-45	0.6243
2017.012352	43.01	13.11	1	2.73	140	65	-75	0.5665
2017.01502	42.97	13.07	5	3.18	293	66	-123	0.538
2017.015968	42.44	13.27	7	3.25	118	51	-124	0.6708
2017.023395	42.43	13.27	7	2.99	285	70	-142	0.6639
2017.024636	42.42	13.28	7	3.46	288	66	-141	0.6409
2017.034845	43.08	13.07	5	3.36	175	60	-60	0.5949

Table S3. Dislocation parameters for the earthquakes used in this study to compute cumulative stress changes.

#TYP	#	LONCEN	LATCEN	DCEN	STR	DIP	HORLEN	DIPLEN	SS(m)	DS(m)	OP(m)	RAKE
Dislocation	1	13.2200	42.7100	5.0000	155.0000	50.000	12.0865	7.9506	0.0306	0.3496	0.	-85.
Dislocation	2	13.2800	42.6100	5.0000	115.0000	57.000	1.5538	2.6134	-0.0246	0.0378	0.	-123.
Dislocation	3	13.1500	42.7900	5.0000	136.0000	46.000	4.7984	4.8173	-0.0242	0.1372	0.	-100.
Dislocation	4	13.1400	42.8000	5.0000	151.0000	57.000	0.7563	1.7685	-0.0049	0.0214	0.	-103.
Dislocation	5	13.2700	42.6100	7.0000	152.0000	61.000	0.5533	1.4928	0.0017	0.016	0.	-84.
Dislocation	6	13.2400	42.6200	6.0000	150.0000	60.000	0.9790	2.0342	0.	0.0284	0.	-90.
Dislocation	7	13.1200	42.7700	3.0000	160.0000	50.000	1.2847	2.3572	0.	0.0373	0.	-90.
Dislocation	8	13.1500	42.8200	7.0000	155.0000	65.000	1.6406	2.6915	0.0123	0.046	0.	-75.
Dislocation	9	13.2500	42.8000	3.0000	40.0000	65.000	0.6086	1.5718	0.0135	0.0114	0.	-40.0001
Dislocation	10	13.2200	42.6600	7.0000	159.0000	55.000	1.0767	2.1419	-0.0016	0.0312	0.	-93.
Dislocation	11	13.1500	42.7800	5.0000	137.0000	63.000	0.3258	1.1200	-0.0049	0.0081	0.	-121.
Dislocation	12	13.1700	42.8000	6.0000	168.0000	50.000	0.2257	0.9179	-0.0005	0.0065	0.	-94.
Dislocation	13	13.2100	42.6500	9.0000	147.0000	56.000	0.8095	1.8348	-0.0041	0.0231	0.	-100.
Dislocation	14	13.2100	42.7500	5.0000	159.0000	72.000	1.3564	2.4277	-0.0062	0.0389	0.	-99.
Dislocation	15	13.2300	42.6900	7.0000	157.0000	50.000	0.3085	1.0874	-0.0035	0.0082	0.	-113.
Dislocation	16	13.3300	42.6200	2.0000	138.0000	61.000	0.5922	1.5488	-0.0024	0.017	0.	-98.
Dislocation	17	13.3000	42.6100	3.0000	140.0000	55.000	0.2383	0.9454	0.	0.0069	0.	-90.
Dislocation	18	13.2500	42.6100	7.0000	144.0000	65.000	0.2693	1.0102	-0.0007	0.0078	0.	-95.
Dislocation	19	13.2900	42.6000	5.0000	125.0000	55.000	1.4129	2.4820	-0.0205	0.0355	0.	-120.
Dislocation	20	13.2900	42.5900	5.0000	122.0000	54.000	0.3940	1.2416	-0.0069	0.0091	0.	-127.
Dislocation	21	13.2900	42.6700	3.0000	155.0000	55.000	0.4897	1.3970	0.	0.0142	0.	-90.
Dislocation	22	13.2300	42.7000	7.0000	180.0000	55.000	0.2693	1.0102	0.0045	0.0064	0.	-55.
Dislocation	23	13.2900	42.6200	5.0000	138.0000	48.000	0.2551	0.9808	-0.0024	0.007	0.	-109.
Dislocation	24	13.2900	42.6000	5.0000	127.0000	50.000	2.2121	3.1652	-0.0251	0.0591	0.	-113.
Dislocation	25	13.3000	42.6200	5.0000	159.0000	55.000	0.2922	1.0558	-0.0004	0.0085	0.	-93.
Dislocation	26	13.2100	42.7500	7.0000	120.0000	70.000	0.2844	1.0404	0.	-0.0083	0.	90.
Dislocation	27	13.1500	42.7700	5.0000	167.0000	71.000	0.3487	1.1620	-0.003	0.0097	0.	-107.
Dislocation	28	13.2900	42.5700	7.0000	155.0000	55.000	0.1792	0.8098	0.0009	0.0051	0.	-80.
Dislocation	29	13.3000	42.6100	5.0000	128.0000	51.000	0.1697	0.7863	-0.0028	0.0041	0.	-124.
Dislocation	30	13.2900	42.6000	5.0000	150.0000	60.000	0.2053	0.8718	0.0015	0.0058	0.	-75.
Dislocation	31	13.1500	42.6900	7.0000	143.0000	61.000	0.4160	1.2788	-0.0013	0.012	0.	-96.
Dislocation	32	13.1500	42.7900	5.0000	175.0000	65.000	0.2351	0.9384	0.0023	0.0064	0.	-70.
Dislocation	33	13.2600	42.8400	2.0000	170.0000	55.000	0.2551	0.9808	0.0037	0.0064	0.	-60.
Dislocation	34	13.2400	42.8400	2.0000	175.0000	50.000	0.5922	1.5488	0.0073	0.0156	0.	-65.
Dislocation	35	13.2500	42.8400	2.0000	175.0000	55.000	0.7360	1.7426	0.0107	0.0185	0.	-60.
Dislocation	36	13.2500	42.8400	3.0000	165.0000	65.000	0.1866	0.8279	0.0031	0.0044	0.	-55.
Dislocation	37	13.2400	42.8400	2.0000	175.0000	65.000	0.3994	1.2508	0.0058	0.01	0.	-60.
Dislocation	38	13.3100	42.5500	3.0000	150.0000	50.000	0.3128	1.0955	0.0031	0.0085	0.	-70.
Dislocation	39	13.2300	42.7700	4.0000	165.0000	85.000	0.1461	0.7251	0.0027	-0.0033	0.	50.
Dislocation	40	13.1800	42.7900	5.0000	121.0000	52.000	0.2320	0.9315	-0.0014	0.0066	0.	-102.
Dislocation	41	13.2500	42.8400	2.0000	175.0000	65.000	0.4392	1.3170	0.0064	0.011	0.	-60.
Dislocation	42	13.2600	42.5900	7.0000	130.0000	53.000	0.3681	1.1967	-0.0029	0.0103	0.	-106.
Dislocation	43	13.3100	42.6000	5.0000	144.0000	47.000	0.2586	0.9881	-0.0019	0.0073	0.	-105.
Dislocation	44	13.2100	42.7200	7.0000	149.0000	54.000	0.3258	1.1200	-0.0032	0.0089	0.	-110.
Dislocation	45	13.2300	42.8000	5.0000	124.0000	66.000	0.2693	1.0102	-0.001	0.0078	0.	-97.
Dislocation	46	13.2900	42.6300	5.0000	140.0000	55.000	0.2962	1.0637	0.0007	0.0086	0.	-85.
Dislocation	47	13.1100	42.7800	10.0000	103.0000	57.000	0.1944	0.8464	-0.0036	0.0043	0.	-130.
Dislocation	48	13.2900	42.5900	5.0000	159.0000	71.000	0.4638	1.3564	-0.0012	0.0134	0.	-95.
Dislocation	49	13.1200	42.7700	9.0000	155.0000	50.000	0.4104	1.2694	-0.001	0.0119	0.	-95.
Dislocation	50	13.2400	42.8200	5.0000	206.0000	60.000	1.0198	2.0797	0.0015	0.0296	0.	-87.
Dislocation	51	13.1400	42.8200	5.0000	160.0000	55.000	0.6169	1.5834	0.0016	0.0178	0.	-85.
Dislocation	52	13.2000	42.7400	5.0000	144.0000	47.000	0.2383	0.9454	-0.0018	0.0067	0.	-105.

Dislocation	53	13.2000	42.7600	7.0000	165.0000	50.000	0.3783	1.2145	0.0038	0.0103	0.	-70.
Dislocation	54	13.1900	42.7500	6.0000	131.0000	46.000	0.4638	1.3564	-0.0023	0.0133	0.	-100.
Dislocation	55	13.1400	42.7300	4.0000	132.0000	75.000	0.1652	0.7748	-0.0036	-0.0032	0.	137.9999
Dislocation	56	13.1500	42.8300	6.0000	119.0000	77.000	0.1744	0.7980	-0.0031	-0.004	0.	128.
Dislocation	57	13.2200	42.8600	4.0000	185.0000	80.000	0.2621	0.9954	0.0072	-0.0026	0.	20.
Dislocation	58	13.1400	42.8000	6.0000	160.0000	55.000	0.3347	1.1366	0.0041	0.0088	0.	-65.
Dislocation	59	13.1900	42.7300	8.0000	173.0000	73.000	0.1792	0.8098	-0.0009	0.0051	0.	-100.
Dislocation	60	13.2600	42.8200	3.0000	158.0000	61.000	0.2025	0.8654	-0.0039	0.0044	0.	-132.
Dislocation	61	13.1600	42.8100	7.0000	50.0000	89.000	0.2383	0.9454	-0.0018	0.0067	0.	-105.
Dislocation	62	13.1800	42.7600	6.0000	132.0000	56.000	0.2730	1.0177	-0.0014	0.0078	0.	-100.
Dislocation	63	13.1400	42.8400	5.0000	160.0000	60.000	0.7771	1.7947	0.002	0.0225	0.	-85.
Dislocation	64	13.2400	42.8700	4.0000	97.0000	81.000	0.3783	1.2145	-0.0103	-0.0038	0.	160.
Dislocation	65	13.2400	42.7600	8.0000	165.0000	75.000	0.3258	1.1200	0.0054	0.0077	0.	-55.
Dislocation	66	13.2600	42.8300	5.0000	141.0000	79.000	0.4333	1.3074	-0.0087	0.009	0.	-134.
Dislocation	67	13.1300	42.8300	5.0000	165.0000	60.000	0.3583	1.1792	0.0018	0.0102	0.	-80.
Dislocation	68	13.1600	42.7800	5.0000	164.0000	65.000	0.3783	1.2145	-0.0004	0.011	0.	-92.
Dislocation	69	13.2400	42.7500	5.0000	130.0000	45.000	0.3887	1.2325	0.	0.0113	0.	-90.
Dislocation	70	13.1800	42.8500	11.0000	117.0000	61.000	0.1866	0.8279	-0.0025	0.0048	0.	-118.
Dislocation	71	13.3100	42.6200	5.0000	145.0000	60.000	0.4964	1.4073	0.0025	0.0142	0.	-80.
Dislocation	72	13.2300	42.8600	5.0000	135.0000	50.000	0.2483	0.9665	0.	0.0072	0.	-90.
Dislocation	73	13.2400	42.8100	3.0000	135.0000	70.000	0.2227	0.9112	-0.0051	0.004	0.	-142.
Dislocation	74	13.1700	42.8100	7.0000	40.0000	80.000	0.2517	0.9736	0.0071	-0.0019	0.	15.
Dislocation	75	13.3000	42.5600	6.0000	121.0000	69.000	0.3393	1.1450	-0.0037	0.0091	0.	-112.
Dislocation	76	13.1400	42.7500	2.0000	195.0000	50.000	0.1607	0.7635	0.002	0.0042	0.	-65.
Dislocation	77	9.6000	44.5000	3.0000	77.0000	76.000	0.2383	0.9454	-0.0025	0.0065	0.	-111.
Dislocation	78	13.1300	42.7700	2.0000	158.0000	61.000	1.0337	2.0951	-0.0042	0.0297	0.	-98.
Dislocation	79	13.2000	42.8100	3.0000	158.0000	74.000	0.1792	0.8098	-0.0011	0.0051	0.	-102.
Dislocation	80	13.2600	42.9300	4.0000	170.0000	80.000	0.1892	0.8341	0.0023	0.005	0.	-65.
Dislocation	81	13.2100	42.8700	4.0000	104.0000	85.000	1.2334	2.3057	-0.0353	-0.0062	0.	170.
Dislocation	82	13.2200	42.8700	4.0000	190.0000	70.000	0.2416	0.9524	0.0064	-0.003	0.	25.
Dislocation	83	13.2200	42.8600	2.0000	115.0000	67.000	0.2081	0.8782	-0.0043	0.0042	0.	-136.
Dislocation	84	7.5200	43.9800	9.0000	112.0000	81.000	0.3258	1.1200	-0.0089	-0.0032	0.	160.
Dislocation	85	13.2300	42.8500	2.0000	132.0000	63.000	0.1607	0.7635	-0.0024	0.004	0.	-121.
Dislocation	86	13.2100	42.8500	4.0000	107.0000	81.000	0.3393	1.1450	-0.0093	-0.0034	0.	160.
Dislocation	87	13.3100	42.6300	7.0000	159.0000	65.000	0.1697	0.7863	-0.0004	0.0049	0.	-95.
Dislocation	88	13.2400	42.8500	2.0000	140.0000	60.000	0.2551	0.9808	-0.0024	0.007	0.	-109.
Dislocation	89	13.3400	42.6500	6.0000	140.0000	55.000	0.4452	1.3268	0.0022	0.0127	0.	-80.
Dislocation	90	13.0000	42.8300	7.0000	180.0000	65.000	0.1720	0.7921	0.0043	-0.0025	0.	30.
Dislocation	91	13.3400	42.6600	5.0000	126.0000	46.000	0.2693	1.0102	-0.0014	0.0077	0.	-100.
Dislocation	92	13.1900	42.7600	6.0000	155.0000	55.000	0.2351	0.9384	0.0006	0.0068	0.	-85.
Dislocation	93	13.2200	42.8600	2.0000	141.0000	73.000	0.2621	0.9954	-0.0032	0.0069	0.	-115.
Dislocation	94	13.1900	42.7300	9.0000	127.0000	54.000	0.2483	0.9665	-0.0043	0.0058	0.	-127.
Dislocation	95	13.2000	42.8000	6.0000	215.0000	60.000	0.2730	1.0177	0.004	0.0069	0.	-60.
Dislocation	96	13.3000	42.6700	9.0000	175.0000	70.000	0.2053	0.8718	0.	0.006	0.	-90.
Dislocation	97	13.2400	42.8000	1.0000	133.0000	45.000	0.3214	1.1117	-0.0008	0.0093	0.	-95.
Dislocation	98	13.1600	42.9500	1.0000	144.0000	47.000	0.2053	0.8718	-0.0015	0.0058	0.	-105.
Dislocation	99	13.2600	42.8400	3.0000	195.0000	55.000	0.1841	0.8219	0.0031	0.0044	0.	-55.
Dislocation	100	13.1600	42.9600	1.0000	160.0000	60.000	0.2025	0.8654	0.0015	0.0057	0.	-75.
Dislocation	101	13.2300	42.7900	3.0000	150.0000	55.000	0.2805	1.0328	0.0014	0.008	0.	-80.
Dislocation	102	13.2800	42.6800	4.0000	150.0000	50.000	0.2962	1.0637	0.0007	0.0086	0.	-85.
Dislocation	103	13.2200	42.8000	2.0000	134.0000	47.000	0.2109	0.8847	-0.0016	0.0059	0.	-105.
Dislocation	104	13.2000	42.5800	15.0000	150.0000	70.000	0.3393	1.1450	0.0075	0.0063	0.	-40.0001
Dislocation	105	13.2600	42.8600	2.0000	100.0000	74.000	0.1944	0.8464	-0.0034	0.0045	0.	-127.
Dislocation	106	13.1300	42.7800	2.0000	150.0000	60.000	0.1892	0.8341	0.0005	0.0055	0.	-85.
Dislocation	107	13.1300	42.7800	2.0000	178.0000	61.000	0.5686	1.5150	-0.0017	0.0164	0.	-96.
Dislocation	108	13.1300	42.7800	2.0000	182.0000	56.000	0.4217	1.2882	-0.0021	0.0121	0.	-100.
Dislocation	109	13.1400	42.7800	1.0000	165.0000	55.000	0.3044	1.0794	0.	0.0088	0.	-90.
Dislocation	110	13.1400	42.7500	1.0000	170.0000	50.000	0.1607	0.7635	-0.0004	0.0046	0.	-95.
Dislocation	111	13.0900	42.7600	7.0000	43.0000	76.000	0.2351	0.9384	-0.0017	0.0066	0.	-104.
Dislocation	112	13.2300	42.8400	5.0000	120.0000	59.000	0.2844	1.0404	-0.0023	0.0079	0.	-106.
Dislocation	113	13.2900	42.6800	4.0000	145.0000	80.000	0.2517	0.9736	0.0047	0.0056	0.	-50.
Dislocation	114	13.2500	42.8200	2.0000	132.0000	71.000	0.2109	0.8847	-0.0045	0.0042	0.	-137.
Dislocation	115	16.4500	39.0400	17.0000	68.0000	69.000	0.3170	1.1036	-0.0021	0.009	0.	-103.
Dislocation	116	13.2900	42.6800	4.0000	135.0000	75.000	0.1816	0.8158	0.0026	0.0046	0.	-60.
Dislocation	117	13.2800	42.6700	4.0000	145.0000	65.000	0.5313	1.4602	0.0088	0.0126	0.	-55.
Dislocation	118	13.2900	42.6800	4.0000	145.0000	90.000	0.2805	1.0328	0.0028	-0.0077	0.	70.
Dislocation	119	13.1500	42.8100	6.0000	120.0000	75.000	0.1918	0.8402	0.0019	0.0052	0.	-70.
Dislocation	120	13.1500	42.8100	6.0000	130.0000	90.000	0.1918	0.8402	0.0019	0.0052	0.	-70.
Dislocation	121	13.1500	42.8000	5.0000	175.0000	90.000	0.3583	1.1792	0.0018	-0.0102	0.	80.
Dislocation	122	13.1300	42.7800	2.0000	140.0000	75.000	0.1607	0.7635	0.0004	0.0046	0.	-85.
Dislocation	123	13.1900	42.7600	5.0000	155.0000	60.000	0.4104	1.2694	0.0021	0.0117	0.	-80.
Dislocation	124	13.2500	42.9000	5.0000	175.0000	60.000	0.3681	1.1967	0.0028	0.0103	0.	-75.
Dislocation	125	13.2400	42.9000	5.0000	175.0000	60.000	0.4452	1.3268	0.0044	0.0121	0.	-70.
Dislocation	126	13.2300	42.7900	2.0000	140.0000	55.000	0.2962	1.0637	0.0015	0.0085	0.	-80.
Dislocation	127	13.1200	42.8600	5.0000	107.0000	54.000	0.3940	1.2416	-0.0069	0.0091	0.	-127.
Dislocation	128	13.2200	42.6400	7.0000	148.0000	61.000	0.2586	0.9881	-0.001	0.0074	0.	-98.
Dislocation	129	13.1400	42.8800	5.0000	149.0000	66.000	0.1697	0.7863	-0.0006	0.0049	0.	-97.
Dislocation	130	13.2500	42.9000	5.0000	160.0000	65.000	0.2922	1.0558	0.0022	0.0082	0.	-75.

Dislocation	131	13.2000	42.7800	6.0000	90.0000	65.000	0.1866	0.8279	0.0031	0.0044	0.	-55.
Dislocation	132	13.1800	42.7500	3.0000	148.0000	45.000	0.4701	1.3665	-0.0012	0.0136	0.	-95.
Dislocation	133	13.1900	42.7500	4.0000	148.0000	45.000	0.2517	0.9736	-0.0006	0.0073	0.	-95.
Dislocation	134	13.1900	42.7400	3.0000	151.0000	46.000	0.7360	1.7426	-0.0037	0.021	0.	-100.
Dislocation	135	13.2000	42.7400	3.0000	165.0000	70.000	0.2320	0.9315	0.0006	0.0067	0.	-85.
Dislocation	136	13.2000	42.7400	3.0000	160.0000	60.000	0.4217	1.2882	0.0011	0.0122	0.	-85.
Dislocation	137	13.2500	42.8600	1.0000	115.0000	53.000	0.1629	0.7691	-0.0013	0.0045	0.	-106.
Dislocation	138	13.0700	42.8700	5.0000	145.0000	55.000	0.2586	0.9881	0.0026	0.0071	0.	-70.
Dislocation	139	13.3300	42.6300	5.0000	152.0000	51.000	0.3170	1.1036	-0.0013	0.0091	0.	-98.
Dislocation	140	13.2600	42.8900	3.0000	145.0000	60.000	0.2517	0.9736	0.0042	0.006	0.	-55.
Dislocation	141	13.1800	42.7500	3.0000	180.0000	60.000	0.2257	0.9179	0.0022	0.0062	0.	-70.
Dislocation	142	13.1800	42.7500	3.0000	161.0000	46.000	0.7771	1.7947	-0.0039	0.0222	0.	-100.
Dislocation	143	13.1500	42.8500	5.0000	175.0000	70.000	0.2922	1.0558	0.0007	0.0085	0.	-85.
Dislocation	144	15.6500	40.7600	16.0000	150.0000	89.000	0.4160	1.2788	-0.0021	-0.0119	0.	100.
Dislocation	145	11.0500	43.1900	9.0000	37.0000	78.000	0.4392	1.3170	-0.0048	-0.0118	0.	112.
Dislocation	146	12.5500	43.3800	1.0000	145.0000	60.000	0.1918	0.8402	0.001	0.0055	0.	-80.
Dislocation	147	10.9900	43.6000	8.0000	82.0000	85.000	0.7667	1.7816	-0.0202	0.0094	0.	-155.
Dislocation	148	13.1300	42.8800	5.0000	154.0000	60.000	4.8641	4.8529	-0.0074	0.141	0.	-93.
Dislocation	149	13.0900	42.8800	6.0000	159.0000	66.000	0.3214	1.1117	-0.0011	0.0093	0.	-97.
Dislocation	150	13.1200	42.9100	5.0000	144.0000	47.000	0.3347	1.1366	-0.0025	0.0094	0.	-105.
Dislocation	151	13.1300	42.8900	5.0000	170.0000	60.000	0.2257	0.9179	0.0017	0.0063	0.	-75.
Dislocation	152	13.1300	42.9100	5.0000	162.0000	45.000	10.5511	7.3858	0.0267	0.3052	0.	-85.
Dislocation	153	13.0700	42.8900	6.0000	175.0000	75.000	0.6971	1.6920	0.0116	-0.0166	0.	55.
Dislocation	154	13.0800	42.8700	5.0000	149.0000	66.000	0.5764	1.5262	-0.002	0.0166	0.	-97.
Dislocation	155	13.2600	42.8200	4.0000	134.0000	79.000	0.2138	0.8913	-0.0043	-0.0045	0.	134.
Dislocation	156	13.1300	42.8600	5.0000	150.0000	60.000	1.5966	2.6522	0.	0.0464	0.	-90.
Dislocation	157	13.2100	42.8600	4.0000	163.0000	78.000	0.3258	1.1200	-0.0035	0.0088	0.	-112.
Dislocation	158	13.1600	42.9300	2.0000	137.0000	84.000	0.2586	0.9881	-0.0043	-0.0061	0.	125.
Dislocation	159	13.1200	42.8700	5.0000	186.0000	60.000	0.2768	1.0252	0.0004	0.008	0.	-87.
Dislocation	160	13.1700	42.8400	3.0000	150.0000	60.000	0.3887	1.2325	0.0039	0.0106	0.	-70.
Dislocation	161	13.1700	42.8400	2.0000	175.0000	60.000	0.2227	0.9112	0.0046	0.0046	0.	-45.
Dislocation	162	13.1200	42.9900	2.0000	146.0000	55.000	0.3044	1.0794	0.0005	0.0088	0.	-87.
Dislocation	163	13.0600	42.8900	7.0000	130.0000	55.000	0.2693	1.0102	-0.0039	0.0068	0.	-120.
Dislocation	164	13.1500	42.8400	5.0000	159.0000	60.000	0.7878	1.8080	-0.0012	0.0228	0.	-93.
Dislocation	165	13.1300	42.9900	3.0000	170.0000	70.000	0.9528	2.0045	0.0048	0.0272	0.	-80.
Dislocation	166	13.1300	42.8700	3.0000	161.0000	73.000	0.2883	1.0481	-0.0035	0.0076	0.	-115.
Dislocation	167	13.1000	42.8700	5.0000	168.0000	61.000	1.2847	2.3572	-0.0039	0.0371	0.	-96.
Dislocation	168	13.1500	42.9600	1.0000	160.0000	80.000	0.2167	0.8978	0.0044	0.0044	0.	-45.
Dislocation	169	13.1300	43.0200	1.0000	135.0000	59.000	0.3128	1.0955	-0.0025	0.0087	0.	-106.
Dislocation	170	13.1400	43.0200	1.0000	128.0000	66.000	0.2288	0.9247	-0.0036	0.0056	0.	-123.
Dislocation	171	13.1600	42.7900	5.0000	173.0000	61.000	0.2883	1.0481	-0.0009	0.0083	0.	-96.
Dislocation	172	13.0700	42.9500	7.0000	144.0000	66.000	0.2551	0.9808	-0.0032	0.0067	0.	-116.
Dislocation	173	13.1000	42.8400	5.0000	175.0000	70.000	1.1841	2.2553	-0.0012	0.0344	0.	-92.
Dislocation	174	13.1100	42.8500	5.0000	175.0000	65.000	0.6784	1.6673	0.	0.0197	0.	-90.
Dislocation	175	13.1200	43.0100	2.0000	170.0000	50.000	0.3214	1.1117	0.0039	0.0085	0.	-65.
Dislocation	176	13.1500	42.8700	3.0000	107.0000	62.000	0.2351	0.9384	-0.0052	0.0045	0.	-139.
Dislocation	177	13.1200	42.8200	5.0000	156.0000	57.000	0.2962	1.0637	-0.0019	0.0084	0.	-103.
Dislocation	178	13.1400	42.9900	2.0000	140.0000	55.000	0.2922	1.0558	0.	0.0085	0.	-90.
Dislocation	179	13.1200	43.0300	2.0000	121.0000	64.000	0.3170	1.1036	-0.0076	0.0051	0.	-146.
Dislocation	180	13.1500	42.9900	2.0000	130.0000	53.000	0.2883	1.0481	-0.0023	0.008	0.	-106.
Dislocation	181	13.1400	43.0000	2.0000	145.0000	50.000	0.2621	0.9954	0.0007	0.0076	0.	-85.
Dislocation	182	13.0400	42.8600	8.0000	130.0000	67.000	0.2730	1.0177	-0.0057	0.0055	0.	-136.
Dislocation	183	13.1800	42.8900	2.0000	150.0000	50.000	0.2320	0.9315	0.0012	0.0066	0.	-80.
Dislocation	184	13.1400	42.9600	3.0000	106.0000	66.000	0.2257	0.9179	-0.0041	0.0051	0.	-129.
Dislocation	185	13.1100	42.9200	5.0000	155.0000	55.000	0.3170	1.1036	0.0046	0.008	0.	-60.
Dislocation	186	13.2100	42.8700	1.0000	150.0000	55.000	0.3440	1.1535	0.0009	0.0099	0.	-85.
Dislocation	187	13.1200	42.7900	8.0000	160.0000	75.000	0.5032	1.4178	0.0112	0.0094	0.	-40.0001
Dislocation	188	13.1600	42.8700	5.0000	180.0000	75.000	0.5385	1.4710	0.0027	0.0154	0.	-80.
Dislocation	189	13.1400	42.8000	5.0000	158.0000	61.000	0.2730	1.0177	-0.0011	0.0078	0.	-98.
Dislocation	190	13.0900	42.8800	6.0000	148.0000	67.000	0.3534	1.1706	-0.0016	0.0101	0.	-99.
Dislocation	191	13.0500	42.9900	6.0000	136.0000	66.000	0.3487	1.1620	-0.0031	0.0096	0.	-108.
Dislocation	192	13.1500	42.8500	3.0000	205.0000	85.000	0.3258	1.1200	0.0032	-0.0089	0.	70.
Dislocation	193	13.1000	43.0200	3.0000	123.0000	68.000	0.2138	0.8913	-0.0036	0.0051	0.	-125.
Dislocation	194	13.2000	42.8800	1.0000	145.0000	55.000	0.2383	0.9454	0.	0.0069	0.	-90.
Dislocation	195	13.1000	42.8100	7.0000	150.0000	50.000	0.9273	1.9751	0.	0.0269	0.	-90.
Dislocation	196	13.0800	42.9600	5.0000	134.0000	66.000	0.2517	0.9736	-0.0032	0.0066	0.	-116.
Dislocation	197	13.1000	42.8300	5.0000	173.0000	61.000	0.2844	1.0404	-0.0009	0.0082	0.	-96.
Dislocation	198	13.0700	43.0600	5.0000	160.0000	65.000	0.3044	1.0794	0.0037	0.008	0.	-65.
Dislocation	199	13.1100	42.8400	2.0000	150.0000	55.000	19.7106	10.3657	0.	0.5722	0.	-90.
Dislocation	200	13.0500	42.8600	8.0000	165.0000	90.000	0.5843	1.5374	0.0097	0.0139	0.	-55.
Dislocation	201	13.0800	42.8300	8.0000	185.0000	75.000	1.1681	2.2387	0.0059	0.0334	0.	-80.
Dislocation	202	13.1900	42.8800	2.0000	128.0000	51.000	0.5100	1.4282	-0.0083	0.0123	0.	-124.
Dislocation	203	13.2200	42.7100	7.0000	155.0000	55.000	0.3834	1.2235	0.0064	0.0091	0.	-55.
Dislocation	204	13.2100	42.9300	4.0000	90.0000	57.000	0.3534	1.1706	-0.0056	-0.0086	0.	123.
Dislocation	205	13.1100	42.8600	3.0000	165.0000	80.000	0.3534	1.1706	0.0084	-0.0059	0.	35.
Dislocation	206	13.1200	42.8400	5.0000	170.0000	65.000	0.4104	1.2694	0.0021	0.0117	0.	-80.
Dislocation	207	13.2000	42.9400	2.0000	170.0000	50.000	0.4897	1.3970	0.006	0.0129	0.	-65.
Dislocation	208	13.0700	42.8400	7.0000	155.0000	75.000	0.4765	1.3766	0.	0.0138	0.	-90.

Dislocation	209	12.2400	44.1800	10.0000	68.0000	80.000	0.5241	1.4494	-0.0071	-0.0134	0.	118.
Dislocation	210	13.0800	42.7800	7.0000	173.0000	74.000	0.5922	1.5488	-0.0036	0.0168	0.	-102.
Dislocation	211	13.0900	42.8200	6.0000	148.0000	67.000	0.4333	1.3074	-0.002	0.0124	0.	-99.
Dislocation	212	13.1900	42.9200	2.0000	118.0000	51.000	0.4701	1.3665	-0.0076	0.0113	0.	-124.
Dislocation	213	13.1900	42.8000	7.0000	165.0000	65.000	0.4392	1.3170	0.0022	0.0126	0.	-80.
Dislocation	214	13.1900	42.8000	7.0000	165.0000	65.000	0.4392	1.3170	0.0022	0.0126	0.	-80.
Dislocation	215	13.0700	43.0600	5.0000	160.0000	60.000	0.8095	1.8348	0.008	0.0221	0.	-70.
Dislocation	216	13.1200	42.8500	9.0000	125.0000	68.000	0.2883	1.0481	-0.0039	0.0074	0.	-118.
Dislocation	217	13.1400	42.8900	5.0000	145.0000	55.000	0.4049	1.2601	0.003	0.0114	0.	-75.
Dislocation	218	13.0600	42.8400	9.0000	160.0000	90.000	0.8782	1.9178	0.0022	0.0254	0.	-85.
Dislocation	219	13.0800	42.8400	6.0000	150.0000	75.000	1.6406	2.6915	-0.0008	0.0476	0.	-91.
Dislocation	220	13.2000	42.9300	2.0000	165.0000	55.000	0.5241	1.4494	0.0076	0.0132	0.	-60.
Dislocation	221	13.2000	42.9300	2.0000	165.0000	55.000	0.5241	1.4494	0.0076	0.0132	0.	-60.
Dislocation	222	13.1400	42.8500	3.0000	170.0000	75.000	0.3258	1.1200	-0.0002	0.0095	0.	-91.
Dislocation	223	13.1500	42.9200	2.0000	126.0000	52.000	0.3302	1.1282	-0.0044	0.0085	0.	-117.
Dislocation	224	13.1900	42.9200	4.0000	83.0000	74.000	0.2351	0.9384	-0.0055	-0.0041	0.	142.9999
Dislocation	225	13.2000	42.9100	2.0000	165.0000	50.000	0.2768	1.0252	0.0034	0.0073	0.	-65.
Dislocation	226	13.1900	42.7300	2.0000	149.0000	66.000	0.2449	0.9594	-0.0031	0.0064	0.	-116.
Dislocation	227	13.2000	42.9000	2.0000	158.0000	50.000	0.3044	1.0794	-0.0006	0.0088	0.	-94.
Dislocation	228	13.1500	42.7300	6.0000	153.0000	45.000	0.3085	1.0874	-0.0008	0.0089	0.	-95.
Dislocation	229	13.0600	42.7700	7.0000	134.0000	54.000	0.3393	1.1450	-0.0034	0.0093	0.	-110.
Dislocation	230	13.2000	42.8100	7.0000	170.0000	70.000	0.2621	0.9954	-0.0003	0.0076	0.	-92.
Dislocation	231	13.1200	43.0200	1.0000	155.0000	45.000	0.3940	1.2416	0.	0.0114	0.	-90.
Dislocation	232	13.1200	43.0100	4.0000	119.0000	81.000	0.3044	1.0794	-0.0018	0.0086	0.	-102.
Dislocation	233	13.1600	42.8000	6.0000	155.0000	75.000	0.9399	1.9898	0.0175	0.0209	0.	-50.
Dislocation	234	13.2200	42.9000	4.0000	188.0000	69.000	0.3258	1.1200	-0.008	0.005	0.	-147.9999
Dislocation	235	13.2000	42.9100	1.0000	112.0000	61.000	0.2320	0.9315	-0.0032	0.0059	0.	-118.
Dislocation	236	13.2100	42.9400	1.0000	158.0000	56.000	0.4452	1.3268	-0.0016	0.0128	0.	-97.
Dislocation	237	13.0700	42.7900	7.0000	149.0000	71.000	0.2922	1.0558	-0.0007	0.0085	0.	-95.
Dislocation	238	13.2000	42.9100	2.0000	151.0000	46.000	0.3994	1.2508	-0.002	0.0114	0.	-100.
Dislocation	239	13.0900	42.7800	7.0000	165.0000	75.000	0.5922	1.5488	0.0009	-0.0172	0.	87.
Dislocation	240	13.2100	42.6800	5.0000	161.0000	69.000	0.2383	0.9454	-0.0026	0.0064	0.	-112.
Dislocation	241	13.0600	42.7600	6.0000	180.0000	88.000	0.3632	1.1880	-0.0018	0.0104	0.	-100.
Dislocation	242	13.1600	42.9000	2.0000	155.0000	60.000	0.4831	1.3868	0.0059	0.0127	0.	-65.
Dislocation	243	13.2100	42.9300	3.0000	185.0000	85.000	0.2138	0.8913	0.0051	0.0036	0.	-35.
Dislocation	244	13.1900	42.6900	7.0000	167.0000	71.000	0.2483	0.9665	-0.0021	0.0069	0.	-107.
Dislocation	245	13.2000	42.9400	2.0000	165.0000	65.000	0.2922	1.0558	0.0015	0.0084	0.	-80.
Dislocation	246	13.2000	42.9300	2.0000	132.0000	50.000	0.2586	0.9881	-0.0029	0.0069	0.	-113.
Dislocation	247	13.0400	42.8400	7.0000	163.0000	67.000	0.2197	0.9045	-0.0012	0.0063	0.	-101.
Dislocation	248	13.1400	42.8000	6.0000	168.0000	56.000	0.3085	1.0874	-0.0011	0.0089	0.	-97.
Dislocation	249	13.2000	42.7700	3.0000	155.0000	50.000	0.1971	0.8527	0.0024	0.0052	0.	-65.
Dislocation	250	13.1000	42.8600	8.0000	40.0000	55.000	0.1998	0.8590	0.0037	0.0044	0.	-50.
Dislocation	251	13.0700	43.0600	5.0000	160.0000	55.000	0.4765	1.3766	0.0047	0.013	0.	-70.
Dislocation	252	13.1600	42.8200	6.0000	141.0000	86.000	0.2288	0.9247	-0.0028	-0.006	0.	115.
Dislocation	253	13.1700	42.7800	5.0000	83.0000	74.000	0.2053	0.8718	-0.0012	0.0058	0.	-102.
Dislocation	254	13.0500	42.8300	6.0000	150.0000	70.000	0.2730	1.0177	0.	0.0079	0.	-90.
Dislocation	255	13.2100	42.9200	3.0000	116.0000	58.000	0.1866	0.8279	-0.004	0.0036	0.	-137.9999
Dislocation	256	13.0700	43.0700	5.0000	160.0000	60.000	0.2621	0.9954	0.002	0.0074	0.	-75.
Dislocation	257	13.1000	42.8100	7.0000	107.0000	66.000	0.2109	0.8847	-0.0048	-0.0039	0.	141.0001
Dislocation	258	13.0700	42.8700	7.0000	126.0000	63.000	0.2449	0.9594	-0.0043	0.0057	0.	-127.
Dislocation	259	13.1600	42.8900	2.0000	128.0000	48.000	0.3887	1.2325	-0.0037	0.0107	0.	-109.
Dislocation	260	13.1800	42.9500	4.0000	170.0000	75.000	0.2197	0.9045	0.0052	-0.0037	0.	35.
Dislocation	261	13.1400	42.9100	6.0000	175.0000	50.000	0.4638	1.3564	0.0067	0.0117	0.	-60.
Dislocation	262	13.2100	42.8800	2.0000	130.0000	71.000	0.2621	0.9954	-0.0038	0.0066	0.	-120.
Dislocation	263	13.2100	42.9200	1.0000	145.0000	53.000	0.1607	0.7635	-0.0013	0.0045	0.	-106.
Dislocation	264	13.1500	42.7900	1.0000	175.0000	45.000	0.6784	1.6673	0.	0.0197	0.	-90.
Dislocation	265	13.1000	42.8100	5.0000	145.0000	70.000	0.3681	1.1967	0.0004	0.0107	0.	-88.
Dislocation	266	13.1500	42.8000	1.0000	166.0000	46.000	0.2288	0.9247	-0.0012	0.0065	0.	-100.
Dislocation	267	13.0900	42.8100	8.0000	155.0000	70.000	0.2109	0.8847	0.0031	-0.0053	0.	60.
Dislocation	268	13.2000	42.9300	4.0000	94.0000	67.000	0.3170	1.1036	-0.0082	-0.0042	0.	153.
Dislocation	269	13.1400	42.9400	6.0000	146.0000	57.000	0.3085	1.0874	-0.002	0.0087	0.	-103.
Dislocation	270	13.1600	42.8000	1.0000	177.0000	45.000	0.1652	0.7748	0.0004	0.0048	0.	-85.
Dislocation	271	13.1600	42.9100	1.0000	150.0000	50.000	0.3170	1.1036	0.0016	0.0091	0.	-80.
Dislocation	272	13.2000	42.9000	4.0000	110.0000	73.000	0.2320	0.9315	-0.0057	-0.0036	0.	147.9999
Dislocation	273	13.1900	42.8100	7.0000	175.0000	70.000	0.3732	1.2056	0.0037	0.0102	0.	-70.
Dislocation	274	13.2100	42.9200	4.0000	200.0000	65.000	0.2768	1.0252	0.0066	-0.0046	0.	35.
Dislocation	275	13.0500	42.9100	7.0000	120.0000	55.000	0.3258	1.1200	-0.0047	0.0082	0.	-120.
Dislocation	276	13.1800	42.7200	1.0000	165.0000	85.000	0.1841	0.8219	-0.0053	0.0005	0.	-175.
Dislocation	277	13.1200	42.7800	7.0000	159.0000	79.000	0.3887	1.2325	-0.0022	0.0111	0.	-101.
Dislocation	278	13.0900	42.8300	4.0000	147.0000	69.000	0.4452	1.3268	-0.011	-0.0068	0.	147.9999
Dislocation	279	13.1000	42.7800	7.0000	160.0000	85.000	0.2805	1.0328	0.0058	0.0058	0.	-45.
Dislocation	280	13.1900	42.7500	4.0000	116.0000	82.000	0.2081	0.8782	-0.0049	0.0035	0.	-145.
Dislocation	281	13.1900	42.7300	2.0000	175.0000	50.000	0.1744	0.7980	0.0017	0.0048	0.	-70.
Dislocation	282	13.1300	42.7500	7.0000	148.0000	74.000	0.3393	1.1450	-0.002	0.0096	0.	-102.
Dislocation	283	13.1300	42.7500	7.0000	148.0000	74.000	0.3393	1.1450	-0.002	0.0096	0.	-102.
Dislocation	284	13.1000	42.8000	7.0000	188.0000	67.000	0.2768	1.0252	-0.0013	0.0079	0.	-99.
Dislocation	285	13.1100	42.9900	2.0000	145.0000	65.000	0.1674	0.7805	0.0017	0.0046	0.	-70.
Dislocation	286	13.0400	42.7900	6.0000	155.0000	90.000	0.3534	1.1706	0.0027	0.0099	0.	-75.

Dislocation	287	13.1800	42.7400	6.0000	125.0000	60.000	0.2081	0.8782	0.003	0.0052	0.	-60.
Dislocation	288	13.1500	42.9000	2.0000	160.0000	60.000	0.3681	1.1967	0.0045	0.0097	0.	-65.
Dislocation	289	13.1200	42.7800	11.0000	91.0000	78.000	0.2483	0.9665	-0.0058	-0.0042	0.	144.
Dislocation	290	13.1100	42.7800	7.0000	145.0000	85.000	0.1971	0.8527	0.0024	0.0052	0.	-65.
Dislocation	291	13.0700	43.0700	5.0000	165.0000	60.000	0.4513	1.3366	0.0045	0.0123	0.	-70.
Dislocation	292	13.3000	42.6200	5.0000	160.0000	65.000	0.3994	1.2508	0.001	0.0116	0.	-85.
Dislocation	293	13.0500	42.8400	5.0000	72.0000	80.000	0.2693	1.0102	-0.0076	-0.002	0.	165.
Dislocation	294	13.0900	42.7700	7.0000	174.0000	84.000	0.8664	1.9037	-0.0061	0.0244	0.	-104.
Dislocation	295	13.1900	42.9500	2.0000	101.0000	58.000	0.4897	1.3970	-0.0106	0.0095	0.	-137.9999
Dislocation	296	13.1900	42.7200	4.0000	163.0000	50.000	0.1998	0.8590	-0.0004	0.0058	0.	-94.
Dislocation	297	13.1400	42.9400	7.0000	143.0000	66.000	0.2320	0.9315	-0.0037	0.0056	0.	-123.
Dislocation	298	13.1900	42.8900	2.0000	150.0000	50.000	0.2922	1.0558	0.0015	0.0084	0.	-80.
Dislocation	299	13.0600	42.8400	7.0000	160.0000	60.000	0.3583	1.1792	0.	0.0104	0.	-90.
Dislocation	300	13.0700	42.7900	6.0000	147.0000	70.000	0.2844	1.0404	-0.0021	0.008	0.	-105.
Dislocation	301	13.2100	42.7700	3.0000	132.0000	51.000	0.2517	0.9736	-0.001	0.0072	0.	-98.
Dislocation	302	13.2100	42.7700	5.0000	129.0000	47.000	0.5843	1.5374	-0.0044	0.0164	0.	-105.
Dislocation	303	13.1300	42.8400	5.0000	175.0000	70.000	0.8095	1.8348	0.002	0.0234	0.	-85.
Dislocation	304	13.0800	43.0200	5.0000	165.0000	55.000	0.3887	1.2325	0.0048	0.0102	0.	-65.
Dislocation	305	13.1400	42.8100	5.0000	148.0000	61.000	0.3783	1.2145	-0.0011	0.0109	0.	-96.
Dislocation	306	13.1900	42.8100	7.0000	165.0000	75.000	0.2922	1.0558	0.0036	0.0077	0.	-65.
Dislocation	307	13.1500	42.8200	7.0000	146.0000	66.000	0.4104	1.2694	-0.0075	0.0093	0.	-129.
Dislocation	308	13.1100	42.9100	8.0000	109.0000	86.000	0.1866	0.8279	-0.0038	0.0038	0.	-135.
Dislocation	309	13.2100	42.9000	2.0000	200.0000	50.000	0.1792	0.8098	0.0026	0.0045	0.	-60.
Dislocation	310	13.0800	42.7700	7.0000	99.0000	87.000	0.2351	0.9384	-0.0044	0.0052	0.	-130.
Dislocation	311	13.2700	42.6900	7.0000	160.0000	80.000	0.2320	0.9315	0.0012	0.0066	0.	-80.
Dislocation	312	13.2200	42.9200	2.0000	165.0000	50.000	0.2551	0.9808	0.0019	0.0072	0.	-75.
Dislocation	313	13.1300	43.0600	2.0000	131.0000	63.000	0.1918	0.8402	-0.0034	0.0044	0.	-127.
Dislocation	314	13.1400	42.7500	8.0000	143.0000	86.000	0.2517	0.9736	-0.006	0.0042	0.	-145.
Dislocation	315	13.1400	42.9000	5.0000	150.0000	55.000	0.3214	1.1117	0.0024	0.009	0.	-75.
Dislocation	316	13.0500	42.7700	6.0000	160.0000	75.000	0.2730	1.0177	0.0021	-0.0077	0.	75.
Dislocation	317	13.2000	42.9500	2.0000	150.0000	50.000	0.2883	1.0481	0.0015	0.0082	0.	-80.
Dislocation	318	13.1500	42.7400	1.0000	215.0000	65.000	0.2081	0.8782	0.0026	0.0055	0.	-65.
Dislocation	319	13.2100	42.9400	2.0000	125.0000	68.000	0.2351	0.9384	-0.0032	0.006	0.	-118.
Dislocation	320	13.1800	42.8900	4.0000	85.0000	73.000	0.2167	0.8978	-0.0053	-0.0033	0.	147.9999
Dislocation	321	13.0500	42.8100	7.0000	106.0000	73.000	0.2844	1.0404	-0.0035	0.0075	0.	-115.
Dislocation	322	13.2000	42.9500	1.0000	160.0000	50.000	0.2551	0.9808	0.0019	0.0072	0.	-75.
Dislocation	323	13.0800	42.8500	8.0000	151.0000	73.000	0.2257	0.9179	-0.0028	0.0059	0.	-115.
Dislocation	324	13.0600	42.9300	6.0000	146.0000	73.000	0.2167	0.8978	-0.0027	0.0057	0.	-115.
Dislocation	325	13.2200	42.6600	7.0000	134.0000	54.000	0.2922	1.0558	-0.0029	0.008	0.	-110.
Dislocation	326	13.0300	42.7700	7.0000	145.0000	90.000	0.1720	0.7921	-0.0021	0.0045	0.	-115.
Dislocation	327	13.3100	42.9100	17.0000	105.0000	68.000	0.4160	1.2788	-0.0057	0.0107	0.	-118.
Dislocation	328	13.1400	42.7800	6.0000	146.0000	46.000	0.2053	0.8718	-0.001	0.0059	0.	-100.
Dislocation	329	13.1400	43.0100	1.0000	147.0000	51.000	0.3302	1.1282	-0.0013	0.0095	0.	-98.
Dislocation	330	13.1400	43.0100	1.0000	146.0000	46.000	0.2621	0.9954	-0.0013	0.0075	0.	-100.
Dislocation	331	13.1600	43.0000	7.0000	110.0000	81.000	1.8793	2.8973	-0.0473	0.0273	0.	-150.
Dislocation	332	11.0100	43.6100	9.0000	180.0000	70.000	0.3085	1.0874	0.0078	-0.0045	0.	30.
Dislocation	333	13.2100	42.7300	5.0000	155.0000	60.000	0.2586	0.9881	0.0032	0.0068	0.	-65.
Dislocation	334	13.1500	42.6900	9.0000	110.0000	70.000	0.2288	0.9247	-0.0052	-0.0041	0.	142.
Dislocation	335	13.1600	42.9000	3.0000	113.0000	57.000	0.1998	0.8590	-0.0037	0.0044	0.	-130.
Dislocation	336	13.1700	42.9100	1.0000	138.0000	45.000	0.3632	1.1880	-0.0009	0.0105	0.	-95.
Dislocation	337	13.1100	42.8000	11.0000	106.0000	77.000	0.2730	1.0177	-0.0049	0.0062	0.	-128.
Dislocation	338	13.2100	42.9300	2.0000	155.0000	45.000	0.3128	1.0955	0.	0.0091	0.	-90.
Dislocation	339	13.1000	42.8000	7.0000	150.0000	55.000	0.2768	1.0252	0.0034	0.0073	0.	-65.
Dislocation	340	13.1300	42.8100	8.0000	130.0000	75.000	0.3440	1.1535	0.0042	0.0091	0.	-65.
Dislocation	341	13.2200	42.7300	6.0000	137.0000	73.000	0.3302	1.1282	-0.003	0.0091	0.	-108.
Dislocation	342	13.0300	42.8000	7.0000	155.0000	80.000	0.5313	1.4602	0.0027	0.0152	0.	-80.
Dislocation	343	13.1300	42.9100	5.0000	142.0000	69.000	0.1971	0.8527	-0.0038	0.0043	0.	-131.
Dislocation	344	13.0600	43.0400	6.0000	136.0000	66.000	0.1918	0.8402	-0.0017	0.0053	0.	-108.
Dislocation	345	13.0800	42.7800	6.0000	144.0000	85.000	0.2621	0.9954	-0.0038	0.0066	0.	-120.
Dislocation	346	13.0600	43.0300	6.0000	145.0000	65.000	0.3347	1.1366	0.	0.0097	0.	-90.
Dislocation	347	13.1700	42.8000	6.0000	111.0000	63.000	0.2922	1.0558	-0.0051	0.0068	0.	-127.
Dislocation	348	13.1900	42.7100	5.0000	55.0000	60.000	0.2551	0.9808	0.0057	0.0048	0.	-40.0001
Dislocation	349	13.1500	43.0000	1.0000	152.0000	45.000	0.2109	0.8847	0.0005	0.0061	0.	-85.
Dislocation	350	13.2100	42.7800	3.0000	150.0000	60.000	0.2416	0.9524	0.0035	0.0061	0.	-60.
Dislocation	351	13.1500	42.8800	7.0000	148.0000	56.000	0.2730	1.0177	-0.0031	0.0073	0.	-113.
Dislocation	352	13.1500	42.8000	7.0000	59.0000	83.000	0.1629	0.7691	-0.0015	0.0045	0.	-109.
Dislocation	353	13.0400	43.0300	6.0000	160.0000	65.000	0.3044	1.0794	0.0015	0.0087	0.	-80.
Dislocation	354	13.1500	42.8900	5.0000	152.0000	48.000	0.2197	0.9045	0.0021	0.006	0.	-71.
Dislocation	355	13.2100	42.9300	2.0000	195.0000	75.000	0.2483	0.9665	0.0068	-0.0025	0.	20.
Dislocation	356	13.1500	42.9400	5.0000	148.0000	61.000	0.3085	1.0874	-0.0012	0.0089	0.	-98.
Dislocation	357	13.0700	42.8800	1.0000	142.0000	51.000	0.4897	1.3970	-0.002	0.0141	0.	-98.
Dislocation	358	13.2000	42.9000	2.0000	97.0000	86.000	0.1522	0.7413	-0.0038	-0.0022	0.	150.
Dislocation	359	13.1900	42.8800	2.0000	134.0000	47.000	0.3170	1.1036	-0.0024	0.0089	0.	-105.
Dislocation	360	13.0600	43.0400	5.0000	160.0000	55.000	0.2320	0.9315	0.0023	0.0063	0.	-70.
Dislocation	361	13.0600	43.0400	5.0000	160.0000	55.000	0.2320	0.9315	0.0023	0.0063	0.	-70.
Dislocation	362	13.0500	43.0300	5.0000	144.0000	71.000	2.1237	3.0960	-0.0054	0.0614	0.	-95.
Dislocation	363	13.0700	42.8600	9.0000	185.0000	60.000	0.1720	0.7921	0.0009	0.0049	0.	-80.
Dislocation	364	13.3100	42.6600	2.0000	154.0000	65.000	0.2288	0.9247	-0.0006	0.0066	0.	-95.

Dislocation	365	13.0600	43.0200	5.0000	145.0000	70.000	0.2025	0.8654	0.	0.0059	0.	-90.
Dislocation	366	13.1500	42.9700	5.0000	155.0000	55.000	0.2805	1.0328	0.0047	0.0067	0.	-55.
Dislocation	367	13.1200	42.8300	6.0000	150.0000	55.000	0.3440	1.1535	0.	0.01	0.	-90.
Dislocation	368	13.2100	42.7800	4.0000	188.0000	67.000	0.2416	0.9524	-0.0013	0.0069	0.	-101.
Dislocation	369	13.2200	42.9100	2.0000	143.0000	57.000	0.3487	1.1620	-0.0065	0.0078	0.	-130.
Dislocation	370	13.2000	42.9200	2.0000	180.0000	55.000	0.2844	1.0404	0.0041	0.0072	0.	-60.
Dislocation	371	13.1800	42.6900	9.0000	147.0000	56.000	0.5764	1.5262	-0.0029	0.0165	0.	-100.
Dislocation	372	13.0800	42.9900	5.0000	153.0000	69.000	0.3534	1.1706	-0.0023	0.01	0.	-103.
Dislocation	373	13.0600	43.0300	6.0000	137.0000	56.000	0.2483	0.9665	-0.0013	0.0071	0.	-100.
Dislocation	374	13.0500	43.0200	5.0000	158.0000	77.000	0.2320	0.9315	-0.0019	0.0065	0.	-106.
Dislocation	375	13.1100	42.7900	7.0000	184.0000	84.000	0.2449	0.9594	-0.0029	0.0065	0.	-114.
Dislocation	376	13.0500	42.7600	7.0000	130.0000	53.000	0.2517	0.9736	-0.002	0.007	0.	-106.
Dislocation	377	13.1000	42.8700	7.0000	133.0000	61.000	0.1944	0.8464	-0.0038	0.0042	0.	-132.
Dislocation	378	13.0700	42.8700	7.0000	149.0000	66.000	0.2883	1.0481	-0.001	0.0083	0.	-97.
Dislocation	379	13.2100	42.6800	9.0000	127.0000	54.000	0.2768	1.0252	-0.0048	0.0064	0.	-127.
Dislocation	380	13.1600	42.9000	2.0000	140.0000	60.000	0.1971	0.8527	0.	0.0057	0.	-90.
Dislocation	381	13.1400	42.7800	6.0000	143.0000	56.000	0.2167	0.8978	-0.0008	0.0062	0.	-97.
Dislocation	382	13.0700	43.0100	5.0000	152.0000	45.000	0.2138	0.8913	0.0005	0.0062	0.	-85.
Dislocation	383	13.1300	42.8700	3.0000	102.0000	54.000	0.2517	0.9736	-0.0044	0.0058	0.	-127.
Dislocation	384	13.1300	42.9800	3.0000	190.0000	65.000	0.1697	0.7863	0.0043	0.0025	0.	-30.
Dislocation	385	13.1300	42.7900	6.0000	152.0000	56.000	0.3347	1.1366	0.0012	0.0096	0.	-83.
Dislocation	386	13.2300	42.8300	11.0000	135.0000	75.000	0.2320	0.9315	0.0043	0.0052	0.	-50.
Dislocation	387	13.1300	42.8800	3.0000	175.0000	65.000	0.1720	0.7921	0.0009	0.0049	0.	-80.
Dislocation	388	13.0600	43.0600	5.0000	141.0000	52.000	0.1944	0.8464	-0.0012	0.0055	0.	-102.
Dislocation	389	13.1500	42.7000	8.0000	145.0000	80.000	0.2483	0.9665	0.0013	0.0071	0.	-80.
Dislocation	390	13.1800	42.6800	7.0000	128.0000	51.000	0.2053	0.8718	-0.0033	0.0049	0.	-124.
Dislocation	391	13.1900	42.9100	2.0000	129.0000	64.000	0.2483	0.9665	-0.0029	0.0066	0.	-114.
Dislocation	392	13.2100	42.9400	1.0000	170.0000	60.000	0.2693	1.0102	0.002	0.0076	0.	-75.
Dislocation	393	13.2300	42.9500	1.0000	155.0000	55.000	0.4765	1.3766	-0.0012	0.0138	0.	-95.
Dislocation	394	13.2200	42.9500	1.0000	155.0000	55.000	0.2483	0.9665	0.0019	0.007	0.	-75.
Dislocation	395	13.1800	42.7900	7.0000	102.0000	62.000	0.1971	0.8527	-0.0043	0.0038	0.	-139.
Dislocation	396	13.1300	42.9800	2.0000	147.0000	50.000	0.3302	1.1282	-0.0037	0.0088	0.	-113.
Dislocation	397	13.1900	42.7500	2.0000	159.0000	55.000	0.3258	1.1200	-0.0005	0.0094	0.	-93.
Dislocation	398	13.2000	42.9500	1.0000	155.0000	60.000	0.2922	1.0558	0.0029	0.008	0.	-70.
Dislocation	399	13.2200	42.9400	2.0000	175.0000	70.000	0.1792	0.8098	0.0018	0.0049	0.	-70.
Dislocation	400	13.1900	42.7300	5.0000	180.0000	50.000	0.3681	1.1967	0.0053	0.0093	0.	-60.
Dislocation	402	13.2100	42.9500	2.0000	120.0000	55.000	0.2351	0.9384	-0.0034	0.0059	0.	-120.
Dislocation	403	13.0600	43.0600	5.0000	131.0000	64.000	0.4964	1.4073	-0.004	0.0139	0.	-106.
Dislocation	404	13.2000	42.7800	4.0000	135.0000	65.000	0.2551	0.9808	0.0037	0.0064	0.	-60.
Dislocation	405	13.1900	42.8100	6.0000	140.0000	65.000	0.3732	1.2056	0.0028	0.0105	0.	-75.
Dislocation	406	13.1900	42.8800	2.0000	150.0000	50.000	0.2383	0.9454	0.0006	0.0069	0.	-85.
Dislocation	407	13.0800	42.8700	9.0000	197.0000	77.000	0.2768	1.0252	-0.0022	-0.0077	0.	106.
Dislocation	408	13.1400	43.0200	2.0000	152.0000	50.000	0.2962	1.0637	0.0006	0.0086	0.	-86.
Dislocation	409	13.1800	42.9000	1.0000	128.0000	50.000	0.1481	0.7305	-0.0003	0.0043	0.	-94.
Dislocation	410	13.1500	42.8900	9.0000	146.0000	64.000	0.5764	1.5262	-0.0046	0.0161	0.	-106.
Dislocation	411	13.1800	42.9000	2.0000	149.0000	66.000	0.2167	0.8978	-0.0028	0.0057	0.	-116.
Dislocation	412	13.0400	42.8300	7.0000	148.0000	73.000	0.2883	1.0481	-0.0015	0.0082	0.	-100.
Dislocation	413	12.7700	42.8100	7.0000	110.0000	70.000	0.3347	1.1366	0.0056	0.008	0.	-55.
Dislocation	414	13.2500	42.5500	3.0000	165.0000	55.000	0.2257	0.9179	0.	0.0066	0.	-90.
Dislocation	415	13.1500	43.0000	2.0000	160.0000	45.000	0.3583	1.1792	0.	0.0104	0.	-90.
Dislocation	416	13.1600	43.0000	2.0000	149.0000	54.000	0.2081	0.8782	-0.0021	0.0057	0.	-110.
Dislocation	417	13.1900	42.6600	9.0000	180.0000	50.000	0.4831	1.3868	0.007	0.0121	0.	-60.
Dislocation	418	13.1800	42.7300	9.0000	185.0000	55.000	0.3128	1.0955	0.0016	0.0089	0.	-80.
Dislocation	419	13.1300	42.8900	3.0000	179.0000	65.000	0.3887	1.2325	-0.0004	0.0113	0.	-92.
Dislocation	420	13.0500	42.7800	7.0000	135.0000	90.000	0.3393	1.1450	0.0017	0.0097	0.	-80.
Dislocation	421	13.1800	42.9000	2.0000	138.0000	56.000	0.1971	0.8527	-0.0007	0.0057	0.	-97.
Dislocation	422	13.1300	43.0000	2.0000	160.0000	50.000	0.5764	1.5262	0.0015	0.0167	0.	-85.
Dislocation	423	13.1400	42.9900	2.0000	165.0000	50.000	0.4513	1.3366	0.0023	0.0129	0.	-80.
Dislocation	424	13.2100	42.7200	5.0000	151.0000	46.000	0.9528	2.0045	-0.0048	0.0272	0.	-100.
Dislocation	425	13.2000	42.9400	1.0000	175.0000	60.000	0.1892	0.8341	0.0005	0.0055	0.	-85.
Dislocation	426	13.0700	43.0300	5.0000	165.0000	65.000	0.2081	0.8782	0.001	0.0059	0.	-80.
Dislocation	427	13.1400	42.8000	6.0000	175.0000	50.000	0.4392	1.3170	0.	0.0128	0.	-90.
Dislocation	428	13.2100	42.9200	3.0000	105.0000	76.000	0.2657	1.0028	-0.0072	0.0028	0.	-159.
Dislocation	429	13.1000	42.8200	8.0000	190.0000	65.000	0.2288	0.9247	0.0012	0.0065	0.	-80.
Dislocation	430	13.1000	42.8200	10.0000	143.0000	71.000	0.2197	0.9045	-0.006	-0.0023	0.	159.
Dislocation	431	13.2300	42.5500	3.0000	140.0000	60.000	0.2693	1.0102	-0.0025	0.0074	0.	-109.
Dislocation	432	13.0900	42.9500	6.0000	135.0000	55.000	0.2844	1.0404	-0.0041	0.0072	0.	-120.
Dislocation	433	13.1600	42.8600	8.0000	144.0000	64.000	0.7066	1.7045	-0.0083	0.0187	0.	-114.
Dislocation	434	13.0600	43.0100	5.0000	170.0000	60.000	0.2586	0.9881	0.0026	0.0071	0.	-70.
Dislocation	435	13.0600	42.9800	6.0000	155.0000	80.000	0.2621	0.9954	0.0004	0.0076	0.	-87.
Dislocation	436	13.1500	42.9400	9.0000	161.0000	52.000	0.5313	1.4602	-0.0032	0.0151	0.	-102.
Dislocation	437	13.0700	43.0300	3.0000	160.0000	55.000	0.2138	0.8913	0.0021	0.0058	0.	-70.
Dislocation	438	13.0800	43.0300	5.0000	141.0000	55.000	0.2844	1.0404	0.0004	0.0082	0.	-87.
Dislocation	439	13.2100	42.7500	5.0000	175.0000	50.000	0.2693	1.0102	0.	0.0078	0.	-90.
Dislocation	440	13.1100	43.0400	2.0000	99.0000	64.000	0.1792	0.8098	-0.0043	-0.0029	0.	146.
Dislocation	441	13.1300	42.8000	7.0000	125.0000	80.000	0.6339	1.6069	0.0048	0.0178	0.	-75.
Dislocation	442	13.1000	43.0300	2.0000	185.0000	85.000	0.1697	0.7863	0.004	0.0028	0.	-35.
Dislocation	443	13.2000	42.7700	10.0000	134.0000	76.000	0.3302	1.1282	-0.0065	0.007	0.	-133.

Dislocation	444	13.0700	43.0100	6.0000	145.0000	55.000	0.2883	1.0481	0.	0.0084	0.	-90.
Dislocation	445	13.1900	42.8600	4.0000	66.0000	72.000	0.2383	0.9454	-0.0062	-0.003	0.	154.
Dislocation	446	13.2200	42.6400	8.0000	180.0000	73.000	0.2962	1.0637	-0.0073	0.0046	0.	-147.9999
Dislocation	447	13.1600	42.9500	9.0000	168.0000	61.000	0.2657	1.0028	-0.0008	0.0077	0.	-96.
Dislocation	448	9.7900	44.4300	4.0000	143.0000	56.000	0.2730	1.0177	-0.001	0.0079	0.	-97.
Dislocation	449	13.0800	43.0100	5.0000	150.0000	55.000	0.2351	0.9384	0.0018	0.0066	0.	-75.
Dislocation	450	13.0800	43.0200	4.0000	135.0000	50.000	0.1971	0.8527	0.0005	0.0057	0.	-85.
Dislocation	451	13.1300	43.0100	2.0000	141.0000	46.000	0.1744	0.7980	-0.0009	0.005	0.	-100.
Dislocation	452	13.1200	42.8400	5.0000	154.0000	55.000	0.3994	1.2508	-0.0006	0.0116	0.	-93.
Dislocation	453	13.1500	42.9300	2.0000	170.0000	60.000	0.2657	1.0028	0.0055	0.0055	0.	-45.
Dislocation	454	13.1000	43.0500	3.0000	195.0000	90.000	0.1816	0.8158	0.0051	0.0014	0.	-15.
Dislocation	455	13.1000	43.0500	3.0000	190.0000	85.000	0.2621	0.9954	0.0075	-0.0013	0.	10.
Dislocation	456	13.2800	42.7200	10.0000	142.0000	76.000	0.2693	1.0102	-0.0028	0.0073	0.	-111.
Dislocation	457	13.0800	43.0200	5.0000	150.0000	55.000	0.2551	0.9808	0.0025	0.007	0.	-70.
Dislocation	458	13.1500	42.9900	2.0000	160.0000	55.000	0.1607	0.7635	0.0012	0.0045	0.	-75.
Dislocation	459	12.9400	42.8600	3.0000	80.0000	90.000	0.2483	0.9665	-0.0065	0.003	0.	-155.
Dislocation	460	13.2100	42.8000	5.0000	140.0000	55.000	0.3534	1.1706	0.0043	0.0093	0.	-65.
Dislocation	461	13.0700	43.0100	5.0000	155.0000	65.000	0.2517	0.9736	0.0019	0.0071	0.	-75.
Dislocation	462	13.0700	43.0100	3.0000	155.0000	55.000	0.2449	0.9594	0.0046	0.0054	0.	-50.
Dislocation	463	13.0800	43.0200	5.0000	145.0000	50.000	0.4765	1.3766	0.0047	0.013	0.	-70.
Dislocation	464	13.0800	43.0200	5.0000	143.0000	45.000	0.5241	1.4494	-0.0013	0.0152	0.	-95.
Dislocation	465	13.0700	43.0200	4.0000	154.0000	47.000	0.2197	0.9045	-0.0017	0.0062	0.	-105.
Dislocation	466	13.0700	43.0200	4.0000	130.0000	55.000	0.2025	0.8654	-0.0005	0.0059	0.	-95.
Dislocation	467	13.0700	43.0200	5.0000	131.0000	46.000	0.6877	1.6796	-0.0035	0.0197	0.	-100.
Dislocation	468	13.2200	42.6500	8.0000	129.0000	76.000	0.2657	1.0028	-0.0069	-0.0034	0.	154.
Dislocation	469	12.7600	42.8100	5.0000	100.0000	65.000	0.2730	1.0177	0.004	0.0069	0.	-60.
Dislocation	470	13.0700	43.0200	5.0000	136.0000	46.000	0.4897	1.3970	-0.0025	0.014	0.	-100.
Dislocation	471	13.0700	43.0200	5.0000	143.0000	61.000	0.3783	1.2145	-0.0015	0.0109	0.	-98.
Dislocation	472	13.0700	43.0200	5.0000	155.0000	50.000	0.4104	1.2694	0.0041	0.0112	0.	-70.
Dislocation	473	12.7800	42.8100	5.0000	85.0000	50.000	0.3440	1.1535	0.0017	0.0098	0.	-80.
Dislocation	474	13.2400	42.7600	7.0000	155.0000	55.000	0.4104	1.2694	0.001	0.0119	0.	-85.
Dislocation	475	13.1200	43.0200	2.0000	155.0000	50.000	0.2320	0.9315	0.0012	0.0066	0.	-80.
Dislocation	476	13.2900	42.5300	7.0000	154.0000	71.000	1.3201	2.3922	-0.0033	0.0382	0.	-95.
Dislocation	477	13.2500	42.7500	9.0000	164.0000	86.000	0.2227	0.9112	-0.0027	0.0059	0.	-115.
Dislocation	478	13.0800	43.0000	5.0000	148.0000	56.000	0.7878	1.8080	-0.0028	0.0227	0.	-97.
Dislocation	479	13.0700	43.0400	6.0000	167.0000	56.000	0.2657	1.0028	0.0009	0.0077	0.	-83.
Dislocation	480	13.0700	43.0400	6.0000	145.0000	50.000	0.2320	0.9315	0.	0.0067	0.	-90.
Dislocation	481	13.1400	43.0100	2.0000	147.0000	51.000	0.2109	0.8847	-0.0009	0.0061	0.	-98.
Dislocation	482	13.0800	42.9900	5.0000	150.0000	60.000	0.2730	1.0177	0.0007	0.0079	0.	-85.
Dislocation	483	13.0600	43.0100	5.0000	127.0000	62.000	0.2586	0.9881	-0.0014	0.0074	0.	-101.
Dislocation	484	13.1000	43.0400	3.0000	190.0000	90.000	0.3170	1.1036	0.0091	0.0016	0.	-10.
Dislocation	485	13.2900	42.5600	6.0000	155.0000	55.000	0.2621	0.9954	0.0007	0.0076	0.	-85.
Dislocation	486	15.8200	40.5400	10.0000	108.0000	56.000	0.5686	1.5150	-0.0064	0.0152	0.	-113.
Dislocation	487	13.1600	42.8800	5.0000	134.0000	71.000	0.1792	0.8098	-0.0031	0.0042	0.	-126.
Dislocation	488	13.0100	42.8300	1.0000	97.0000	54.000	0.1971	0.8527	-0.0034	0.0046	0.	-127.
Dislocation	489	13.0700	43.0100	5.0000	142.0000	51.000	0.1918	0.8402	-0.0008	0.0055	0.	-98.
Dislocation	490	13.0900	43.0500	3.0000	175.0000	65.000	0.1944	0.8464	0.004	0.004	0.	-45.
Dislocation	491	13.2200	42.8700	7.0000	90.0000	60.000	0.1998	0.8590	0.	0.0058	0.	-90.
Dislocation	492	13.2800	42.5600	6.0000	139.0000	66.000	0.2551	0.9808	-0.0009	0.0074	0.	-97.
Dislocation	493	13.0300	42.8400	7.0000	145.0000	70.000	0.3003	1.0715	0.	0.0087	0.	-90.
Dislocation	494	13.0700	43.0200	5.0000	165.0000	65.000	0.3732	1.2056	0.0077	0.0077	0.	-45.
Dislocation	495	10.5000	44.3300	6.0000	170.0000	50.000	0.6602	1.6429	0.0081	0.0174	0.	-65.
Dislocation	496	13.0700	43.0200	5.0000	123.0000	48.000	0.3085	1.0874	-0.0029	0.0085	0.	-109.
Dislocation	497	13.0700	43.0200	4.0000	144.0000	54.000	0.2197	0.9045	-0.0022	0.006	0.	-110.
Dislocation	498	13.1100	42.9000	3.0000	205.0000	65.000	0.8902	1.9320	0.0088	0.0243	0.	-70.
Dislocation	499	14.7300	38.0600	7.0000	50.0000	90.000	0.3393	1.1450	0.0057	-0.0081	0.	55.
Dislocation	500	13.0400	42.7400	8.0000	150.0000	70.000	0.3681	1.1967	0.0009	0.0106	0.	-85.
Dislocation	501	13.0700	42.9900	5.0000	159.0000	71.000	0.3681	1.1967	-0.0009	0.0106	0.	-95.
Dislocation	502	13.3000	42.6500	3.0000	154.0000	60.000	0.5459	1.4818	-0.0008	0.0158	0.	-93.
Dislocation	503	13.0700	43.0200	5.0000	150.0000	55.000	0.2962	1.0637	0.0007	0.0086	0.	-85.
Dislocation	504	13.0600	43.0200	5.0000	155.0000	55.000	0.4104	1.2694	0.0031	0.0115	0.	-75.
Dislocation	505	13.0600	43.0200	5.0000	160.0000	60.000	0.3085	1.0874	0.0023	0.0087	0.	-75.
Dislocation	506	13.2700	42.5600	6.0000	145.0000	50.000	0.2730	1.0177	0.0007	0.0079	0.	-85.
Dislocation	507	13.1600	42.9300	2.0000	104.0000	60.000	0.2320	0.9315	-0.0055	0.0039	0.	-145.
Dislocation	508	13.1600	42.9200	2.0000	175.0000	70.000	0.3302	1.1282	0.0055	0.0079	0.	-55.
Dislocation	509	13.2000	42.9300	2.0000	170.0000	55.000	0.2805	1.0328	0.0041	0.0071	0.	-60.
Dislocation	510	13.1700	42.9200	2.0000	175.0000	70.000	0.2138	0.8913	0.0051	0.0036	0.	-35.
Dislocation	511	13.1500	42.7800	6.0000	145.0000	53.000	0.2768	1.0252	-0.0022	0.0077	0.	-106.
Dislocation	512	13.2000	42.9200	2.0000	143.0000	48.000	0.3783	1.2145	-0.0036	0.0104	0.	-109.
Dislocation	513	12.7500	42.8000	4.0000	72.0000	85.000	0.7360	1.7426	-0.0194	0.009	0.	-155.
Dislocation	514	13.2400	42.5700	3.0000	180.0000	70.000	0.2053	0.8718	0.0042	0.0042	0.	-45.
Dislocation	515	13.1100	43.0100	1.0000	140.0000	65.000	0.1481	0.7305	0.0011	0.0042	0.	-75.
Dislocation	516	13.0700	42.9700	5.0000	113.0000	66.000	0.2730	1.0177	-0.0043	0.0066	0.	-123.
Dislocation	517	13.2700	42.4400	7.0000	118.0000	51.000	0.3003	1.0715	-0.0049	0.0072	0.	-124.
Dislocation	518	13.2700	42.4300	7.0000	105.0000	70.000	0.2109	0.8847	-0.0048	0.0038	0.	-142.
Dislocation	519	13.2800	42.4200	7.0000	108.0000	66.000	0.3994	1.2508	-0.009	0.0073	0.	-141.0001
Dislocation	520	13.0700	43.0800	5.0000	175.0000	60.000	0.3487	1.1620	0.0051	0.0088	0.	-60.